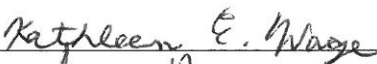
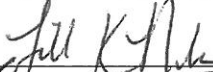
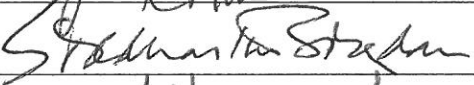
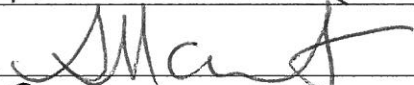
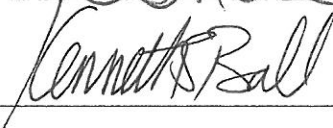


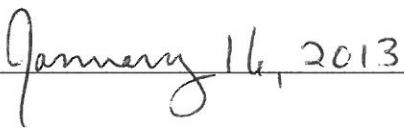
APPLICATION OF THE REITERATIVE MMSE ALGORITHM TO UNDERWATER
ACOUSTICS USING COVARIANCE MATRIX TAPERS FOR ROBUSTNESS

by

Travis Cuprak
A Thesis
Submitted to the
Graduate Faculty
of
George Mason University
In Partial fulfillment of
The Requirements for the Degree
of
Master of Science
Electrical Engineering

Committee:

	Dr. Kathleen Wage, Thesis Director
	Dr. Jill Nelson, Committee Member
	Dr. Siddhartha Sikdar, Committee Member
	Dr. Andre Manitus, Chairman, Department of Electrical and Computer Engineering
	Dr. Kenneth S. Ball, Dean, Volgenau School of Engineering

Date:  Spring Semester 2013
George Mason University
Fairfax, VA

Application of the Reiterative MMSE Algorithm to Underwater Acoustics Using
Covariance Matrix Tapers for Robustness

A thesis submitted in partial fulfillment of the requirements for the degree of
Master of Science at George Mason University

By

Travis Cuprak
Bachelor of Science
University of Notre Dame, 2003

Director: Dr. Kathleen Wage, Professor
Department of Electrical and Computer Engineering

Spring Semester 2013
George Mason University
Fairfax, VA

Copyright © 2013 by Travis Cuprak
All Rights Reserved

Dedication

Like all of my work, this thesis is dedicated to my family: To my wife Melissa; to my children Stephanie, Kyle, Gregory, and to any other children I may have the privilege of holding.

Acknowledgments

First, I would like to thank my advisor, Dr. Kathleen Wage, for her help in making this thesis a reality. Her constructive comments and insight were extremely helpful throughout the whole process.

I would also like to thank the other members of my thesis committee: Dr. Jill Nelson and Dr. Siddhartha Sikdar. They provided great feedback and helpful suggestions.

The acoustic data presented in Chapter 6 was obtained through Office of Naval Research (ONR) Award N00014-08-1-0840. I would like to extend thanks to Dr. Peter Worcester and Dr. Matthew Dzieciuch of Scripps Institution of Oceanography for supplying the data.

I would also like to thank my employer, Adaptive Methods, Inc. Their tuition reimbursement program has enabled me to further my education.

I wish to express a great deal of gratitude to my wife Melissa for her encouragement and support. I would also like to thank my children: Stephanie, Kyle, and Gregory for providing me with much needed breaks and reminding me of what's truly important.

Table of Contents

	Page
List of Tables	viii
List of Figures	ix
Abstract	xii
1 Introduction	1
1.1 Time Domain Sidelobes	1
1.2 Sonar Background	2
1.2.1 Current Approaches for Resolving Time Overlapped Signals	4
1.3 Summary	5
2 An Adaptive Algorithm for the Suppression of Time Domain Sidelobes	7
2.1 Notation Conventions	7
2.2 Multipath Model	9
2.3 Discrete Received Signal Model	10
2.3.1 Signal Model Parameters	10
2.3.2 Matrix-Vector Form of Signal Model	11
2.4 Derivation of the Reiterative Minimum Mean Squared Error Algorithm	15
2.4.1 MMSE Formulation	15
2.4.2 RMMSE Algorithm	17
2.4.3 RMMSE Implementation	21
2.4.4 Gain Constrained RMMSE	23
2.5 RMMSE Operational Description	23
2.5.1 Filter Convergence	23
2.5.2 Cross Correlation Effects of Adaptive Weights	24
2.6 RMMSE Topics in Literature	25
2.6.1 General RMMSE Papers	26
2.6.2 Processing Time	26
2.6.3 RMMSE Robustness	27
2.6.4 Multistatics and Shared Spectrum Processing	27
2.6.5 Additional Applications	27

2.7	Summary	28
3	RMMSE Sensitivity to Mismatch and Distortion	29
3.1	Figure of Merit Development	29
3.1.1	Visual Detection	29
3.1.2	Mean Squared Error	30
3.1.3	Mean Sidelobe Level	30
3.1.4	Median Sidelobe Level	31
3.1.5	Selected FOM	32
3.2	Simulation Settings	32
3.2.1	Level Calibration	34
3.3	Simulation Results	34
3.3.1	Baseline Simulation	34
3.3.2	Signal Power Sweep	35
3.3.3	Intrasample Arrival	37
3.3.4	Doppler Distortion	39
3.3.5	Doppler Distortion with Doppler Estimation	45
3.3.6	Uncalibrated Transducer Distortion	49
3.4	Sensitivity Study Summary	51
4	Enhancing RMMSE Performance Using Covariance Matrix Tapers	53
4.1	Overview of Covariance Matrix Tapers	53
4.1.1	Covariance Matrix Taper Framework	53
4.2	CMT Use in RMMSE Processing	55
4.2.1	CMT Application to RMMSE for LFM Intrasample Arrival: Time Shift View	56
4.2.2	CMT Application to RMMSE for LFM Intrasample Arrival: Instan- taneous Frequency View	60
4.2.3	CMT Application to RMMSE for Small Doppler Shifts	64
4.2.4	CMT Application to RMMSE for Uncalibrated Transducers	66
4.3	Summary	67
5	Results of Applying Covariance Matrix Tapers to RMMSE Processing	69
5.1	Simulation Setup and CMT Selection	69
5.2	Simulation Results	70
5.2.1	Baseline Case	70
5.2.2	Intrasample Arrival	71
5.2.3	Doppler Distortion	73

5.2.4	Uncalibrated Transducer Effects	75
5.2.5	Stressing Scenario	80
5.3	Summary of CMT Use in RMMSE Processing	83
6	Acoustic Data Analysis	84
6.1	Data Description and Processing Steps	84
6.1.1	Input Data	86
6.1.2	Data Preprocessing	87
6.1.3	Data Processing	88
6.2	Processing Results	91
6.3	Summary	93
7	Conclusions	96
7.1	Application of RMMSE Algorithm to Active Sonar	96
7.2	Performance with Experimental Data	97
7.3	Future Work	98
A	CMT Use in Adaptive Beamforming	99
A.1	CMT Derivation	99
A.1.1	Case 1: Stationary Interferer	100
A.1.2	Case 2: Moving Interferer	101
A.2	Summary of CMT use in Adaptive Beamforming	104
	Bibliography	105

List of Tables

Table	Page
3.1 Parameters used in simulated waveform	33
5.1 Stressing scenario signal settings	81
5.2 Stressing scenario SNR results	82
6.1 Acoustic Data LFM Parameters	86
6.2 Paths for acoustic signal propagation	94

List of Figures

Figure	Page
1.1 Matched filter input and output time responses with signals at $t = -0.1$, $t = 0$ seconds	2
1.2 Matched filter output. Quiet signal at $t = -0.1$ seconds; loud signal at $t = 0$ seconds. Sidelobes obscure weaker signal	3
1.3 Basic multipath illustration. The signal transmitted from the source travels along 2 paths to the receiver, as indicated by the ray lines	4
2.1 Multipath profile. (Left): Path Geometry; (Right): Path profile. Path 1 is the shorter path and its signal arrives first. The signal arriving from Path 2 arrives later and is attenuated relative to the signal from Path 1.	9
2.2 Received signal model for the RMMSE algorithm	10
2.3 Illustration of received signal model. Top left: True multipath profile. Top right: Waveform replica. Bottom left: Convolution of replica with multipath profile. Bottom right: Received data	14
2.4 Adaptive process diagram used for algorithm derivation. The adaptive filter is used to estimate the multipath profile.	15
2.5 RMMSE iteration process. Following an initialization stage, weights are iteratively computed to generate a new estimate	22
2.6 RMMSE convergence illustration. Left plot: RMMSE results through iteration stages. Right plot: Squared error at given lag value minimized as algorithm iterates.	24
2.7 Illustration of the null created by the weights at lag=-0.05 seconds to cancel the signal arriving at lag=0 seconds	25
3.1 Region used to obtain average sidelobe levels indicated by black horizontal bars. The region does not extend beyond the autocorrelation sidelobes and is notched near the true signal locations	31

3.2	Comparison of mean and median sidelobe estimation levels in a severe distortion case. The mean sidelobe level (dashed black line) is raised by the dynamic range of the sidelobes. The median sidelobe level (dashed red line) is less sensitive to these effects.	32
3.3	RMMSE (red) and Matched Filter (blue) outputs for the baseline simulation	35
3.4	MSL as a function of signal power for matched filter and RMMSE	36
3.5	RMMSE and matched filter output when the rising edge of the primary signal arrives halfway between A/D samples	38
3.6	RMMSE and matched filter output when the rising edge of the secondary signal arrives halfway between A/D samples	39
3.7	Effect of intrasample arrival on MSL for primary and secondary signals . .	40
3.8	Doppler distortion examples: Matched filter and RMMSE output	43
3.9	Doppler Distortion Results	44
3.10	Example Ambiguity Surface	46
3.11	Algorithm Output for Primary Signal with +1.5 m/s range rate, opening .	47
3.12	Effects of Doppler estimation on RMMSE processing	48
3.13	Modeled transfer functions for calibrated and uncalibrated transducers . . .	50
3.14	Effects of uncalibrated transducers on RMMSE processing	51
4.1	Probability Density Function for a zero mean uniform time distribution . .	58
4.2	Effects of Intrasample Arrival on LFM Pulse	61
4.3	Probability Density Function for a zero mean uniform frequency distribution	62
4.4	Effects of Doppler on LFM pulse for a low opening Doppler	65
4.5	Probability density function for μ as a uniform distribution on the interval (0,1]	66
5.1	Baseline simulation: RMMSE (red) and matched filter (blue) outputs . . .	70
5.2	CMT to be applied to estimated covariance matrix	71
5.3	Intrasample arrival distortion: Results of RMMSE and RMMSE-CMT processing; Pulse arrives halfway between A/D samples	72
5.4	Intrasample arrival distortion: MSL for matched Filter, RMMSE and RMMSE-CMT	73
5.5	Doppler distortion: MSL of matched filter, RMMSE, RMMSE-CMT outputs. Doppler estimation not performed	74
5.6	Doppler distortion: RMMSE and RMMSE-CMT output with ± 1.5 m/s Doppler	76

5.7	Doppler distortion with Doppler estimation: MSL for matched filter, RMMSE and RMMSE-CMT approaches	77
5.8	CMT for uncalibrated transducer distortion	78
5.9	Uncalibrated transducer distortion: Results of matched filter, RMMSE and RMMSE-CMT processing, lowest frequency attenuated 40 dB	78
5.10	Uncalibrated transducer distortion: MSL of matched filter, RMMSE, and RMMSE-CMT outputs. Min taper value (μ) on x -axis, MSL rel. baseline noise floor on y -axis	79
5.11	Stressing Scenario: Results of matched filter, RMMSE and RMMSE-CMT processing, true signal locations denoted by black vertical ticks	82
6.1	Transmitter and receiver configuration for acoustic data. Transmit beampattern is symmetric about vertical axis	85
6.2	Spectrogram of acoustic data. Zoomed to show LFM region.	86
6.3	Acoustic data and replica preprocessing steps. Colored background regions highlight sample rate changes	87
6.4	Magnitude (top) and phase angle (bottom) of LPF used in acoustic data processing. 2700 point Chebychev window with 10 Hz cutoff frequency. Zoomed to show passband.	89
6.5	Acoustic data and replica processing steps.	89
6.6	Results of processing acoustic data through candidate algorithms. Matched filter shown in blue, adaptive algorithms shown in red	92
6.7	Paths resolved by RMMSE output	94
A.1	Probability Density Function for a zero mean uniform angular distribution .	102

Abstract

APPLICATION OF THE REITERATIVE MMSE ALGORITHM TO UNDERWATER ACOUSTICS USING COVARIANCE MATRIX TAPERS FOR ROBUSTNESS

Travis Cuprak, M.S.

George Mason University, 2013

Thesis Director: Dr. Kathleen Wage

Signal detection in underwater acoustics is conventionally performed with the matched filter. The matched filter is simple, efficient, and well understood. Unfortunately, it is also susceptible to poor sidelobe performance in the presence of loud signals. This can lead to signal masking and missed detections. The matched filter may not be able to resolve the arrival time of multiple, closely-spaced signals. The goal of this thesis is to explore the use of a new radar algorithm, known as the Reiterative Minimum Mean Squared Error (RMMSE) Algorithm [1] for use in underwater acoustics.

The sensitivity of the RMMSE algorithm to several common sonar distortions is explored. The distortions are simulated and processing results are presented. Algorithm sensitivity is quantified through a measurement of the median sidelobe level of the filter output. It is seen that the RMMSE algorithm suffers from degraded performance in the presence of the simulated distortions, and in some cases the adverse effects of the distortion are severe. Further investigation derives Covariance Matrix Tapers (CMTs) as a robustness enhancement to the RMMSE algorithm. Simulations demonstrate the benefit of RMMSE-CMT processing. In all cases investigated, CMTs successfully mitigate distortion and improve output sidelobe levels.

CMTs are also computationally efficient. They are computed once and applied through the use of the Hadamard product (element by element matrix multiplication). The use of CMTs in RMMSE processing is a new contribution to RMMSE literature.

Experimental data analysis is also presented. Initial RMMSE processing results show severely degraded algorithm performance- only the strongest signal is visible. RMMSE-CMT processing reveals the presence of at least three additional signals that are unresolvable in the matched filter and RMMSE sidelobes.

Chapter 1: Introduction

The problem of resolving time-overlapped signals has a long history in underwater acoustics. An early reference [2] to this problem found in the open literature highlights a sonar test performed in 1971. In this event, the time sidelobes caused by multipath were so confounding that 10% of the collected data could not be used. Since then, numerous methods have been developed to address this problem. These techniques include, but are not limited to, hardware configurations, waveform designs and signal processing algorithms. This thesis addresses the specific problem of resolving signals obscured by time-domain sidelobes. The remainder of this chapter provides a brief introduction to the causes of this problem.

1.1 Time Domain Sidelobes

The algorithm most commonly used for waveform detection in underwater acoustics is the matched filter. The matched filter is the filter that maximizes output signal to noise ratio (SNR) [3]. When the noise is assumed to be additive white noise, the matched filter takes the form of a conjugated, time reversed copy of the waveform. This filter is commonly used for waveform detection in many applications, including radar, sonar and communications. It is well understood, easy to compute, and may be implemented efficiently using fast convolution. Figure 1.1(a) shows a simulated time series input to the matched filter. The signal is a 200 Hz, 0.2 second chirp waveform. The simulated time series includes two signal arrivals with unit power plus additive white noise. The signals arrive at times $t = -0.1$ and $t = 0$ seconds. The signals are overlapped and are obscured by noise. Consequently, the signals cannot be resolved in this plot. Figure 1.1(b) shows the output of the matched filter for the same data. The matched filter has coherently integrated the waveforms and both signals can be seen as 20 dB spikes at $t = -0.1$ and $t = 0$ seconds.

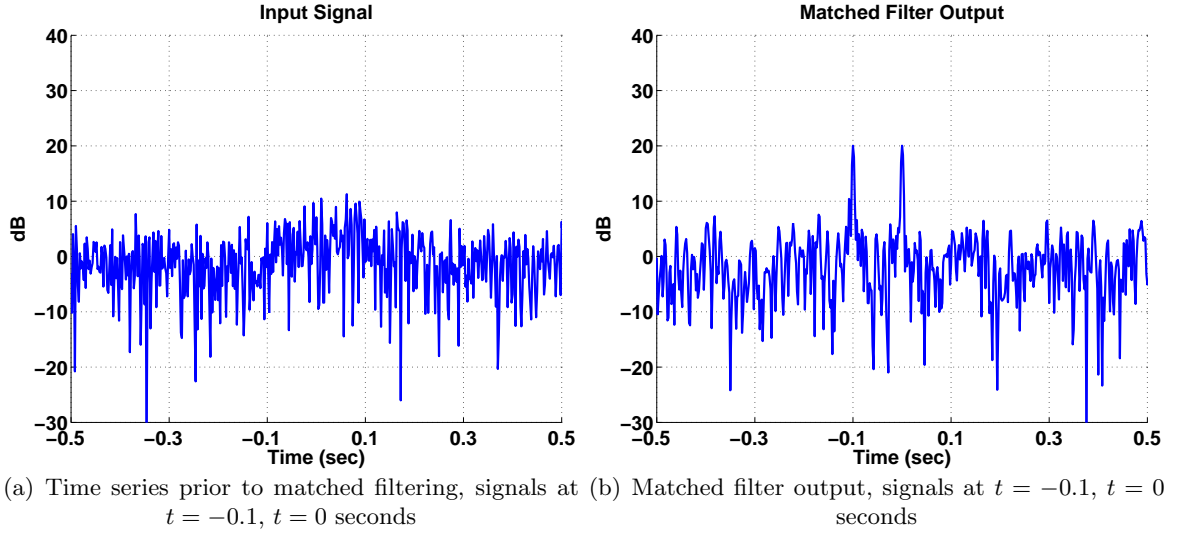


Figure 1.1: Matched filter input and output time responses with signals at $t = -0.1, t = 0$ seconds

The matched filter output can become corrupted by sidelobes as the input signal power increases. This is seen in Figure 1.2. The same simulation described previously is used, but the power of the signal arriving at $t = 0$ seconds has been increased by 40 dB. The matched filter response still shows a peak at $t = 0$. The region surrounding the peak has been corrupted by elevated sidelobes and the signal at $t = -0.1$ seconds is completely masked. The ability of the matched filter to resolve closely spaced signals is limited by the waveform autocorrelation function.

1.2 Sonar Background

This section provides a brief overview of multipath and active sonar. For a more complete primer on underwater acoustics, please see the reference by Urick [4].

Sonar (SOund Navigation And Ranging) is primarily concerned with the detection of propagating underwater pressure (sound) waves. Generally speaking, a source emits a pressure wave, either intentionally (active sonar), or inadvertently due to mechanical

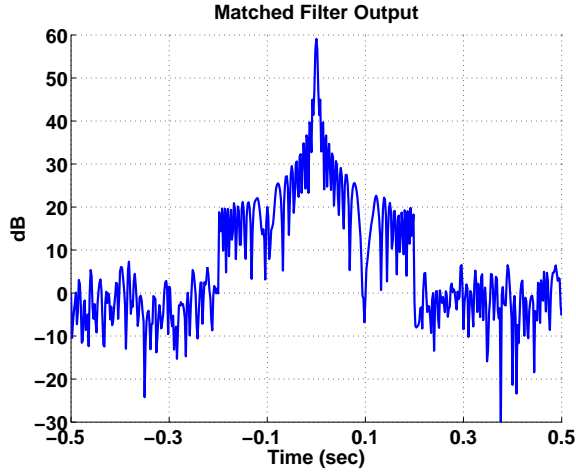


Figure 1.2: Matched filter output. Quiet signal at $t = -0.1$ seconds; loud signal at $t = 0$ seconds. Sidelobes obscure weaker signal

noise/vibration (passive sonar). The pressure wave travels through the water at the speed of sound. A sonar system designed to detect such energy contains one or more transducers sensitive to the pressure wave. When the signal reaches the receiver, the transducer element is excited and generates a voltage differential, indicating that a signal has been received. A significant amount of effort is dedicated towards developing specialized hardware and software to maximize the ability to detect an underwater signal.

The underwater acoustic environment is subject to a wide variety of signal propagation distortions. Thermal layers, currents, surface/bottom reflections, variations in water properties, and many other factors render the ocean effectively inhomogeneous. As energy travels from a source to a receiver, the signal may travel along several different paths, which can be approximated by a ray propagation model. This is referred to as multipath propagation, and is illustrated in the ray diagram of Figure 1.3. The presence of multipath has significant effects on sonar signal processing. A brief survey of potential problems is described in [5]. Of particular interest is the effect of multipath on active sonar. The sonar source transmits a pulse of energy, and the receiver attempts to detect the presence of the signal. The detection process is typically performed through matched filtering. Multipath

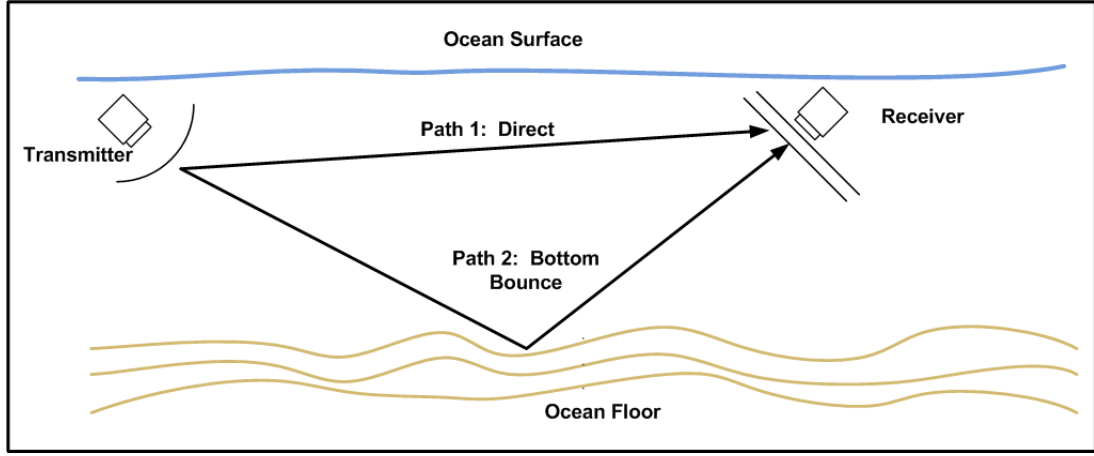


Figure 1.3: Basic multipath illustration. The signal transmitted from the source travels along 2 paths to the receiver, as indicated by the ray lines

propagation causes multiple copies of the signal to arrive at the receiver, separated by a time offset related to the distance traveled. As seen previously, signals arriving at relatively close times may not be resolvable with the matched filter.

1.2.1 Current Approaches for Resolving Time Overlapped Signals

In [2], several approaches for resolving multipath signals are presented. The inverse filter is mentioned, but is quickly discounted due to implementation considerations and sensitivity to distortion. An alternative approach is a minimum mean squared error approach. This approach is derived as an approximation to the inverse filter. Another approach found in [2] is a maximum-likelihood approach. In this method, the number of multipath arrivals is known or estimated a priori and this information is used to determine their time delays. Other methods for resolving delayed time arrivals can be found in acoustic and signal processing literature. Some, such as the Generalized Likelihood Ratio Test (GLRT) approach in [6] utilize prior knowledge of the multipath environment.

Alternately, system design techniques can be used to help resolve multipath. One option is to use an acoustic array that can spatially resolve multipath arrivals through beamforming [4]. This is accomplished either through construction of a two or three dimensional array,

or by orienting a linear array such that the aperture can spatially separate multipath. It is also possible to utilize waveforms that do not suffer from the time domain sidelobe problem. Signals such as M-Sequences [7] have more desirable autocorrelation properties (compared to LFM) and can be detected using the matched filter. Such signals, however, are typically very sensitive to Doppler and other distortions.

1.3 Summary

Time domain sidelobes are a long standing problem in active sonar. These sidelobes can mask the presence of a multiple signals arrivals. A few potential causes of this effect are

- Multipath propagation
- Bathymetric features (such as seamounts)
- Distributed signal reflectors, such as whales or schools of fish

Sidelobe masking can occur in any system utilizing active sonar pulses. Some common applications of pulsed sonar are

- Sound channel characterization
- Sub-bottom profilers
- Undersea communications
- Defense/warfare applications

Common methods currently used for mitigating time domain sidelobes tend to focus on waveform and system design. Long duration waveforms may be used to reduce sidelobe levels, but require more power and are sensitive to distortion. Waveform shading techniques may reduce sidelobe extent but affect detection performance. Complicated waveforms with desirable autocorrelation properties may be used, but are sensitive to distortion. Other techniques require prior knowledge of signal propagation paths. Time domain sidelobes

have no physical meaning and are purely a signal processing phenomenon. Given recent advances in computing power, advanced signal processing techniques may also be used to prevent or mitigate time domain sidelobes.

Chapter 2: An Adaptive Algorithm for the Suppression of Time Domain Sidelobes

This chapter describes the algorithm being investigated as a solution to the time domain sidelobe problem. The candidate algorithm is the Reiterative Minimum Mean Squared Error (RMMSE) algorithm. The RMMSE algorithm was originally published by Blunt and Gerlach in 2003 [1] for high resolution radar imaging. The algorithm adaptively deconvolves the transmitted waveform out of the received data using second order statistics. The deconvolution process suppresses sidelobes and provides enhanced signal detection by revealing the presence of weaker signals in close proximity to strong signals.

An important highlight of the RMMSE algorithm over other adaptive algorithms is that the adaptive weights are computed with a single snapshot of data. This feature is particularly desirable in underwater acoustics. For statistics to be built across snapshots, the acoustic environment has to be stationary across many pings. For useful range scales, this could correspond to tens of minutes or more, which is not practical. The RMMSE algorithm adapts on a single ping and bypasses this problem.

This chapter defines the notation conventions and presents the signal model. A detailed derivation of the algorithm is provided, followed by an operational description. A survey of publications related to the RMMSE algorithm is also provided.

2.1 Notation Conventions

The notation used throughout the remainder of this thesis is summarized briefly below. All quantities are assumed to be complex valued in general.

- Italic lowercase letters, such as s correspond to scalar quantities.

- j indicates the imaginary number, $j = \sqrt{-1}$.
- Boldface, lowercase letters, such as \mathbf{s} correspond to column vectors.
- Boldface, uppercase letters, such as \mathbf{C} correspond to matrices.
- A superscript uppercase T, $(\bullet)^T$, denotes vector or matrix transpose.
- A superscript asterisk, $(\bullet)^*$, represents complex conjugation.
- A superscript uppercase H, $(\bullet)^H$, represents complex conjugate transpose of a vector or matrix.
- A tilde above a quantity, such as, \tilde{x} represents the *true* value of that quantity.
- A carat, or hat, above a quantity, such as \hat{x} represents the *estimated* value of that quantity.
- An uppercase italicized E with curly brackets, $E\{\bullet\}$, denotes the expectation operator.
- The italicized uppercase N refers to the number of samples in the transmitted waveform sampled at the baseband rate.

In order to distinguish between quantities that change with time and quantities that do not, the following conventions are used:

- The elements of a vector that do not change with time are distinguished by a subscript numeral. For example, in the following vector, the values of the elements remain the same regardless of time or lag:

$$\mathbf{s} = [s_0, s_1, \dots, s_{N-1}]^T$$

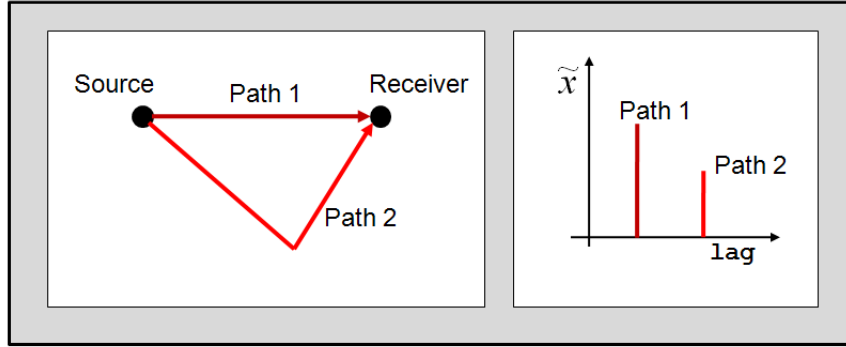


Figure 2.1: Multipath profile. (Left): Path Geometry; (Right): Path profile. Path 1 is the shorter path and its signal arrives first. The signal arriving from Path 2 arrives later and is attenuated relative to the signal from Path 1.

- The elements of a vector that change with time are distinguished by parentheses. For example, in the following vector, the values of the elements vary with lag/time:

$$\mathbf{x}(l) = [x(l), x(l-1), \dots, x(l-N+1)]^T$$

2.2 Multipath Model

The multipath environment is modeled as shown in Figure 2.1. Two signal paths are shown. The picture on the left represents the path geometry, and the picture on the right represents the multipath profile. Path 1 is a direct path from the source to the receiver. Path 2 is an indirect path between the source and the receiver, possibly the result of a reflection off the ocean floor. In the multipath profile, the signal from Path 1 arrives first and has high power. The Path 2 signal arrives after the signal from Path 1 (due to the longer distance traveled) and has lower relative power.

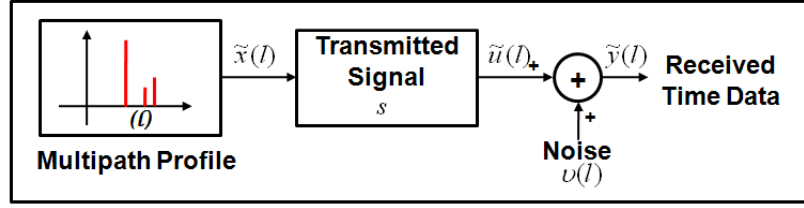


Figure 2.2: Received signal model for the RMMSE algorithm

2.3 Discrete Received Signal Model

Figure 2.2 is a graphical representation of the received signal model used in the derivation of the RMMSE algorithm.

2.3.1 Signal Model Parameters

The variables shown in the signal model of Figure 2.2 represent are defined below:

- x is the multipath profile. This is the random process that is to be estimated. In the language of Widrow and Stearns [8] or Haykin [9], it is the “desired” signal. In general, this profile will consist of zeros for all lags, except lags at which a copy of the transmitted signal is received. At lags corresponding to a signal arrival, the power of $x(l)$ corresponds to the amplitude of the signal.
- s is the transmitted waveform. In general, this is known a priori.
- u is the result of the convolution of the multipath profile with the transmitted waveform
- ν corresponds to additive noise
- y is the sum $u + \nu$. This is the received data. In practice, this is commonly a hydrophone time series or a beam time series.

In Figure 2.2 it is worth noting that it has been chosen to place x prior to s . In some cases, this may seem counterintuitive as the transmitted waveform can be thought of as occurring first. Since these two quantities are convolved against each other, their relative order does not truly matter. Placing x first reinforces its role as a random process to be estimated and makes it consistent with the notation in [8]. Furthermore, this choice is convenient for purposes of algorithm derivation.

The choice of lag (or time) index convention is arbitrary, as long as a consistent method is applied. In this work, the current lag (or time) index under investigation is referred to as lag $l = 0$. Increasing values of l such as $l = (1, 2, 3, 4, \dots)$ correspond to samples that arrive after the current sample. Conversely, negative values of l , such as $l = (-1, -2, -3, -4, \dots)$ correspond to samples that arrive before the current sample. Converting a lag index l to a relative time value in seconds is accomplished by dividing l by the sample rate.

2.3.2 Matrix-Vector Form of Signal Model

It is necessary to define the terms of Figure 2.2 in matrix-vector form so that a mathematical description of the signal model may be developed. The vectors and matrices of interest are now defined.

Multipath Profile: Vector Form

The vector $\tilde{\mathbf{x}}$ is defined as N contiguous samples of the multipath profile:

$$\tilde{\mathbf{x}}(l) = \begin{bmatrix} \tilde{x}(l) \\ \tilde{x}(l-1) \\ \vdots \\ \tilde{x}(l-N+1) \end{bmatrix} \quad (2.1)$$

Note that the first lag index of $\tilde{\mathbf{x}}$ is the current lag index. Subsequent indices decrement in the direction of previous lags. This is the only lag-dependent vector in which the elements

are in time-reversed order.

Multipath Profile: Matrix Form

A matrix that is required for the RMMSE derivation is the matrix form of the multipath profile. Each column of this $N \times N$ matrix is a sample shifted version of $\tilde{\mathbf{x}}$:

$$\mathbf{A}(l) = \begin{bmatrix} | & | & & | \\ \tilde{\mathbf{x}}(l) & \tilde{\mathbf{x}}(l+1) & \dots & \tilde{\mathbf{x}}(l+N-1) \\ | & | & & | \end{bmatrix} \quad (2.2)$$

Waveform Replica Vector

The transmitted waveform is typically an analog waveform with a phase or frequency modulation, such as linear or hyperbolic frequency modulation. For digital processing, a discrete representation of the waveform is required. This is typically accomplished through sampling of the basebanded waveform at the A/D sample rate. The sampling the results are stored in a vector, known as the waveform replica vector. The N elements of the waveform replica vector are denoted as:

$$\mathbf{s} = \begin{bmatrix} s_0 \\ s_1 \\ \vdots \\ s_{N-1} \end{bmatrix} \quad (2.3)$$

It is generally assumed that the waveform replica is not time dependent, so the elements of \mathbf{s} are denoted with a subscript numeral.

Convolution of Multipath Profile with Replica

The time reversal described by (2.1) allows the convolution of $\tilde{\mathbf{x}}$ and \mathbf{s} to be represented with an inner product:

$$\tilde{u}(l) = \tilde{\mathbf{x}}^T(l)\mathbf{s} \quad (2.4)$$

Received Data: Scalar Form

The received data at lag l , $\tilde{y}(l)$, is $\tilde{u}(l)$ plus noise:

$$\tilde{y}(l) = \tilde{u}(l) + \nu(l) = \tilde{\mathbf{x}}^T(l)\mathbf{s} + \nu(l) \quad (2.5)$$

where $\nu(l)$ is additive noise at the given lag.

Received Data: Vector Form

The vector representation of the received data, $\tilde{\mathbf{y}}(l)$ is the column vector consisting of N contiguous samples of the input data:

$$\tilde{\mathbf{y}}(l) = \begin{bmatrix} y(l) \\ y(l+1) \\ \vdots \\ y(l+N-1) \end{bmatrix} \quad (2.6)$$

Defining the N element noise vector $\tilde{\boldsymbol{\nu}}(l)$ as N contiguous samples of noise:

$$\tilde{\boldsymbol{\nu}}(l) = \begin{bmatrix} \nu(l) \\ \nu(l+1) \\ \vdots \\ \nu(l+N-1) \end{bmatrix} \quad (2.7)$$

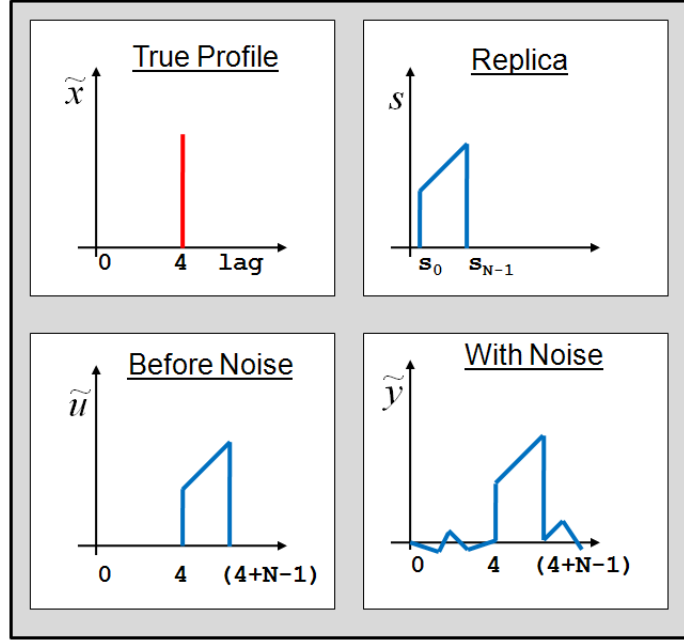


Figure 2.3: Illustration of received signal model. Top left: True multipath profile. Top right: Waveform replica. Bottom left: Convolution of replica with multipath profile. Bottom right: Received data

Then $\tilde{\mathbf{y}}(l)$ is:

$$\tilde{\mathbf{y}}(l) = \mathbf{A}(l)^T \mathbf{s} + \tilde{\mathbf{v}}(l) \quad (2.8)$$

Received Data: Summary

Figure 2.3 is a graphical illustration of the relationship between \mathbf{s} , $\tilde{\mathbf{x}}$, and $\tilde{\mathbf{y}}$. The top-left image shows the true multipath profile. There is 1 signal, arriving at lag $l = 4$. The top-right image shows the waveform replica. The bottom-left image shows the convolution of the multipath profile with the waveform replica. The bottom-right image shows the received data. In the practical applications of interest, the multipath profile $\tilde{\mathbf{x}}$ is unknown. The received data, $\tilde{\mathbf{y}}$ and waveform replica \mathbf{s} are known.

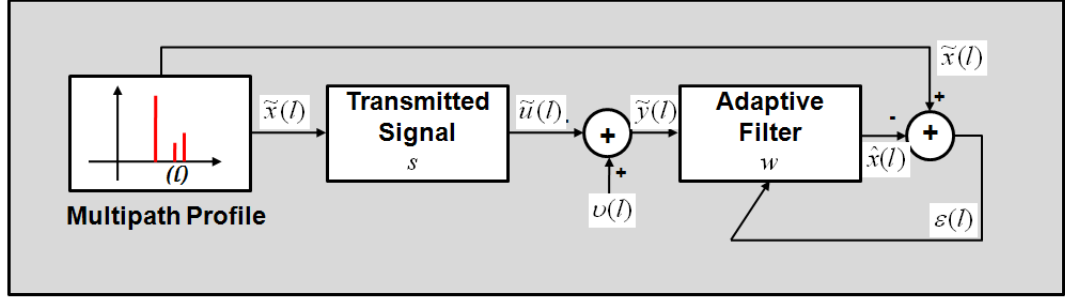


Figure 2.4: Adaptive process diagram used for algorithm derivation. The adaptive filter is used to estimate the multipath profile.

2.4 Derivation of the Reiterative Minimum Mean Squared Error Algorithm

This section provides a detailed derivation of the RMMSE algorithm. The general Minimum Mean Squared Error (MMSE) derivation commonly found in adaptive signal processing literature is presented first. This result is then used in the derivation of the RMMSE algorithm, which takes advantage of several assumptions to estimate statistics.

2.4.1 MMSE Formulation

This section derives the general Minimum Mean Squared Error (MMSE) equations. This derivation closely follows the discussion in [10]. The notation has been changed to match the signal model presented for the RMMSE algorithm. For simplicity, the lag index, l , is omitted in subsequent derivations except where absolutely necessary.

Figure 2.4 shows the architecture for the adaptive process. The parameter to be estimated using a minimum mean squared error approach is \tilde{x} . The transmitted waveform, s , is known, as is the received data, \tilde{y} . The estimate of \tilde{x} is denoted by \hat{x} , and is the output of the adaptive filter:

$$\hat{x} = \mathbf{w}^H \tilde{\mathbf{y}} \quad (2.9)$$

where \mathbf{w} is the N element vector of adaptive weights. The difference between \hat{x} and \tilde{x} is the estimation error, ϵ :

$$\epsilon = \tilde{x} - \hat{x} \quad (2.10)$$

The mean-squared error, denoted as J , is the expected value of $|\epsilon|^2$:

$$J = E \{ |\epsilon|^2 \} = E \{ |\tilde{x} - \hat{x}|^2 \} = E \{ |\tilde{x} - \mathbf{w}^H \tilde{\mathbf{y}}|^2 \} \quad (2.11)$$

The J term is also sometimes referred to as the performance surface [8]. Expanding the squared term above:

$$J = E \{ (\tilde{x} - \mathbf{w}^H \tilde{\mathbf{y}}) (\tilde{x}^* - \tilde{\mathbf{y}}^H \mathbf{w}) \} \quad (2.12)$$

and mutliplying through results in:

$$J = E \{ \tilde{x} \tilde{x}^* - \mathbf{w}^H \tilde{\mathbf{y}} \tilde{x}^* - \tilde{x} \tilde{\mathbf{y}}^H \mathbf{w} + \mathbf{w}^H \tilde{\mathbf{y}} \tilde{\mathbf{y}}^H \mathbf{w} \} \quad (2.13)$$

Using the linearity property of the expectation operator and assuming that the weights are not statistical quantities gives:

$$J = E \{ |\tilde{x}(l)|^2 \} - \mathbf{w}^H E \{ \tilde{\mathbf{y}}(l) \tilde{x}(l)^2 \} - E \{ \tilde{x}(l) \tilde{\mathbf{y}}^H \} \mathbf{w} + \mathbf{w}^H E \{ \tilde{\mathbf{y}} \tilde{\mathbf{y}}^H \} \mathbf{w} \quad (2.14)$$

To simplify the notation, the following definitions are set:

$$\begin{aligned} \mathbf{P}_x &\triangleq E \{ |\tilde{x}(l)|^2 \} && \text{Variance of the desired response} \\ \mathbf{d} &\triangleq E \{ \tilde{\mathbf{y}}(l) \tilde{x}(l)^* \} && \text{Cross correlation between input and desired response} \\ \mathbf{R}_{yy} &\triangleq E \{ \tilde{\mathbf{y}} \tilde{\mathbf{y}}^H \} && \text{Input autocorrelation matrix} \end{aligned} \quad (2.15)$$

The substitutions result in the notational simplification of J :

$$J = \mathbf{P}_x - \mathbf{w}^H \mathbf{d} - \mathbf{d}^H \mathbf{w} + \mathbf{w}^H \mathbf{R}_{yy} \mathbf{w} \quad (2.16)$$

The complex gradient of J is computed with respect to \mathbf{w}^H :

$$\nabla_{\mathbf{w}^H} J = \mathbf{R}_{yy} \mathbf{w} - \mathbf{d} \quad (2.17)$$

The value of J is minimized when the complex gradient is equal to the null vector, $\mathbf{0}$. The weights that satisfy this equation are referred to as the optimum weight vector, \mathbf{w}_o .

$$\mathbf{0} = \mathbf{R}_{yy} \mathbf{w}_o - \mathbf{d} \quad (2.18)$$

Assuming that \mathbf{R}_{yy} is non-singular, \mathbf{w}_o is:

$$\mathbf{w}_o = \mathbf{R}_{yy}^{-1} \mathbf{d} \quad (2.19)$$

These resulting weights are the familiar Wiener-Hopf weights in matrix form [8].

2.4.2 RMMSE Algorithm

Up to this point, the derivation has followed the typical minimum mean squared error derivation found in textbooks such as [10]. This is the starting point for the RMMSE algorithm. The subsequent equations and assumptions are specific to RMMSE processing.

The first step is to substitute the definitions of \mathbf{R}_{yy} and \mathbf{d} from (2.15) into (2.19), resulting in:

$$\mathbf{w}_o = (E \{ \tilde{\mathbf{y}} \tilde{\mathbf{y}}^H \})^{-1} E \{ \tilde{\mathbf{y}}(l) \tilde{x}(l)^* \} \quad (2.20)$$

The two expectation terms in the equation above will be expanded separately.

Expansion of $E \{ \tilde{\mathbf{y}} \tilde{\mathbf{y}}^H \}$

Using (2.8), $\tilde{\mathbf{y}}$ can be decomposed into a multipath profile and noise component:

$$\begin{aligned}
E \{ \tilde{\mathbf{y}} \tilde{\mathbf{y}}^H \} &= E \{ (\mathbf{A}^T \mathbf{s} + \tilde{\boldsymbol{\nu}})(\mathbf{A}^T \mathbf{s} + \tilde{\boldsymbol{\nu}})^H \} \\
&= E \{ (\mathbf{A}^T \mathbf{s} + \tilde{\boldsymbol{\nu}})(\mathbf{s}^H \mathbf{A}^* + \tilde{\boldsymbol{\nu}}^H) \} \\
&= E \{ \mathbf{A}^T \mathbf{s} \mathbf{s}^H \mathbf{A}^* + \mathbf{A}^T \mathbf{s} \tilde{\boldsymbol{\nu}}^H + \tilde{\boldsymbol{\nu}} \mathbf{s}^H \mathbf{A}^* + \tilde{\boldsymbol{\nu}} \tilde{\boldsymbol{\nu}}^H \} \\
&= E \{ \mathbf{A}^T \mathbf{s} \mathbf{s}^H \mathbf{A}^* \} + E \{ \mathbf{A}^T \mathbf{s} \tilde{\boldsymbol{\nu}}^H \} + E \{ \tilde{\boldsymbol{\nu}} \mathbf{s}^H \mathbf{A}^* \} + E \{ \tilde{\boldsymbol{\nu}} \tilde{\boldsymbol{\nu}}^H \}
\end{aligned} \tag{2.21}$$

The noise is assumed to be zero mean and independent of the multipath profile, so the equation above becomes:

$$E \{ \tilde{\mathbf{y}} \tilde{\mathbf{y}}^H \} = E \{ \mathbf{A}^T \mathbf{s} \mathbf{s}^H \mathbf{A}^* \} + E \{ \tilde{\boldsymbol{\nu}} \tilde{\boldsymbol{\nu}}^H \} \tag{2.22}$$

Expansion of $E \{ \tilde{\mathbf{y}}(l) \tilde{x}(l)^* \}$

The expectation term on the right side of (2.20), is expanded:

$$\begin{aligned}
E \{ \tilde{\mathbf{y}} \tilde{x}^* \} &= E \{ (\tilde{\mathbf{u}} + \tilde{\boldsymbol{\nu}}) \tilde{x}^* \} \\
&= E \{ \tilde{\mathbf{u}} \tilde{x}^* + \tilde{\boldsymbol{\nu}} \tilde{x}^* \} \\
&= E \{ \tilde{\mathbf{u}} \tilde{x}^* \} + E \{ \tilde{\boldsymbol{\nu}} \tilde{x}^* \} \\
&= E \{ \tilde{\mathbf{u}} \tilde{x}^* \}
\end{aligned} \tag{2.23}$$

The last step is due to the assumption that the noise is zero mean and is independent of multipath profile. We are left with the cross-correlation between the input and output of a linear system, whose transfer function is known (it is the transfer function of the transmitted waveform). The input-output cross correlation for a linear system is the convolution of the

system's impulse response with the autocorrelation of the system's input [10].

$$E \{ \tilde{\mathbf{u}} \tilde{x}^* \} = E \{ \tilde{x} \tilde{x}^* \mathbf{s} \} = E \{ \tilde{x} \tilde{x}^* \} \mathbf{s} \quad (2.24)$$

Expanded Form of \mathbf{w}_o

The optimum weight vector from (2.20) is now written as:

$$\mathbf{w}_o = \left(E \{ \mathbf{A}^T \mathbf{s} \mathbf{s}^H \mathbf{A}^* \} + E \{ \tilde{\nu} \tilde{\nu}^H \} \right)^{-1} E \{ \tilde{x} \tilde{x}^* \} \mathbf{s} \quad (2.25)$$

Note that in making the above substitutions, the input data, \tilde{y} is no longer explicitly part of the weight solution, and has been replaced with terms dependent on the multipath profile, \tilde{x} .

Noise Covariance Matrix

Defining the noise covariance matrix, \mathbf{R} to be:

$$\mathbf{R} \triangleq E \{ \tilde{\nu} \tilde{\nu}^H \} \quad (2.26)$$

Then (2.25) is rewritten:

$$\mathbf{w}_o = \left(E \{ \mathbf{A}^T \mathbf{s} \mathbf{s}^H \mathbf{A}^* + \mathbf{R} \} \right)^{-1} E \{ |\tilde{x}|^2 \} \mathbf{s} \quad (2.27)$$

The noise is assumed to be white Gaussian noise. Consequently, \mathbf{R} is the identity matrix scaled by the noise power.

Signal Covariance Matrix

The signal covariance matrix, \mathbf{C}_1 is defined:

$$\mathbf{C}_1 \triangleq E \{ \mathbf{A}^T \mathbf{s} \mathbf{s}^H \mathbf{A}^* \} \quad (2.28)$$

The power estimate of the multipath profile at a given lag is defined to be

$$\rho \triangleq E \{ \tilde{x} \tilde{x}^* \} = \hat{x} \hat{x}^* \quad (2.29)$$

It is assumed that neighboring lag cells are uncorrelated. The estimate of the element in the m^{th} row and n^{th} column of \mathbf{C}_1 is therefore:

$$E \{ C_{1,mn} \} \triangleq \sum_{i=\kappa_L}^{\kappa_U} \rho(l-i+m-1) s_i s_{i-m+n}^* \quad (2.30)$$

Where the lower summation bound is

$$\kappa_L = \max \{ 0, m - n \} \quad (2.31)$$

and the upper summation bound is

$$\kappa_U = \min \{ N - 1, N - 1 + m - n \} \quad (2.32)$$

The matrix indices, m and n are the 1-based indices of the rows and columns of \mathbf{C}_1 , respectively.

An alternative expression may be used to write 2.30 in terms of the full \mathbf{C}_1 matrix:

$$\mathbf{C}_1 = \sum_{n=-N+1}^{N-1} \rho(l+n) \mathbf{s}_{\rightarrow n} \mathbf{s}_{\rightarrow n}^H \quad (2.33)$$

where $\mathbf{s}_{\rightarrow n}$ corresponds to the waveform replica vector shifted by n samples with the remaining elements set to 0. For instance:

$$\mathbf{s}_{\rightarrow 2} = \begin{bmatrix} 0 \\ 0 \\ s_0 \\ \vdots \\ s_{N-3} \end{bmatrix} \quad (2.34)$$

This particular form is useful for generating true covariance matrices in simulations.

RMMSE Optimum Weights

The results of the previous sections are combined to give the RMMSE weights:

$$\mathbf{w}_o = (\mathbf{C}_1 + \mathbf{R})^{-1} \mathbf{s} \rho \quad (2.35)$$

where the m^{th} , n^{th} element of \mathbf{C}_1 is given by 2.30

2.4.3 RMMSE Implementation

The RMMSE weights in (2.35) depend on ρ . Recall that in (2.29), ρ is the expected power of the multipath profile at the given lag. The multipath profile, \tilde{x} is unknown and is the quantity that is being estimated. The RMMSE authors chose to address this through iterative estimation. An initialization stage generates an estimate of \tilde{x} using non-adaptive weights. The initialization weights are similar to matched filter weights. This initial estimate is then used to adaptively re-estimate \tilde{x} . This process repeats several times until the weights converge. The flow diagram in Figure 2.5 illustrates this iterative process.

There is currently no criteria for exiting the iteration loop. The algorithm authors

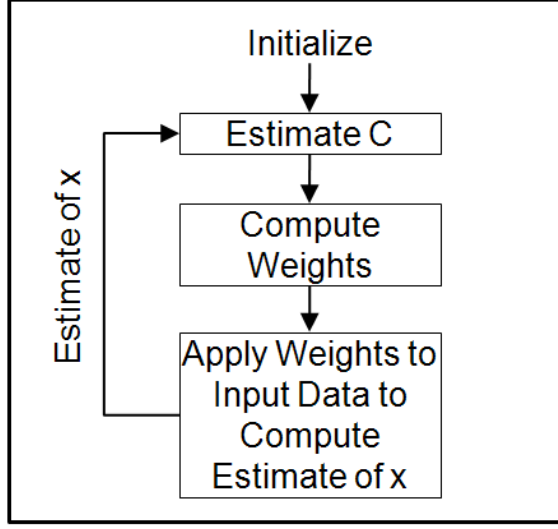


Figure 2.5: RMMSE iteration process. Following an initialization stage, weights are iteratively computed to generate a new estimate

indicate that 3-4 iterations provide convergence, and this has been verified in simulation. The final item in the RMMSE derivation is the initial estimate of \tilde{x} . For this step, it is assumed that the noise is negligible and all \tilde{x} values are equal. This assumption results in an initialization signal covariance matrix \mathbf{C}_{init} that does not depend on \tilde{x} .

$$C_{\text{init},mn} = \sum_{i=\kappa_L}^{\kappa_U} s_i s_{i-m+n}^* \quad (2.36)$$

The initialization weights are set:

$$\mathbf{w}_{\text{init}} = (\mathbf{C}_{\text{init}})^{-1} \mathbf{s} \quad (2.37)$$

The initialization weights are the same regardless of lag value, so this stage may be implemented with a fast convolution process.

2.4.4 Gain Constrained RMMSE

In [11], the weight derivation leading to (2.35) is modified slightly to incorporate a unity gain constraint. The resulting weights have the familiar MVDR scale factor [12]:

$$\mathbf{w}_{\text{unity gain}} = \frac{(\mathbf{C}_1 + \mathbf{R})^{-1} \mathbf{s}}{\mathbf{s}^H (\mathbf{C}_1 + \mathbf{R})^{-1} \mathbf{s}} \quad (2.38)$$

For this variation, the initialization weights are the matched filter weights, as the matched filter is derived to satisfy the unity gain constraint [3].

2.5 RMMSE Operational Description

The goal of this section is to introduce several operational descriptions of the RMMSE algorithm. These examples provide additional insight to the algorithm and the effect of the adaptive weights.

2.5.1 Filter Convergence

The RMMSE weights are computed independently at each lag value and iteration. There is no averaging of the input correlation matrix as commonly seen in the LMS algorithm [8]. Algorithm convergence, rather, is obtained by iterating over the same input data multiple times. The weights depend on the transmitted waveform replica and the previously computed power estimates. The power estimate is refined through iterations.

Even though the algorithm does not converge in exactly the same manner as the LMS algorithm, the quadratic performance surface visualization from [8] may still be used to describe algorithm performance at a given lag. The left plot of Figure 2.6 shows the RMMSE output at several iteration stages. The right plot shows the quadratic performance surface at the lag indicated by the black box. The solid black line on the performance surface shows the progression of two weights as the RMMSE algorithm iterates. There are two signals

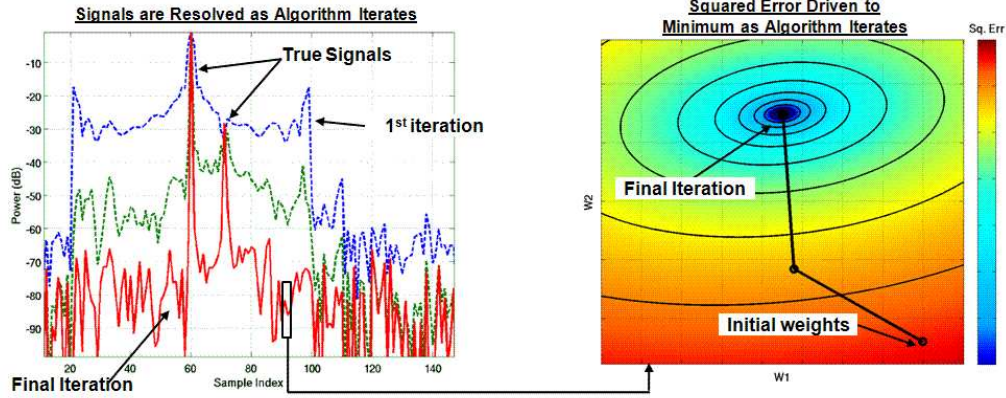


Figure 2.6: RMMSE convergence illustration. Left plot: RMMSE results through iteration stages. Right plot: Squared error at given lag value minimized as algorithm iterates.

present in the simulation, as indicated by the arrows in the left plot. The initial weights lead to relatively high error, indicated by the blue line on the RMMSE output. Through the iterations, the RMMSE output converges to the red line where the two signals are clearly visible. At this iteration, the weights approach the minimum point of the performance surface.

2.5.2 Cross Correlation Effects of Adaptive Weights

The RMMSE algorithm generates a unique weight vector for each lag cell. The effects of these weights on signals arriving from other lags are easily visualized by cross correlating the RMMSE weights against the replica vector. A simple simulation is shown in Figure 2.7. A signal arrives at lag=0 seconds. Figure 2.7(a) shows the matched filter (blue) and RMMSE (red) outputs for this case. The matched filter output peaks in the correct location, but suffers from time sidelobes around the peak. The RMMSE output correctly locates the peak and suppresses the sidelobes. The RMMSE weights from lag=-0.05 seconds were used to generate Figure 2.7(b). In this figure, there is a deep null located at lag=0, which corresponds to the arrival time of the strong signal. It is also seen in Figure 2.7(b) that

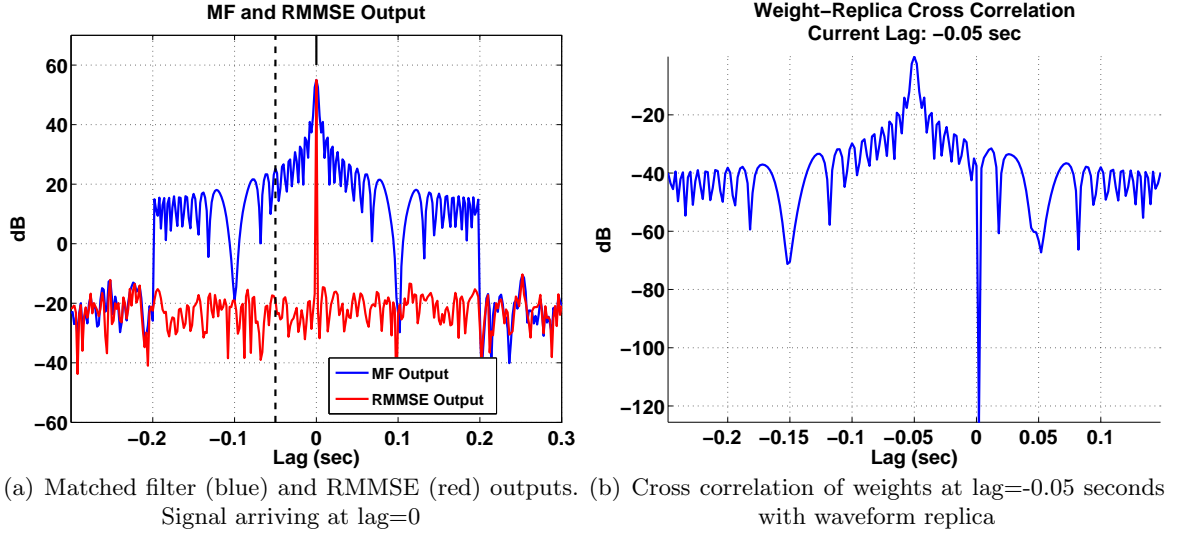


Figure 2.7: Illustration of the null created by the weights at lag=-0.05 seconds to cancel the signal arriving at lag=0 seconds

the adaptive weights pass any signals arriving from lag=-0.05 seconds. There is no signal at this lag, and the corresponding RMMSE output approaches the noise floor, as seen in Figure 2.7(a) at the lag indicated by the dashed vertical black line. This analysis is similar to the use of beampatterns in adaptive beamformer analysis.

2.6 RMMSE Topics in Literature

Since the original publication of the RMMSE algorithm in 2003, there have been numerous subsequent publications related to the algorithm. The related papers can be divided into five major categories, with varying amounts of work devoted to each:

- General RMMSE
- Processing Time Enhancements
- Algorithm Robustness
- Multistatics and Shared Spectrum

- Additional Applications

2.6.1 General RMMSE Papers

The original publication of the RMMSE algorithm is found in [1]. In this paper, the authors present the algorithm, along with simulation results showing algorithm performance on single point scatterers. A detailed derivation is not explicitly provided, but the authors provide enough information to recreate the derivation of the algorithm.

In [13], the authors extend the RMMSE simulation results to show algorithm performance in dense target scenarios. The authors also show that the algorithm is sensitive to Doppler distortion, but still has superior performance to other algorithms in the presence of such distortion. The authors describe additional RMMSE capabilities in [14]. In particular, they show how the RMMSE algorithm may be used to resolve weak returns that would otherwise be masked by range sidelobes. Again, it is shown that the algorithm is sensitive to Doppler effects, but the performance is superior to other algorithms under consideration.

In [15], and [16] it is shown that the RMMSE algorithm can successfully be applied to matched filter output. This allows the algorithm to be run on systems where it is not possible to obtain data prior to matched filtering. Finally, in [17], the authors present algorithm results obtained in a test scenario. Several synthetic test targets were injected into receive processing hardware, and it was shown that the RMMSE results closely match the performance predicted by simulations.

2.6.2 Processing Time

There have also been publications related to the processing speed of the RMMSE algorithm. The first instance is found in reference [18] and extended in [19] where two Fast Adaptive Pulse Compression (FAPC) algorithm variants are developed. These are reduced-rank approaches. It is shown that both FAPC approaches reduce computation time by an order of magnitude over the original RMMSE algorithm. It is also shown that one of the FAPC approaches improves performance in the presence of Doppler distortion due to shorter time

windows.

2.6.3 RMMSE Robustness

In [20] and [21], two approaches are presented for making the RMMSE algorithm insensitive to Doppler mismatch. The two approaches are termed “Doppler compensation” (DC) and “single pulse imaging” (SPI). In the DC approach, the Doppler shift is modeled as a constant phase shift for each sample of the replica. During each iteration of the algorithm, a Doppler phase shift is estimated and applied. In the SPI approach, a bank of Doppler shifted replicas is used. The RMMSE algorithm is run on all Doppler hypotheses and the signal outputs are compiled. The filter output with the highest SNR is chosen as the true output.

In [11], the RMMSE algorithm is presented with a distortionless constraint. The authors state that the purpose of this formulation is to combat signal suppression that can occur in the FAPC approaches.

2.6.4 Multistatics and Shared Spectrum Processing

There have been a significant number of publications related to multistatic and shared spectrum processing using the RMMSE algorithm. The multistatic generalization of RMMSE is presented in [22] and extended in [23] and [24]. It is shown that the RMMSE approach may be used in multistatic scenarios for time of arrival information. It is also shown to enhance signal detection performance in shared-spectrum settings. In [25] the authors further extend the RMMSE architecture by jointly performing adaptive pulse compression and adaptive beamforming, which is further discussed in [26]. Other references in this area of interest are [27] and [28].

2.6.5 Additional Applications

There are several papers related to the RMMSE approach that do not fit into any of the above listed categories. In [29], the authors show that the RMMSE approach may be used

to achieve super-resolution. It is demonstrated via simulation that the RMMSE algorithm can resolve signal arrivals at time resolutions greater than the A/D sample rate.

The RMMSE authors also show how the RMMSE approach may be utilized for direction of arrival (DOA) processing in references [30] and [31].

Other authors not directly affiliated with Blunt and Gerlach have also contributed to the RMMSE literature. In [32], a RMMSE architecture is developed for Stepped Frequency Continuous Wave (SFCW) radars. In [33] an approach is outlined for a 2-dimensional implementation of RMMSE.

2.7 Summary

This chapter described several aspects of the RMMSE algorithm. The signal model was established and a derivation of the algorithm was provided. The derivation was based off the papers by Blunt and Gerlach. A line-by-line derivation such as the one provided here does not currently exist in the RMMSE literature. It should be noted that Blunt and Gerlach provide all of the information and assumptions necessary to complete the derivation in their papers.

Operational descriptions of the RMMSE algorithm were also provided. It is seen that this algorithm can be visualized with adaptive beamforming or LMS techniques.

Finally, a brief survey of RMMSE literature was provided. The RMMSE algorithm and its variants are applied to a wide variety of applications, and research is currently ongoing.

Chapter 3: RMMSE Sensitivity to Mismatch and Distortion

Adaptive algorithms such as the RMMSE algorithm are developed assuming certain models. When the data characteristics match the models, adaptive algorithms generally perform well. In practice, there is frequently mismatch between the assumed models and the actual data. The goal of this chapter is to investigate the sensitivity of the RMMSE algorithm to several common forms of mismatch. A figure of merit is developed for assessing algorithm performance, and simulation results are presented.

3.1 Figure of Merit Development

In order to assess algorithm performance in the presence of distortion, it is desirable to use a Figure of Merit (FOM) as a means of “grading” the algorithm output. The FOM is ideally a measurement directly related to algorithm performance. Many simulations will be compared side-by-side, so the FOM needs to provide an immediate and intuitive indication of performance. The following paragraphs present four candidate FOMs and discuss the benefits and drawbacks of each.

3.1.1 Visual Detection

The simplest FOM is a visual detection approach. The algorithm output is displayed and the user determines whether or not the simulated signals can be visually resolved in the presence of the given distortions. For many of the distortions, the signal can either be clearly seen, or it cannot.

Since the sensitivity study compares many test cases, a visual comparison of each would be time intensive. This approach would also depend significantly on the given simulation.

Slight differences in the simulation, such as random noise initializations, may impact results. Finally, this binary yes/no result does not give an indication of overall trends.

3.1.2 Mean Squared Error

In a carefully constructed simulation the true signal covariance and signal locations are known. This allows an estimation error to be computed for each lag cell. However, after running a few candidate simulations and looking at the error performance, it was seen that this approach does not provide a direct indication of signal detectability. This metric is more suitable for investigating individual cases and digging deeper into a specific result.

3.1.3 Mean Sidelobe Level

The sidelobe levels in the algorithm output provide a useful indication of signal detectability. The average sidelobe level approximately describes the noise floor of the algorithm output.

The average signal power was measured in the region surrounding the primary signal. The extent of the region was matched to the expected duration of the matched filter sidelobes, essentially $\pm T$, where T is the duration of the pulse in seconds. The area outside of the time domain sidelobes was not included so as to not artificially decrease the average. Areas surrounding the expected location of the signals were excluded so they would not artificially raise the average. The region used for averaging is indicated by the horizontal black bars in Figure 3.1

The measured mean sidelobe levels for both the matched filter and RMMSE algorithms are compared against each other. A low RMMSE mean sidelobe level relative to the matched filter indicates that the RMMSE algorithm is suppressing sidelobes. This FOM performs reasonably well in benign distortion cases. As the distortion becomes more severe, the dynamic range of the sidelobes (often tens of dB) tends to drive the value of the mean artificially up.

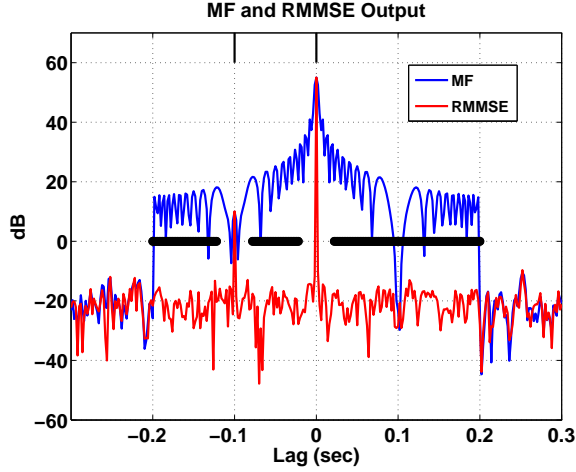


Figure 3.1: Region used to obtain average sidelobe levels indicated by black horizontal bars. The region does not extend beyond the autocorrelation sidelobes and is notched near the true signal locations

3.1.4 Median Sidelobe Level

The median sidelobe level was investigated as an alternative to the mean sidelobe level. The same averaging region described by Figure 3.1 is used to compute the median sidelobe level. The median is found to be less sensitive to the dynamic range of the sidelobes. The median level tends to be much closer to the visual estimate of the sidelobe levels than the mean.

Figure 3.2 compares the results of mean and median averaging. The solid red line indicates RMMSE output. The vertical blue lines indicate the region over which the average is computed. The horizontal dashed black line shows the computed mean sidelobe level in the averaging region, and the horizontal dashed red line shows the median sidelobe level. The mean sidelobe level is driven up by the region immediately surrounding the primary signal, and the mean level is significantly higher than most of the averaging region. The median estimate, however, appears to provide a more reliable indication of overall sidelobe performance.

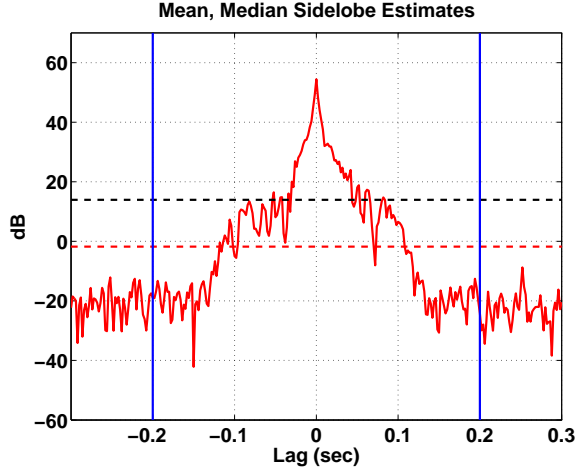


Figure 3.2: Comparison of mean and median sidelobe estimation levels in a severe distortion case. The mean sidelobe level (dashed black line) is raised by the dynamic range of the sidelobes. The median sidelobe level (dashed red line) is less sensitive to these effects.

3.1.5 Selected FOM

The Median Sidelobe Level is selected as the primary FOM for assessing RMMSE performance. This approach gives the best indication as to the ability to detect signals. In subsequent paragraphs and plots, the Median Sidelobe Level is abbreviated MSL.

3.2 Simulation Settings

There are two characterization simulations that are shown prior to investigating distortions:

- Baseline simulation: No distortion, signals at 55 dB and 10 dB
- Signal power sweep: Sweep signal from 10 dB to 210 dB, no distortion

The baseline simulation is performed to illustrate algorithm performance in a perfect simulation and provide a benchmark for later tests. The variation of the primary signal power is performed to show that RMMSE performance does not change significantly with signal

Table 3.1: Parameters used in simulated waveform

	Value	Units	Symbol
Bandwidth	200	Hz	β
Duration	0.2	sec	T
Center frequency	5000	Hz	f_c
Sample Rate	500	Hz	f_s

power.

There are many forms of distortion that can affect a pulsed sonar waveform. Several common distortions are simulated:

- Intrsample arrival: Time mismatch
- Doppler distortion: Phase and frequency mismatch
- Transducer distortion: Frequency dependent amplitude mismatch

These distortions are chosen because they represent differing yet important sources of mismatch. Other distortions that are not investigated can often be represented as a combination of these distortions. For instance, changes in the speed of wave propagation can be approximately modeled as a Doppler shift. Frequency dependent sound channel attenuations can be modeled as transducer distortions.

For all simulations, there are two signals present in the data. The primary signal is located at lag $t = 0$ seconds, and the secondary signal is located at lag $t = -0.1$ seconds. Unless otherwise stated, the primary signal power is 55 dB and the secondary signal power is 10 dB. The input noise power is set to 0 dB. The speed of sound is 1500 m/s. A linear frequency modulated (LFM) waveform is used, with a positive frequency sweep. The waveform parameters are summarized in Table 3.1.

The complex basebanded LFM at time t is given by:

$$s(t) = e^{j2\pi\left(-\frac{\beta t}{2} + \frac{\beta t^2}{2T}\right)} \quad 0 \leq t < T \quad (3.1)$$

The number RMMSE of iterations, M , is set to 4. The RMMSE variant used is the unity gain RMMSE defined in (2.38).

3.2.1 Level Calibration

For the selected waveform, approximately 20 dB of signal gain is expected from the matched filter. To preserve signal strength, the matched filter and RMMSE results are calibrated so that the signal strengths are maintained and the noise floor is effectively “pushed down”. Therefore, in plots showing matched filter or RMMSE output, the signal power levels are at 55 dB and 10 dB. The output noise level is at -20 dB. The plots showing MSL estimates versus distortion settings are calibrated relative to the noise level at the output of the matched filter. In these plots, an MSL of 0 dB indicates that the output MSL matches the noise level at the matched filter output.

3.3 Simulation Results

3.3.1 Baseline Simulation

The first simulation shown is a “baseline” case to illustrate algorithm performance in the absence of distortion.

Setup

The received signals are modeled to match the waveform replica exactly.

Results

Figure 3.3 shows the results of the baseline simulation. There is a primary strong signal at lag $t = 0$ seconds. The secondary signal is at lag $t = -0.1$ seconds. The solid black tick marks at the top of the plot denote the true locations of the input signals. In the matched filter output (blue line) the primary signal is the only signal that can be resolved. Both signals are seen clearly in the RMMSE output. The dashed blue line represents the

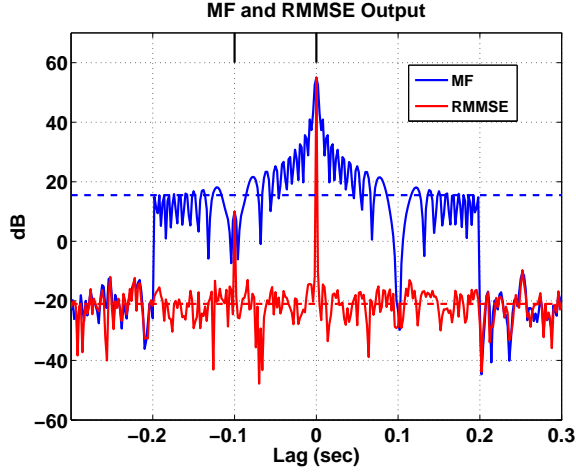


Figure 3.3: RMMSE (red) and Matched Filter (blue) outputs for the baseline simulation

MSL of the matched filter, and the dashed red line represents the MSL of the RMMSE algorithm. For this case, the RMMSE MSL is at approximately the same level as the noise floor, whereas the matched filter MSL is approximately 38 dB above the noise floor.

Summary

The baseline performance of the RMMSE algorithm is very promising. The matched filter sidelobes are completely suppressed, and the secondary signal can be detected easily. The RMMSE algorithm provides a clear improvement over current state of the art capabilities in active sonar pulse signal processing.

3.3.2 Signal Power Sweep

While not technically a form of distortion, the effect of signal strength on MSL is investigated next. This simulation is performed to determine if the RMMSE algorithm maintains performance for all reasonable signal powers.

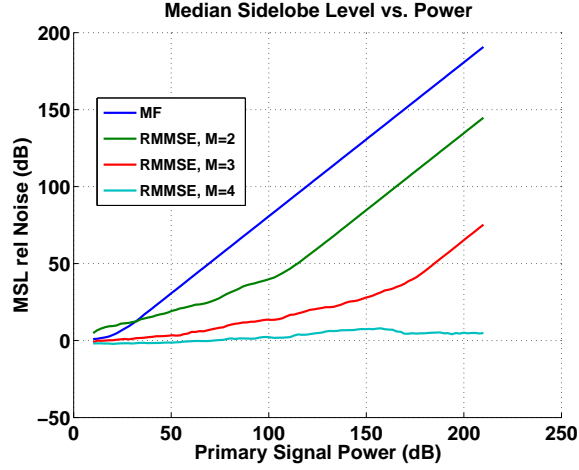


Figure 3.4: MSL as a function of signal power for matched filter and RMMSE

Setup

In this simulation, the primary signal power is varied from 10 dB above the nominal noise floor to 210 dB above the nominal noise floor. The 210 dB level is much higher than would be expected in a practical system. The data was processed through a matched filter and the MSL estimates were computed for each power step. The data was also processed through the RMMSE algorithm. For each iteration of the RMMSE algorithm (up to 4 iterations), the MSL was computed.

Results

The results of this experiment are shown in Figure 3.4. The matched filter MSL is shown in blue. The matched filter sidelobe level increases directly with the primary signal power. The RMMSE output for iterations 2, 3 and 4 are shown in green, red and cyan, respectively. Iteration 1 was omitted because it is a non-adaptive initialization stage and closely follows the matched filter in terms of sidelobe performance.

As the algorithm progresses through iterations, the sidelobes are suppressed relative to

the matched filter output. By the fourth iteration, the RMMSE algorithm has reduced the sidelobes down to the noise floor level for signal powers up to 210 dB. There is a slight increase in MSL for SNRs above 100 dB in the fourth iteration.

Summary

The RMMSE algorithm performs well across a wide range of signal to noise ratios. As the algorithm progresses through iterations, the MSL is decreased to the level of the noise floor. For SNRs greater than 100 dB, there is a slight increase in MSL at the output of the fourth iteration. Additional iterations can provide additional reduction in MSL, but such high SNRs are not expected in practical systems.

3.3.3 Intrsample Arrival

In the baseline simulation, a waveform replica is generated, scaled, and inserted into the receive data. The same, unscaled replica is used in the matched filter and RMMSE algorithms. Aside from the scale factor, the replica matches the waveform exactly. This implies that the rising edge of each pulse arrives at the receiver at the exact same time that an A/D sample is taken. The probability of this occurring is vanishingly small. It is much more likely that the rising edge of the pulse arrives somewhere between clock samples. This behavior is termed “intrsample arrival” and is virtually guaranteed in a real system.

Setup

There are several ways that this behavior can be simulated. The LFM waveform is computed in closed form so the most direct method for modeling this distortion is by using a time offset in equation (3.1). The time offset is chosen so that the true rising edge of the waveform occurs between A/D samples. The time shifted LFM is used to generate the simulated received data, and an unshifted LFM is used in as the waveform replica.

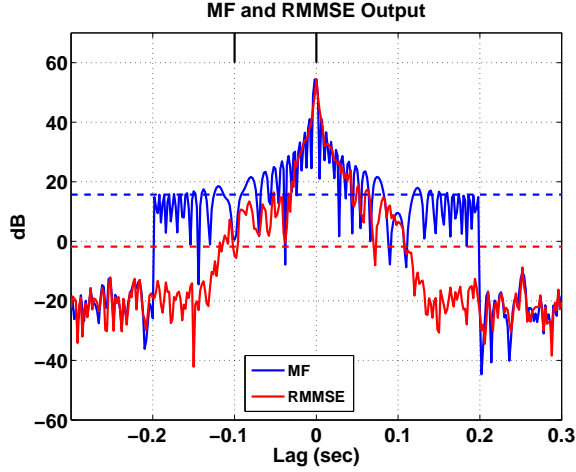


Figure 3.5: RMMSE and matched filter output when the rising edge of the primary signal arrives halfway between A/D samples

Results

Figure 3.5 shows the results of setting the rising edge of the primary signal halfway between A/D samples. RMMSE performance is clearly degraded relative to the baseline case. The MSL has increased nearly 20 dB, and the secondary signal is no longer visually detectable. The RMMSE sidelobes are still well below the matched filter sidelobes. It is possible that other secondary signals can be detected using the RMMSE algorithm (for instance, a signal arriving at $t = -0.15$ can be detected), but the selected secondary signal cannot.

Next, the secondary signal was subject to the same intrasample arrival. The primary signal arrives on an A/D sample. The results are shown in Figure 3.6. In this case, the RMMSE performance is very close to the baseline performance. While the mainlobe of the secondary signal does appear to be slightly widened relative to the baseline, it is clearly visible. Any sidelobes that would mimic the sidelobes seen in Figure 3.5 are below the noise floor and cannot be seen.

The intrasample arrival distortion was simulated over the full range of time offsets. The results of this simulation are shown in Figure 3.7. The x -axis of these plots corresponds to

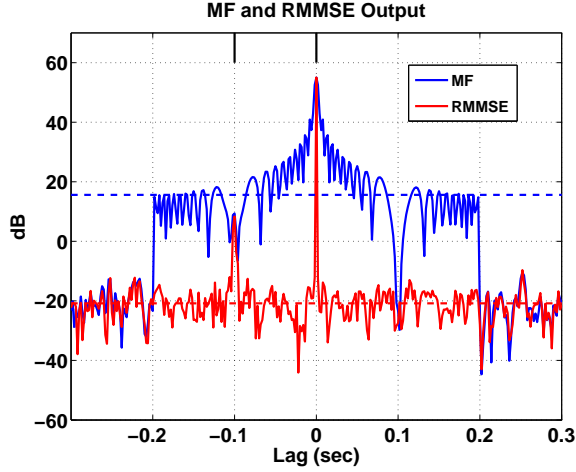


Figure 3.6: RMMSE and matched filter output when the rising edge of the secondary signal arrives halfway between A/D samples

a normalized distance between samples. An x -axis value of 0.5 corresponds to the rising edge of the pulse arriving exactly between A/D samples. An x -axis value of 0 corresponds to the rising edge arriving exactly on an A/D sample.

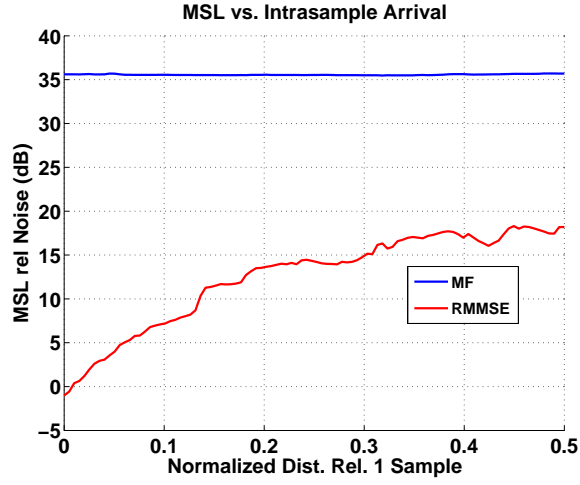
As the primary signal arrives further away from an A/D sample, MSL increases until it reaches a maximum halfway between samples, as shown in Figure 3.7(a). The MSL in Figure 3.7(b) is relatively unchanged for all time offsets.

Summary

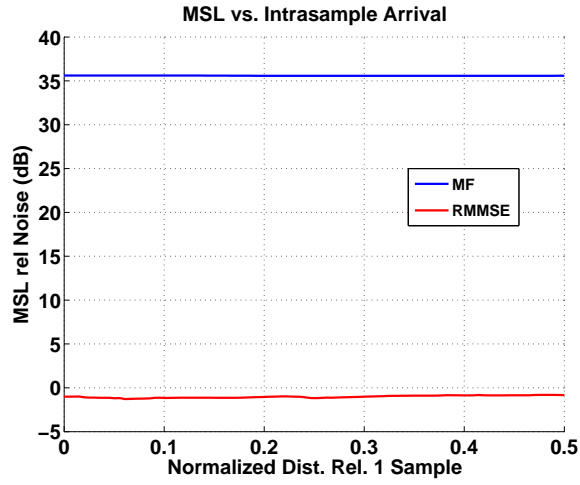
The RMMSE algorithm is sensitive to intrasample arrival. The MSL is highest when the pulse arrives halfway between A/D samples. The degradation is primarily driven by strong signals.

3.3.4 Doppler Distortion

The Doppler effect may distort a pulsed waveform when there is motion involved in transmission, reflection and/or receipt of the transmitted waveform. This results in the receiver



(a) MSL for primary signal intrasample arrival



(b) MSL for secondary signal intrasample arrival

Figure 3.7: Effect of intrasample arrival on MSL for primary and secondary signals

obtaining a waveform that is either compressed or stretched in time relative to the original signal. This form of distortion is discussed next.

Setup

The term “Doppler factor” refers to the scale factor used to describe the effects of Doppler on frequency. For the case of a signal travelling from a source to a receiver, the Doppler factor, α is given by:

$$\alpha = \frac{c + v_{r \rightarrow s}}{c - v_{s \rightarrow r}} \quad (3.2)$$

Where c is the wave propagation speed; $v_{r \rightarrow s}$ is the radial velocity of the receiver towards the source; $v_{s \rightarrow r}$ is the radial velocity of the source towards the receiver. All units are meters per second.

For modeling Doppler distortion in pulsed underwater acoustics, three main factors must be taken into account:

- The duration of the shifted pulse is scaled by $1/\alpha$
- The bandwidth of the shifted pulse is scaled by a factor of α
- The center frequency of the shifted pulse is scaled by α .

In practice, it is not generally known what Doppler effects have been imparted on a pulse. When basebanding is performed assuming a non-Doppler shifted center frequency, the Doppler shifted pulse is not basebanded correctly, resulting in modulation. The modulating frequency is denoted Δ :

$$\Delta = \alpha f_c - f_c \quad (3.3)$$

The Doppler shifted LFM is generated by first creating basebanded LFM with the Doppler

adjusted pulse duration and bandwidth

$$s_b(t) = e^{j2\pi\left(-\frac{\alpha\beta t}{2} + \frac{\alpha^2\beta t^2}{2T}\right)} \quad 0 \leq t < \frac{T}{\alpha} \quad (3.4)$$

where s_b denotes the basebanded replica. The modulated replica, s_m , is obtained from s_b using a complex exponential multiplication:

$$s_m(t) = s_b(t)e^{j2\pi t\Delta} \quad 0 \leq t < \frac{T}{\alpha} \quad (3.5)$$

The term s_m refers to the modulated replica.

The following simulations were run to simulate the Doppler effect:

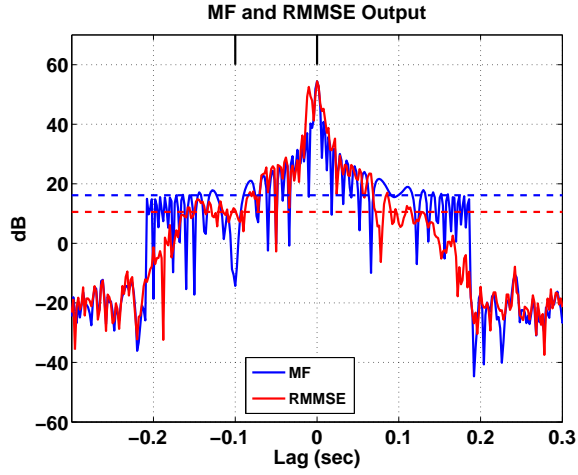
- Primary signal Doppler shifted, secondary signal stationary
- Primary signal stationary, secondary signal Doppler shifted

A monostatic source/receiver configuration is assumed. Doppler shifts were applied at range rates from -5 m/s to +5 m/s in 100 linearly spaced steps. The replica used in processing was the original, unmodified replica with no Doppler. The algorithms have no knowledge of the Doppler effect.

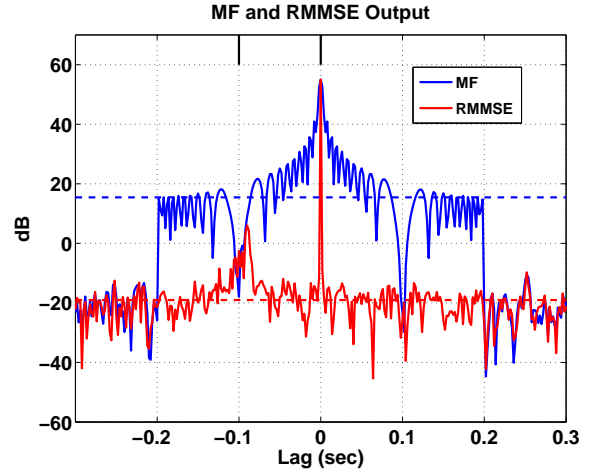
Results

Examples of algorithm performance with Doppler distortion are shown in Figure 3.8. In Figures 3.8(a) and 3.8(c), the primary signal is Doppler distorted with ± 1.5 m/s range rate, respectively. The sidelobes have raised considerably and the secondary signal is completely obscured. In Figures 3.8(b) and 3.8(d), the secondary signal is Doppler distorted with ± 1.5 m/s range rate, respectively. Both signals are clearly visible, although the response of the secondary signal is distorted.

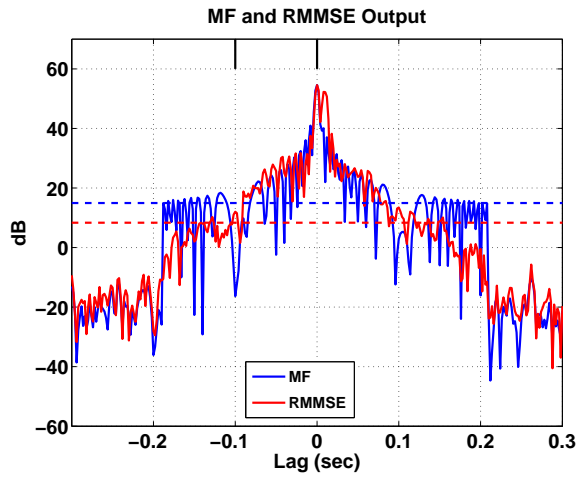
Figure 3.9(a) shows MSL as a function of primary signal Doppler distortion. The RMMSE MSL is elevated for most of the experiment space, and at times is as high as



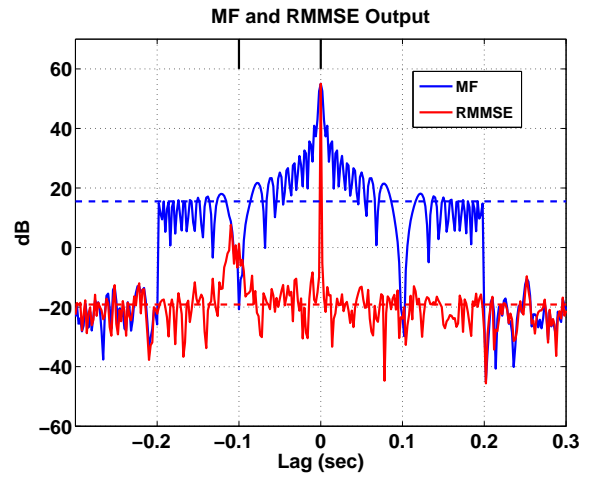
(a) Primary signal with 1.5 m/s range rate; Secondary signal stationary



(b) Secondary signal with 1.5 m/s rate rate; Primary signal stationary



(c) Primary signal with -1.5 m/s range rate; Secondary signal stationary



(d) Secondary signal with -1.5 m/s range rate; Primary signal stationary

Figure 3.8: Doppler distortion examples: Matched filter and RMMSE output

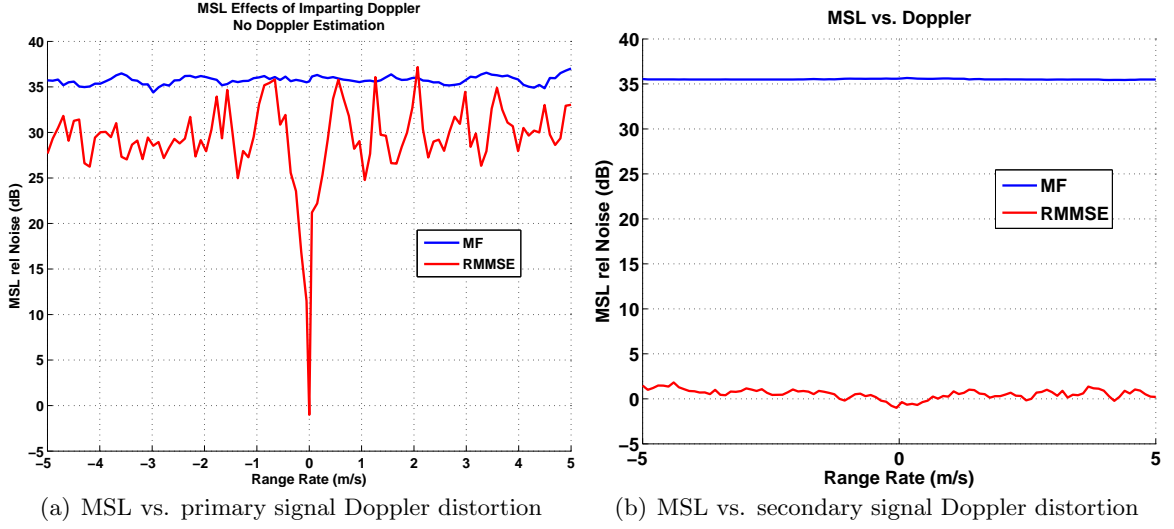


Figure 3.9: Doppler Distortion Results

the matched filter MSL. There is a very small region near 0 m/s where the RMMSE MSL is well behaved. The width of this region is approximately ± 0.04 m/s. Figure 3.9(b) shows the MSL as a function of the secondary signal. The MSL is approximately the same level as the noise floor for this experiment. Note that even though the MSL is low, Figures 3.8(b) and 3.8(d) show that the secondary signal can be significantly distorted by Doppler.

Summary

The simulations presented in this section show that the RMMSE algorithm is very sensitive to Doppler distortion. The MSL performance degrades rapidly when the primary signal is subjected to Doppler distortion. The region over which RMMSE MSL performance is well behaved is extremely narrow: ± 0.04 m/s for this simulated waveform. Though the MSL performance is better behaved when the weaker, secondary signal is Doppler distorted, the algorithm output is distorted and it is difficult to detect the secondary signal.

3.3.5 Doppler Distortion with Doppler Estimation

The results of the previous section indicate that the Doppler effect can be a limiting factor in implementing the RMMSE algorithm for use in underwater acoustics. Knowing the transmitter/receiver motion through the use of navigational logs or Global Positioning System (GPS) can potentially help alleviate the problem. Additionally, it is possible to estimate the Doppler factor from received data.

Setup

There are several options for estimating the received Doppler of a broadband waveform such as an LFM. One approach is to first transmit a narrowband, single frequency (tonal) waveform. The true Doppler factor is then accurately be estimated for the primary signal through the use of the Fourier transform.

When the dual-transmission capability is not available or is undesirable, then it is also possible to estimate Doppler through the use of a time-Doppler ambiguity surface. In this approach, the received data is cross-correlated against a bank of Doppler shifted replicas. The replica with the highest cross-correlation result is then used as the replica for processing.

For this simulation, the time-Doppler ambiguity surface approach is selected. A bank of Doppler adjusted replicas was generated for processing. The replica with the best match (highest cross-correlation) to the received data was used in adaptive processing. The candidate Dopplers were selected such that they did not exactly match any of the simulated Dopplers. This guarantees that there is always some amount of Doppler mismatch between the replica and the data.

Results

A sample time-Doppler ambiguity surface is shown in Figure 3.10. In this case, the Doppler factor of the primary signal corresponds to a range rate of 1.5 m/s. The peak of the surface is indicated by the solid black circle. The location of this peak is then used to generate the

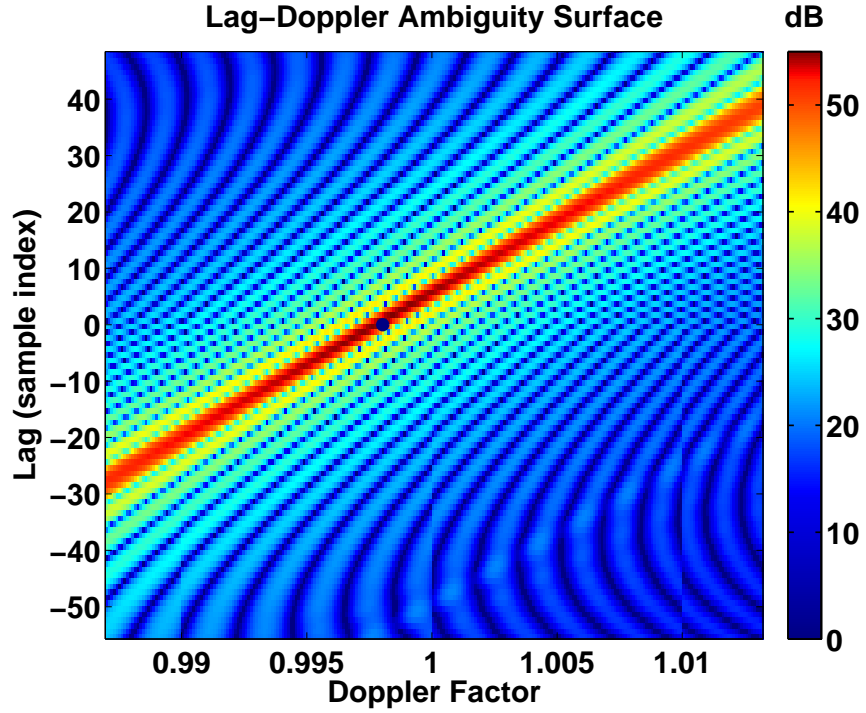


Figure 3.10: Example Ambiguity Surface

waveform replica in subsequent processing.

Figure 3.11(a) shows the algorithm output when no Doppler estimation is applied. In this case, the primary signal has been Doppler distorted by a range rate of 1.5 m/s. Figure 3.11(b) shows the results for the same case when Doppler estimation is performed using the time-Doppler ambiguity surface approach.

Figure 3.12(a) shows the absolute Doppler estimation error for this simulation. The range rate was estimated to within ± 0.04 m/s. The MSL for this simulation is shown in Figure 3.12(b). The MSL has been improved considerably relative to the results shown in Figure 3.9(a). The distribution of MSL with respect to Doppler estimation error is shown in Figure 3.12(c). As expected, the MSL is directly related to the Doppler mismatch.

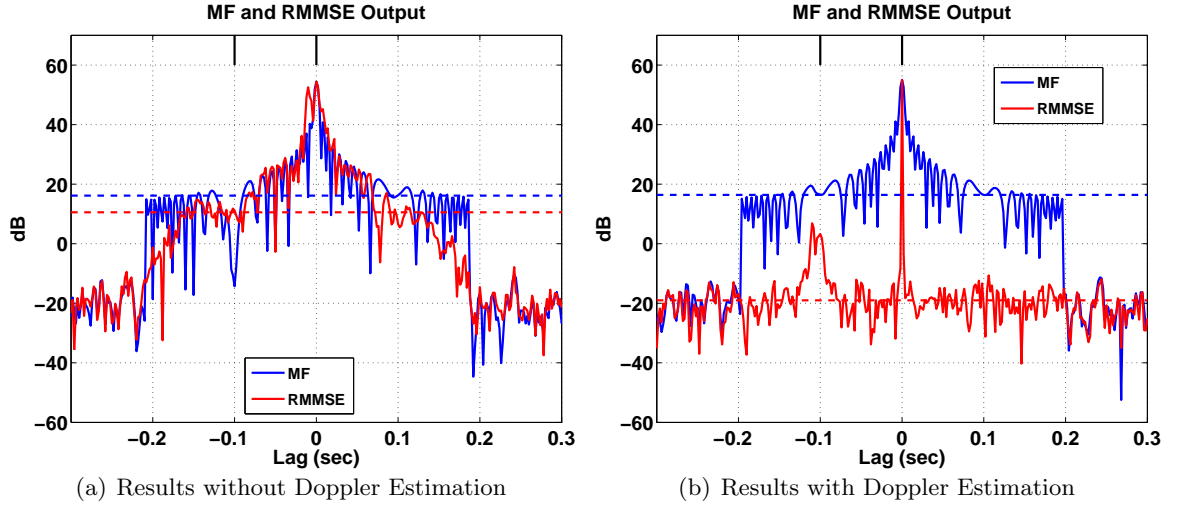


Figure 3.11: Algorithm Output for Primary Signal with +1.5 m/s range rate, opening

Summary

The effects of Doppler distortion can be mitigated through Doppler estimation. Performance improves as estimation error decreases. The steep slope of the notch in Figure 3.9(a) indicates that small errors in Doppler estimation can lead to significant variations in MSL. The accuracy required to achieve acceptable MSL performance may not be possible in a practical system.

An additional consideration in the application of this technique is the presence of multiple signals with different range rates. Only one Doppler factor can be estimated and processed by the RMMSE algorithm. This is seen in Figure 3.11(b) where the Doppler of the primary signal has been correctly compensated, but the Doppler of the secondary signal has not. This leads to distortion of the secondary signal. In many practical cases, it is not expected to receive signals with overlapped time responses and significantly different Dopplers such as seen in Figure 3.11(b). This assertion is based on the assumptions that pulse lengths are typically short (on the order of 1 to 2 seconds or less) and that signals have been spatially separated through beamforming or other techniques. It is not likely to

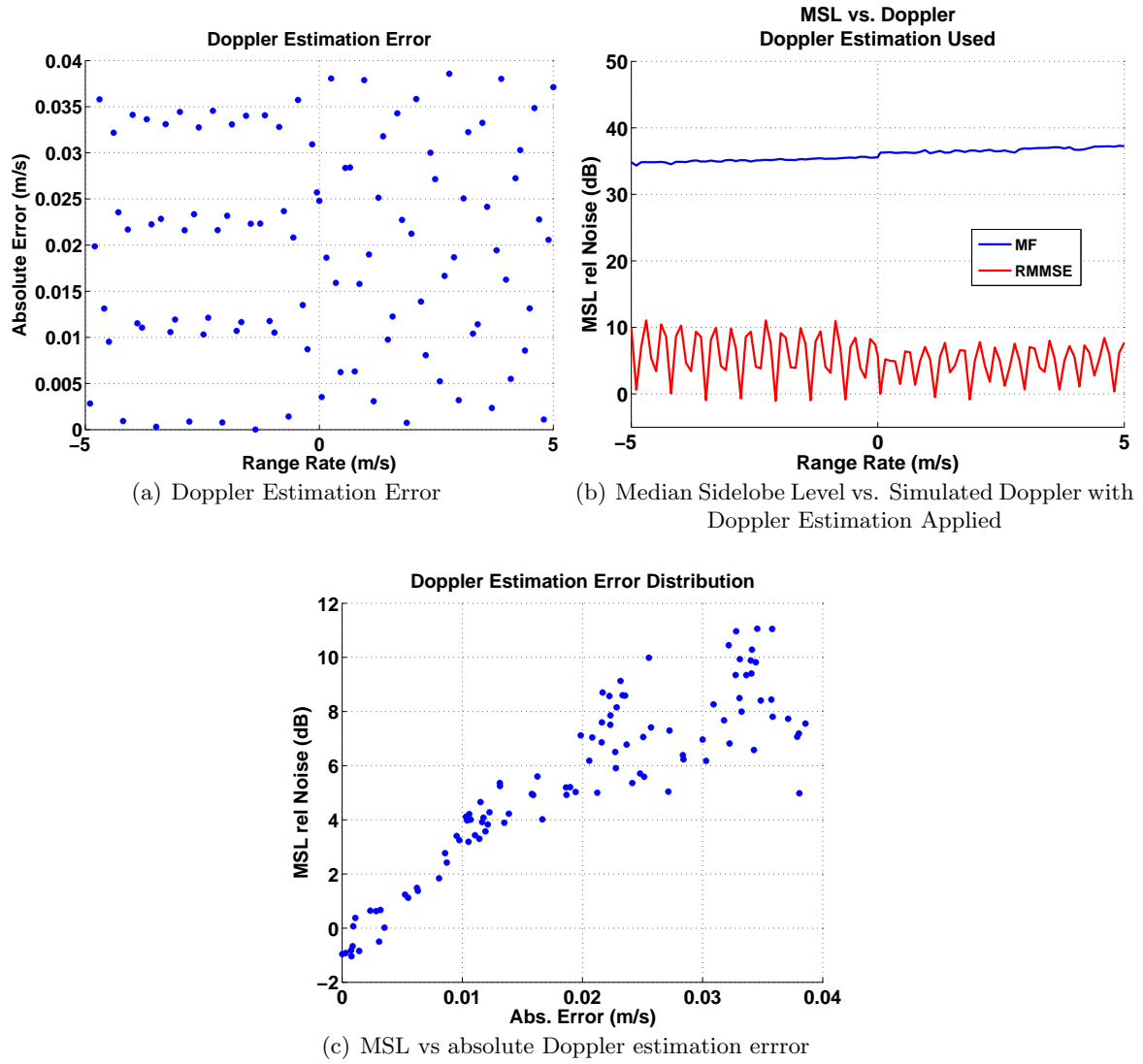


Figure 3.12: Effects of Doppler estimation on RMMSE processing

have multiple reflectors located very close to each other spatially and moving in significantly different directions. It is more likely that such overlapped signals are due to multipath or are multiple point reflections from a distributed surface such as the ocean floor. In cases such as these, the received Doppler factor will not vary significantly between signals. It is assumed in subsequent discussion regarding Doppler that signals spaced relatively close to each other have similar Doppler factors.

3.3.6 Uncalibrated Transducer Distortion

The transmit and receive transducers transfer functions are investigated as a source of signal-replica mismatch. Ideally, the transfer function of the transducers passes all frequencies with unity gain. In practice, this may not be the case. The issue of acoustic transducer calibration is discussed in [4]. This section assumes that the transducer calibration is either unknown or inaccurate.

Setup

The undistorted transducer transfer function is modeled as a bandpass filter with band start and stop edges matched to the transmitted waveform. The passband has unity gain. The corresponding frequency amplitude response is illustrated in Figure 3.13(a). The bandpass edges, denoted as f_{start} and f_{stop} correspond to frequencies of the rising and falling edges of the LFM pulse, respectively. Figure 3.13(b) shows the transfer function of the uncalibrated transducer. The passband now has a ramp-like behavior. The amplitude of the band start edge, f_{start} has a gain of μ instead of unity. The gain increases linearly with frequency until f_{stop} , where unity gain is achieved. Since the waveform of interest is an LFM, the frequency domain attenuation may be modeled easily in the time domain. This is accomplished by applying a time domain amplitude shading to the waveform. The shading function, $\psi(t)$ is

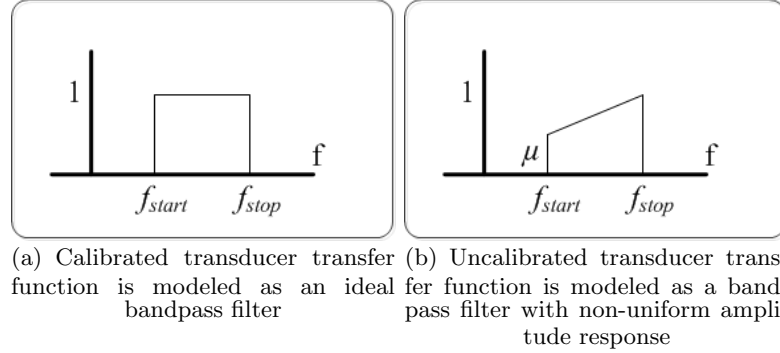


Figure 3.13: Modeled transfer functions for calibrated and uncalibrated transducers

written in slope-intercept form:

$$\psi(t) = \frac{1-\mu}{T}t + \mu \quad 0 \leq t < T \quad (3.6)$$

and is applied directly to the waveform, $s(t)$ through point-by-point multiplication (Hadamard product). This method was selected for implementation. For the simulation, μ was swept from 0.01 to 1.00 in 100 steps. The replica used in matched filter and RMMSE processing was unshaded.

Results

Figure 3.14 shows the processing results. Figure 3.14(a) shows the matched filter and RMMSE output for $\mu = 0.5$. While the RMMSE sidelobes are still lower than the matched filter sidelobes, the RMMSE performance has degraded and the secondary signal is barely visible. Figure 3.14(b) shows the MSL estimate for all of the cases considered. The most severe value of μ has an initial attenuation of 40 dB. In that case, the RMMSE MSL level is 15 dB above the noise floor, and the secondary signal is not visually detectable. As the distortion becomes less severe, the performance improves. The secondary signal becomes visually detectable when μ is approximately 0.5.

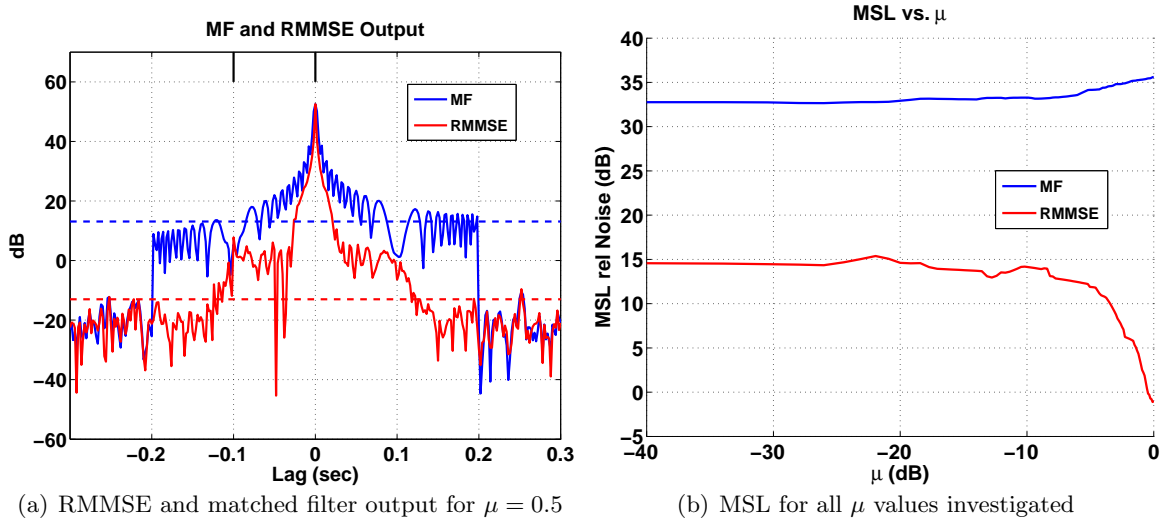


Figure 3.14: Effects of uncalibrated transducers on RMMSE processing

Summary

Uncalibrated transducer effects lead to degradation in RMMSE performance. For the transfer function investigated, the distortion leads to an MSL increase of as much as 15 dB. It is not necessarily expected to have transducers with a ramp-type of transfer function as used in this simulation. In reality, the transducer transfer functions could be more complex. The range of μ values over which this simulation was performed are believed to provide a reasonable indication of performance in a wide variety of cases.

3.4 Sensitivity Study Summary

In this chapter, a number of simulations have been presented in order to characterize RMMSE performance in the presence of mismatch and distortion. The median sidelobe level is chosen as the figure of merit for assessing algorithm performance. The selected distortions model behavior that is expected in real sonar systems. The RMMSE algorithm is sensitive to intrasample arrival, Doppler distortion and transducer distortion. In all of these cases, the distortions lead to increased MSL and reduced signal detection capability.

Many of the simulations shown in this chapter present results that are not currently found in RMMSE literature. The results suggest that the distortions presented can have a significant impact on algorithm performance. In the severe degradation cases, the RMMSE output approaches matched filter performance. This could potentially preclude the use of the RMMSE algorithm in many systems. A robustness enhancement technique capable of returning distorted algorithm performance to the baseline level is investigated next.

Chapter 4: Enhancing RMMSE Performance Using Covariance Matrix Tapers

This chapter develops Covariance Matrix Tapers (CMTs) as a robustness enhancement technique for the RMMSE algorithm. CMTs are derived to address the problems of intrasample arrival, Doppler shift, and uncalibrated transducers. This approach is believed to be a new contribution to RMMSE processing.

4.1 Overview of Covariance Matrix Tapers

The term “Covariance Matrix Taper” corresponds to an amplitude taper applied directly to a covariance matrix through the use of the Hadamard product. The concept of CMTs was first introduced independently by Mailloux [34] and Zatman [35] in 1995. Since then, there have been numerous publications related to the topic. CMTs are primarily used in adaptive beamforming for Radar systems as a robustness enhancement against moving interferers. This application is derived in the Appendix. The work of Guerci [36] provides a mathematical description of CMTs and generalizes several of the original CMT approaches. This section briefly summarizes some of Guerci’s work. For a more complete treatment of the topic, see the cited reference.

4.1.1 Covariance Matrix Taper Framework

This section provides a brief background of CMTs. The matrices and vectors in this section are denoted with a subscript “g” to indicate that they are generic quantities not associated with any specific algorithm.

The covariance matrix, \mathbf{C}_{g1} associated with a signal model, \mathbf{s}_{g1} is defined:

$$\mathbf{C}_{g1} = E \{ \mathbf{s}_{g1} \mathbf{s}_{g1}^H \} = \text{COV} (\mathbf{s}_{g1}) \quad (4.1)$$

where COV denotes covariance and the signal is assumed to be 0 mean. In many practical applications, the true signal covariance matrix is not known and must be estimated. In certain cases, \mathbf{C}_{g1} may not be an accurate representation of the underlying random process. This can occur when the signal model does not match the true signal and is referred to as “model mismatch”. If mismatch is anticipated, actions can be taken in algorithm design to mitigate its effects. For example, diagonal loading of the covariance matrix is often employed in adaptive beamforming algorithms to make them robust against signal angle of arrival mismatch [37]. CMTs address a class of problems in which the mismatch can be modeled in the following form:

$$\mathbf{s}_{g2} = \mathbf{s}_{g1} \circ \mathbf{s}_{g\Delta} \quad (4.2)$$

Where (\circ) represents the Hadamard product. In this equation, the original, undistorted generic signal model is denoted as \mathbf{s}_{g1} . In the RMMSE algorithm, this would correspond to the waveform replica vector, \mathbf{s}_1 . The distorted, received signal is denoted as \mathbf{s}_{g2} .

The covariance matrix associated with \mathbf{s}_{g2} , $\mathbf{C}_{g2} = \text{COV} (\mathbf{s}_{g2})$ is:

$$\begin{aligned} \mathbf{C}_{g2} &= \text{COV} (\mathbf{s}_{g2}) \\ &= \text{COV} (\mathbf{s}_{g1} \circ \mathbf{s}_{g\Delta}) \end{aligned} \quad (4.3)$$

Assuming that \mathbf{s}_{g1} and $\mathbf{s}_{g\Delta}$ are uncorrelated, the element of \mathbf{C}_{g2} at row index m and

column index n is given by:

$$\begin{aligned}
C_{g2,mn} &= E \left\{ s_{g1m} s_{g\Delta m} s_{g1n}^* s_{g\Delta n}^* \right\} \\
&= E \left\{ s_{g1m} s_{g1n}^* s_{g\Delta m} s_{g\Delta n}^* \right\} \\
&= E \left\{ s_{g1m} s_{g1n}^* \right\} E \left\{ s_{g\Delta m} s_{g\Delta n}^* \right\}
\end{aligned} \tag{4.4}$$

Combining the results of (4.3) and (4.4) the covariance associated with \mathbf{s}_{g2} can be written:

$$\mathbf{C}_{g2} = \mathbf{C}_{g1} \circ \mathbf{C}_{g\Delta} \tag{4.5}$$

where $\mathbf{C}_{g1} = E \left\{ \mathbf{s}_{g1} \mathbf{s}_{g1}^H \right\}$ and $\mathbf{C}_{g\Delta} = E \left\{ \mathbf{s}_{g\Delta} \mathbf{s}_{g\Delta}^H \right\}$.

Therefore, in cases such as (4.2) where the distortion and signal model are related through the Hadamard product, the covariance matrices are also related through the Hadamard product as shown in (4.5). It is assumed that \mathbf{s}_{g1} and $\mathbf{s}_{g\Delta}$ are independent. This result allows a corrected covariance estimate to be generated when \mathbf{s}_{g1} is distorted by a random process.

4.2 CMT Use in RMMSE Processing

CMTs are currently used almost exclusively in adaptive beamforming applications to provide robustness against moving interferers. A CMT has also been developed for Space Time Adaptive Processing (STAP) applications [36]. This section investigates the use of CMTs in the RMMSE algorithm for the following sources of mismatch:

- Intrsample arrival
- Doppler
- Uncalibrated transducers

The application of CMTs as a robustness enhancement to the RMMSE algorithm is not currently found in the literature and is believed to be a new contribution to RMMSE processing.

In this section, it is assumed that the waveform is a linear frequency modulated (LFM) pulse. CMTs can be derived for other waveforms using the same general procedure. The covariance matrix, \mathbf{C}_1 as defined by (2.34) is the signal covariance matrix associated with the undistorted replica vector, \mathbf{s}_1 .

4.2.1 CMT Application to RMMSE for LFM Intrsample Arrival: Time Shift View

A basebanded LFM waveform at time t is given by:

$$s(t) = \begin{cases} e^{j2\pi(-\frac{\beta}{2}t + \frac{\beta}{2T}t^2)} & 0 \leq t < T \\ 0 & \text{otherwise} \end{cases} \quad (4.6)$$

Where β is the pulse bandwidth in Hz, and T is the pulse duration in seconds. To generate a N element discrete replica vector of the transmitted waveform, $s(t)$ is sampled at a rate of f_s Hz. The time instants at which $s(t)$ is sampled are given by the time vector

$$\mathbf{t} = [0, \quad 1/f_s, \quad 2/f_s, \quad \dots \quad (N-1)/f_s]^T \quad (4.7)$$

There are several equivalent methods to model intrasample arrival as a time shift. For notational simplicity, the A/D sample times remain as defined in (4.7), and the time argument in (4.6) is shifted by Δ_t seconds:

$$s(t + \Delta_t) = \begin{cases} e^{j2\pi(-\frac{\beta}{2}(t+\Delta_t) + \frac{\beta}{2T}(t+\Delta_t)^2)} & \Delta_t \leq t < T + \Delta_t \\ 0 & \text{otherwise} \end{cases} \quad (4.8)$$

This represents a received waveform in which the rising edge occurs at an offset from $t = 0$. The time offset, Δ_t , is an unknown random quantity. In subsequent equations regarding $s(t + \Delta_t)$, the pulse time interval will be omitted for simplicity. Defining $f_1 = -\frac{\beta}{2}$ and $\lambda = \frac{\beta}{2T}$, the above equation becomes:

$$s(t + \Delta_t) = e^{j2\pi(f_1(t+\Delta_t)+\lambda(t+\Delta_t)^2)} \quad (4.9)$$

Expanding the terms:

$$\begin{aligned} s(t + \Delta_t) &= e^{j2\pi(f_1 t + f_1 \Delta_t + \lambda t^2 + 2\lambda \Delta_t t + \lambda \Delta_t^2)} \\ &= \left(e^{j2\pi(f_1 t + \lambda t^2)} \right) \cdot \left(e^{j2\pi 2\lambda t \Delta_t} \right) \cdot \left(e^{j2\pi f_1 \Delta_t} \right) \cdot \left(e^{j2\pi \lambda \Delta_t^2} \right) \end{aligned} \quad (4.10)$$

Where (\cdot) denotes scalar multiplication. The first exponential term grouped above is the original LFM equation as in (4.6). Note that only the first two exponential terms have a dependence on t . Equation (4.10) is sampled at the discrete time samples defined in (4.7). The resulting N element vector is denoted as \mathbf{s}_2 . The n^{th} element of \mathbf{s}_2 is given by:

$$s_{2n} = \left(e^{j2\pi(f_1 n/fs + \lambda(n/fs)^2)} \right) \cdot \left(e^{j2\pi \Delta_t 2\lambda n/fs} \right) \cdot \left(e^{j2\pi f_1 \Delta_t} \right) \cdot \left(e^{j2\pi \lambda \Delta_t^2} \right) \quad (4.11)$$

This result is shown in matrix-vector form as

$$\mathbf{s}_2 = \mathbf{s}_1 \circ \mathbf{s}_\Delta \circ \mathbf{s}_a \circ \mathbf{s}_b \quad (4.12)$$

where \mathbf{s}_1 corresponds to the first exponential term in (4.11), \mathbf{s}_Δ corresponds to the second term, and so on. The subscript a and b above are used as dummy variables corresponding to the last two terms in (4.11). Since these terms have no dependence on time, the computation of their respective covariances will result in matrices comprised solely of 1's. These terms

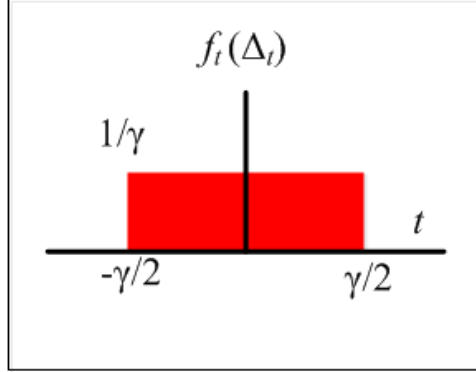


Figure 4.1: Probability Density Function for a zero mean uniform time distribution

therefore do not contribute to the result and will be omitted in subsequent calculations. From the results that lead to (4.5), the covariance matrix associated with \mathbf{s}_2 is the Hadamard product of the individual covariance matrices associated with each of the individual vectors in (4.12):

$$\mathbf{C}_2 = \mathbf{C}_1 \circ \mathbf{C}_\Delta \quad (4.13)$$

The matrix \mathbf{C}_1 is the covariance matrix associated with the undistorted signal model, and is therefore the RMMSE signal covariance matrix as defined in Chapter 2. The computation of \mathbf{C}_Δ is now considered.

The elements of \mathbf{C}_Δ are denoted as $C_{\Delta mn}$, where m and n correspond to the matrix row and column indices, respectively.

$$\begin{aligned} C_{\Delta mn} &= E \left\{ e^{j2\pi\Delta_t 2\lambda m/fs} e^{-j2\pi\Delta_t 2\lambda n/fs} \right\} \\ &= E \left\{ e^{j2\pi\Delta_t 2\lambda(m-n)/fs} \right\} \end{aligned} \quad (4.14)$$

It is assumed that the random process describing Δ_t is a uniformly distributed random variable defined on the interval $[-\gamma/2, \gamma/2]$ as shown in Figure 4.1. The expectation is evaluated via integration:

$$\begin{aligned}
C_{\Delta mn} &= \int_{-\gamma/2}^{\gamma/2} f_t(\Delta_t) e^{j2\pi\Delta_t 2\lambda(m-n)/fs} d\Delta_t \\
&= \int_{-\gamma/2}^{\gamma/2} \frac{1}{\gamma} e^{j2\pi\Delta_t 2\lambda(m-n)/fs} d\Delta_t
\end{aligned} \tag{4.15}$$

Using Euler's relation, this becomes

$$C_{\Delta mn} = \int_{-\gamma/2}^{\gamma/2} \frac{1}{\gamma} (\cos(2\pi\Delta_t 2\lambda(m-n)/fs) + j \sin(2\pi\Delta_t 2\lambda(m-n)/fs)) d\Delta_t \tag{4.16}$$

The sine term goes to 0 due to the symmetric limits of integration, leaving

$$C_{\Delta mn} = \int_{-\gamma/2}^{\gamma/2} \frac{1}{\gamma} \cos(2\pi\Delta_t 2\lambda(m-n)/fs) d\Delta_t \tag{4.17}$$

Solving the integral and rearranging terms yields:

$$C_{\Delta mn} = \text{sinc}\left(\frac{2\gamma\pi\beta(m-n)}{2Tf_s}\right) \tag{4.18}$$

In order for the probability density function to fully cover the region between A/D samples, γ is set to $1/fs$. This is equivalent to stating that the pulse is equally likely to arrive at any instant of time, regardless of where A/D samples fall. This results in a CMT whose m^{th} , n^{th} elements are given by:

$$C_{\Delta mn} = \text{sinc}\left(\frac{2\pi\beta(m-n)}{2Tf_s^2}\right) \tag{4.19}$$

The augmenting matrix, \mathbf{C}_Δ is a series of index-shifted sinc functions. The new covariance matrix for robustness against intrasample arrival, \mathbf{C}_2 is given by:

$$\mathbf{C}_2 = \mathbf{C}_1 \circ \mathbf{C}_\Delta \quad (4.20)$$

where the elements of \mathbf{C}_Δ are given by (4.19). The CMT obtained in this section is similar to the form found in adaptive beamforming CMTs. The similarity is due to the signals being modeled as complex exponentials and the distortions being modeled as uniform random variables.

4.2.2 CMT Application to RMMSE for LFM Intrasample Arrival: Instantaneous Frequency View

An alternative view of CMT application to the RMMSE algorithm for LFM is investigated. This approach is based analyzing the instantaneous frequency of the received waveform, as opposed to the time shift. The end result is the same as found in (4.19), but the derivation is simpler. The different approach also provides a means for understanding how CMTs help RMMSE performance in the presence of small Doppler distortions.

The frequency effects of intrasample arrival on an LFM pulse are illustrated in Figure 4.2. This figure shows the instantaneous analog frequency of the waveforms versus time. An A/D sample is taken at the times indicated by the black circles. The replica waveform is indicated by the blue line, and the received waveform is indicated by the red line. In practical cases, there is no guarantee that a received waveform will be sampled at the same analog frequencies as the replica waveform, as illustrated by this figure. This amounts to a mismatch between the replica and the received data in terms of instantaneous frequency. At any A/D sample, the received data is mismatched from the replica by a frequency offset. This is shown in the figure as the quantity Δ_f . The frequency offset is random for any given received pulse, but is constant over a received pulse due to the linear nature of the frequency sweep.

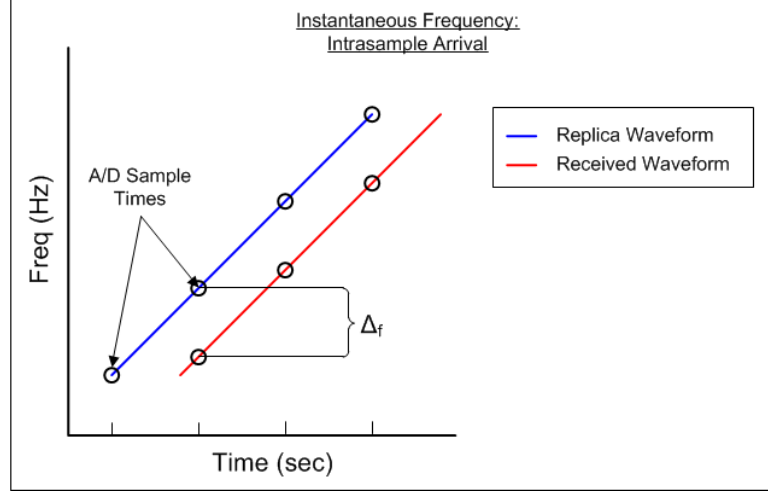


Figure 4.2: Effects of Intrasample Arrival on LFM Pulse

The frequency shift between the received data and the replica waveform is modeled using the shifting property of the Fourier transform. In order to frequency shift every sample of the replica by Δ_f Hz, a vector of complex exponentials is used. This $N \times 1$ vector is denoted as \mathbf{s}_Δ and its terms are given by:

$$\mathbf{s}_\Delta = \begin{bmatrix} e^{j2\pi\Delta_f 0/f_s} \\ e^{j2\pi\Delta_f 1/f_s} \\ \vdots \\ e^{j2\pi\Delta_f (N-1)/f_s} \end{bmatrix} \quad (4.21)$$

where f_s is the A/D sample rate, in Hz. Alternately stated, the n^{th} element of \mathbf{s}_Δ is given by $s_{\Delta n} = e^{j2\pi\Delta_f n/f_s}$ for $n = 0, 1, \dots, (N-1)$. The frequency shifted LFM, \mathbf{s}_2 , is written as:

$$\mathbf{s}_2 = \mathbf{s}_1 \circ \mathbf{s}_\Delta \quad (4.22)$$

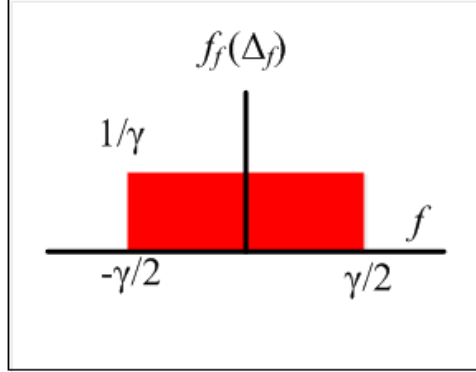


Figure 4.3: Probability Density Function for a zero mean uniform frequency distribution

Note that intrasample arrival causes the “loss” of a discrete sample. This can be seen easily in Figure 4.2. In that illustration, the replica is shown with 4 A/D samples, while only 3 samples of the received analog waveform are captured. It is assumed that the waveform replica is sufficiently long that the effects caused by a single sample loss are negligible.

The random process Δ_f is assumed to be uniformly distributed random variable on the interval $[-\gamma/2 \ \gamma/2]$ Hz. The probability density function of the random variable, $f_f(\Delta_f)$ is pictured in Figure 4.3.

Computation of the covariance matrix elements for \mathbf{s}_Δ is nearly identical to the derivation of $C_{\Delta mn}$ from the previous section. As before, the elements of the taper matrix are denoted as $C_{\Delta mn}$, where m and n correspond to the matrix row and column indices, respectively.

$$\begin{aligned}
 C_{\Delta nm} &= E \left\{ e^{j2\pi\Delta_f m/f_s} e^{-j2\pi\Delta_f n/f_s} \right\} \\
 &= E \left\{ e^{j2\pi\Delta_f (m-n)/f_s} \right\}
 \end{aligned} \tag{4.23}$$

The expectation is once again evaluated via integration:

$$\begin{aligned}
C_{\Delta mn} &= \int_{-\gamma/2}^{\gamma/2} f_f(\Delta_f) e^{j2\pi\Delta_f(m-n)/f_s} d\Delta_f \\
&= \int_{-\gamma/2}^{\gamma/2} \frac{1}{\gamma} e^{j2\pi\Delta_f(m-n)/f_s} d\Delta_f
\end{aligned} \tag{4.24}$$

Using Euler's relation,

$$C_{\Delta mn} = \int_{-\gamma/2}^{\gamma/2} \frac{1}{\gamma} (\cos(2\pi\Delta_f(n-m)/f_s) + j \sin(2\pi\Delta_f(n-m)/f_s)) d\Delta_f \tag{4.25}$$

The sine term goes to 0 due to the symmetric limits of integration, leaving

$$C_{\Delta mn} = \int_{-\gamma/2}^{\gamma/2} \frac{1}{\gamma} \cos(2\pi\Delta_f(n-m)/f_s) d\Delta_f \tag{4.26}$$

Solving the integral and rearranging terms yields:

$$C_{\Delta mn} = \text{sinc}\left(\frac{\gamma}{2} 2\pi(m-n)/f_s\right) \tag{4.27}$$

As before, \mathbf{C}_2 is given by:

$$\mathbf{C}_2 = \mathbf{C}_1 \circ \mathbf{C}_\Delta \tag{4.28}$$

In order to accomodate the possible range of frequency offsets, $\gamma/2$ must be large enough

to account for half of the frequency difference between adjacent A/D samples of the waveform. The offset between samples is constant for an LFM and is determined by the bandwidth and pulse duration. If the waveform bandwidth is given by β and the pulse duration is given by T , then γ must be set such that

$$\gamma = \frac{\beta}{Tf_s} \quad (4.29)$$

This results in a CMT whose m^{th} , n^{th} element is given by:

$$C_{\Delta mn} = \text{sinc} \left(\frac{2\pi\beta(m-n)}{2Tf_s^2} \right) \quad (4.30)$$

which is the same result as (4.19)

4.2.3 CMT Application to RMMSE for Small Doppler Shifts

As stated previously, the Doppler effect causes three primary distortions in pulsed waveforms:

- Pulse duration scaled by $\frac{1}{\alpha}$
- Bandwidth scaled by α
- Center frequency scaled by α

The α term was defined earlier to be the Doppler factor. For small Dopplers (i.e., $\alpha \approx 1$), the Doppler effect may be approximated by a fixed frequency shift of each sample. Figure 4.4 illustrates a sample case. The blue line represents the original (undistorted) waveform replica. The red line represents the received data after Doppler distortion. A relatively small Doppler effect has been illustrated in this example. The frequency offset between the blue and red lines is approximately the same over the pulse duration.

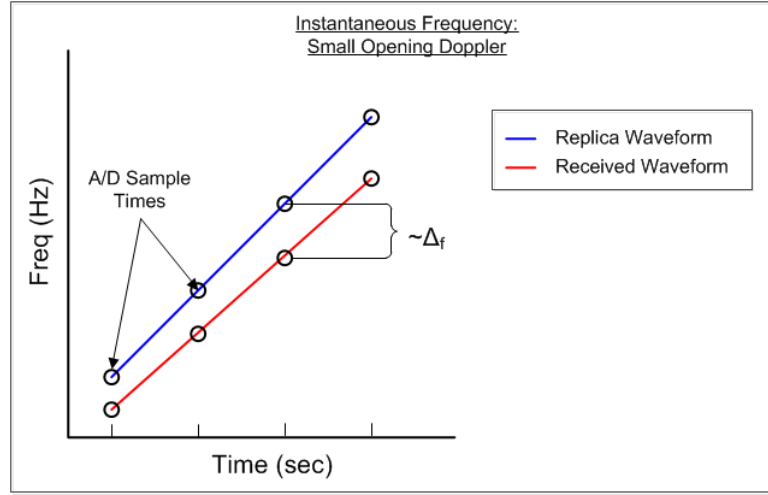


Figure 4.4: Effects of Doppler on LFM pulse for a low opening Doppler

In this case, the distortion caused by Doppler is approximately the same as the effects of intrasample arrival. Each sample of the waveform is subject to a frequency shift that is approximately equal for all samples. The CMT result obtained in (4.27) may therefore also be used to mitigate relatively small Doppler distortions. As the Doppler effect becomes more severe, the slope of the received waveform changes significantly, and this approximation is no longer valid. The extent to which this approximation is valid depends on several independent factors. These factors include, but are not limited to:

- Total Doppler
- Pulse duration
- Pulse bandwidth
- Speed of wave propagation in medium
- A/D sample rate

If the CMT approach is to be used to provide robustness against Doppler using the RMMSE algorithm, its benefits need to be analyzed on a case-by-case basis. It is possible that there

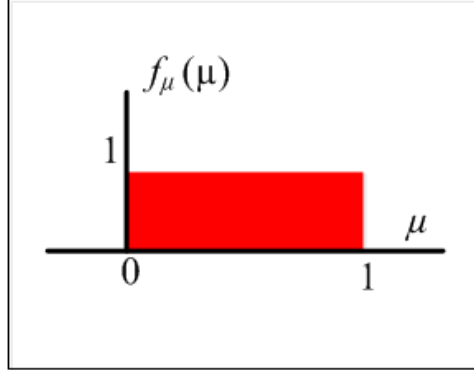


Figure 4.5: Probability density function for μ as a uniform distribution on the interval $(0,1]$

are other techniques that can provide the RMMSE algorithm with enhanced robustness against Doppler. This is an area of future work.

4.2.4 CMT Application to RMMSE for Uncalibrated Transducers

The undistorted transducer was introduced in Chapter 3 as an ideal bandpass filter with start and stop edges corresponding to the starting and stopping frequencies of the LFM sweep as shown in Figure 3.13(a). The uncalibrated transducer is modeled as a bandpass filter with non-uniform passband. The passband has a gain of μ at f_{start} , and increases to unity gain by f_{stop} , where $\mu \leq 1$, as shown in Figure 3.13(b). It is assumed that the value of μ is not known, but can be statistically modeled. For this simulation, μ is a random variable uniformly distributed between 0 and 1. The distribution for this random variable is shown in Figure 4.5. The mean of this distribution is 0.5.

If the LFM upswing previously is again used as the transmitted waveform, then the distorted waveform, \mathbf{s}_2 may be modeled as the Hadamard product of the original waveform replica vector, \mathbf{s}_1 with a linear ramp, \mathbf{s}_r :

$$\mathbf{s}_2 = \mathbf{s}_1 \circ \mathbf{s}_r \quad (4.31)$$

Where the elements of \mathbf{s}_r are given as:

$$\mathbf{s}_r = \begin{bmatrix} \frac{1-\mu}{N-1}0 + \mu \\ \frac{1-\mu}{N-1}1 + \mu \\ \vdots \\ \frac{1-\mu}{N-1}(N-1) + \mu \end{bmatrix} \quad (4.32)$$

The element in the m^{th} row and n^{th} column of the covariance matrix \mathbf{C}_r associated with \mathbf{s}_r is given by:

$$C_{r,mn} = E \left\{ \left(\frac{1-\mu}{N-1}m + \mu - 0.5 \right) \left(\frac{1-\mu}{N-1}n + \mu - 0.5 \right) \right\} \quad (4.33)$$

where the 0.5 term is the mean of the random process. The expectation is now evaluated using the uniform distribution on the interval from 0 to 1:

$$\begin{aligned} C_{r,mn} &= \int_0^1 \left(\frac{1-\mu}{N-1}m + \mu - 0.5 \right) \left(\frac{1-\mu}{N-1}n + \mu - 0.5 \right) d\mu \\ &= \frac{n(m-0.25(N-1))-0.25(N-1)(m-N+1)}{3(N-1)^2} \end{aligned} \quad (4.34)$$

The covariance matrix \mathbf{C}_r with elements are defined by (4.34) may be used to mitigate the modeled transducer distortion. The augmented covariance matrix, \mathbf{C}_2 is obtained by the use of the Hadamard product:

$$\mathbf{C}_2 = \mathbf{C}_1 \circ \mathbf{C}_r \quad (4.35)$$

4.3 Summary

This chapter proposes that CMTs may be used to make the RMMSE algorithm robust against several types of distortion. This approach is not currently found in literature and

is therefore believed to be a new contribution to the field. A CMT was developed for intrasample arrival distortion and was shown to have potential use against small Doppler shifts. A CMT was also developed for the given transducer distortion model.

Chapter 5: Results of Applying Covariance Matrix Tapers to RMMSE Processing

The previous chapter developed two CMTs as a means of augmenting the RMMSE covariance matrix defined in Chapter 2. These CMTs were developed using prior knowledge of the forms of distortion that are likely to occur. In this chapter, the effects of using the derived CMTs in RMMSE processing are investigated.

5.1 Simulation Setup and CMT Selection

The basic simulation for this chapter is the same simulation used in Chapter 3. Unless otherwise stated, there are two signals present in the data. The primary signal is 55 dB above the nominal nominal noise floor and is located at lag=0 seconds. The secondary signal is 10 dB above the noise floor and is located at lag=-0.10 seconds. The waveform selected is a 0.20 second, 200 Hz bandwidth linear frequency modulated (LFM) waveform. As before, three forms of distortion are investigated:

- Intrsample arrival
- Doppler
- Uncalibrated transducer(s)

The original signal covariance matrix for the RMMSE algorithm derived in Chapter 2 is denoted as \mathbf{C}_1 . The augmented covariance matrix obtained from applying the CMT(s) to \mathbf{C}_1 via Hadamard product is denoted as \mathbf{C}_2 . The CMT used to mitigate intrasample arrival and small Doppler shifts is denoted as \mathbf{C}_Δ , and the CMT used to mitigate the ramp-like transducer distortion is denoted as \mathbf{C}_r . Results obtained using \mathbf{C}_1 are denoted as RMMSE results, while results obtained using \mathbf{C}_2 are denoted as RMMSE-CMT results.

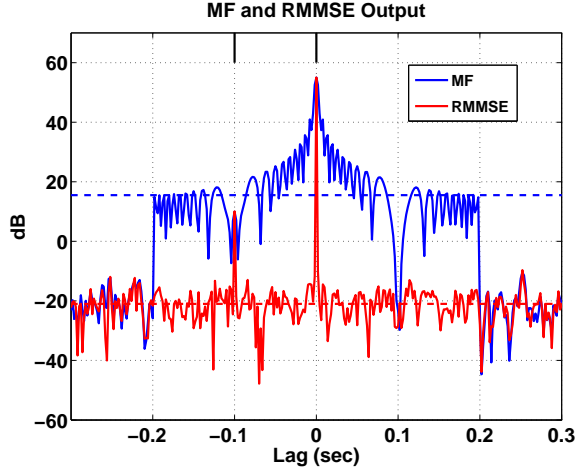


Figure 5.1: Baseline simulation: RMMSE (red) and matched filter (blue) outputs

5.2 Simulation Results

The distortions used in Chapter 3 were applied to the modeled signals. The RMMSE processing code was modified to use the augmented covariance matrix, \mathbf{C}_2 . In addition, a stressing scenario was developed to illustrate performance in the presence of multiple distortions. The results are presented below.

5.2.1 Baseline Case

The baseline results presented in Chapter 3 are briefly reviewed here for convenience. Figure 5.1 shows the matched filter and RMMSE processing results when no distortion is incorporated. Both the primary signal and the secondary signal are clearly visible in the RMMSE output. Their locations are indicated by the vertical black tick marks at the top of the plot. The RMMSE sidelobe level is approximately the same level as the noise floor. The noise floor appears at -20 dB in this figure due to the signal level calibration.

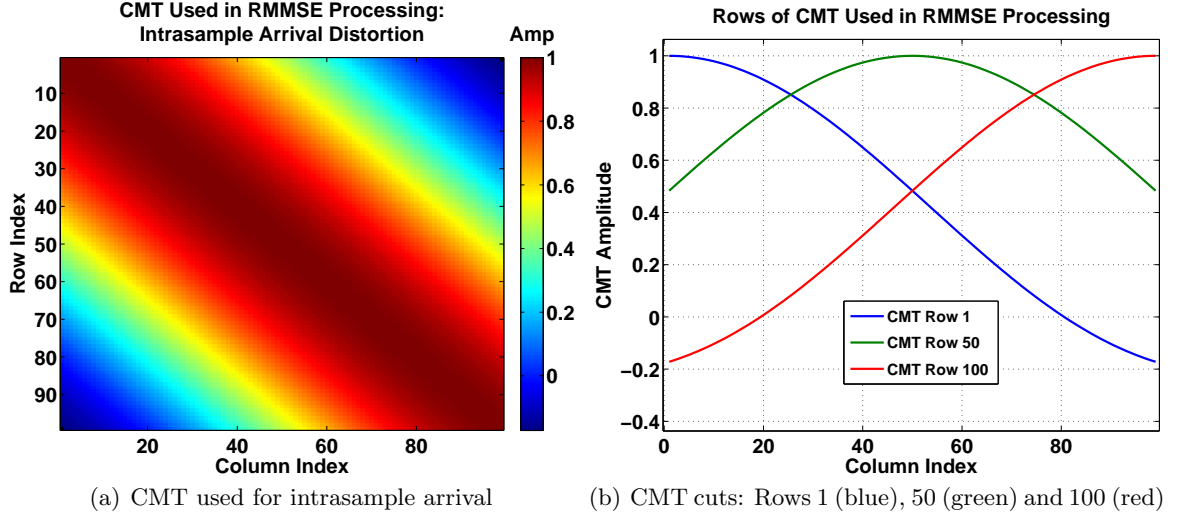


Figure 5.2: CMT to be applied to estimated covariance matrix

5.2.2 Intrasample Arrival

Background

The CMT used for intrasample arrival is built using equation (4.19). For this particular waveform, the CMT is a 100×100 matrix whose element in the m^{th} row and n^{th} column is given by:

$$C_{\Delta,mn} = \text{sinc}\left(\frac{2\pi\beta(m-n)}{2Tf_s^2}\right) \quad (5.1)$$

Substituting the waveform parameters from table 3.1 results in:

$$C_{\Delta,mn} \approx \text{sinc}(0.0126(m-n)) \quad (5.2)$$

The resulting CMT is shown in Figure 5.2(a). Selected rows of the CMT are shown in Figure 5.2(b). The augmented signal covariance matrix, \mathbf{C}_2 for use in RMMSE-CMT processing

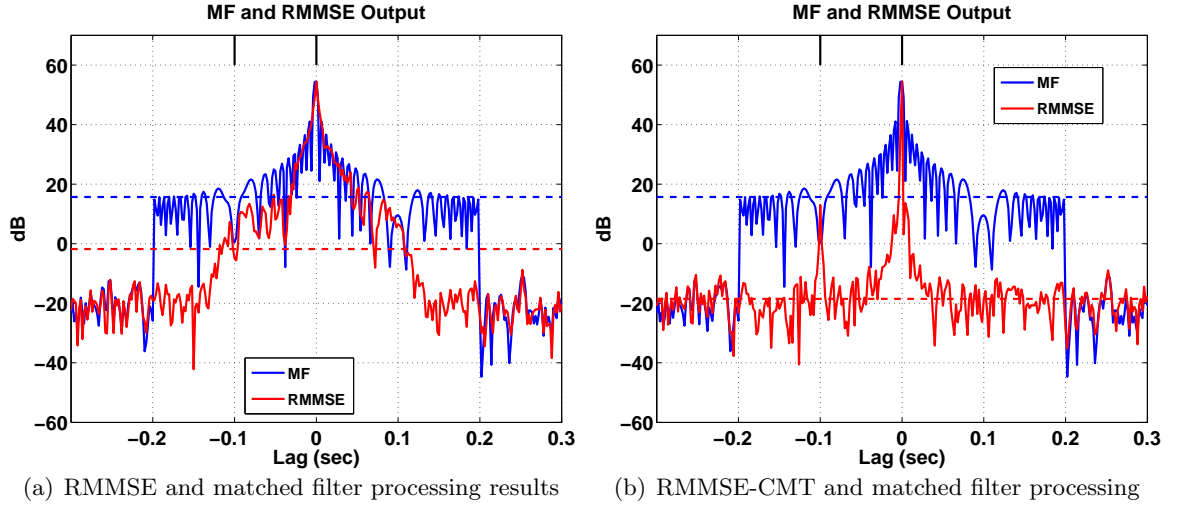


Figure 5.3: Intrasample arrival distortion: Results of RMMSE and RMMSE-CMT processing; Pulse arrives halfway between A/D samples

for this distortion is computed as:

$$\mathbf{C}_2 = \mathbf{C}_1 \circ \mathbf{C}_\Delta \quad (5.3)$$

Results

It was seen in Chapter 3 that intrasample arrival causes elevated sidelobes. A RMMSE output example is shown in Figure 5.3(a). In this case, the signal arrives halfway between A/D samples. The sidelobes are clearly elevated, and the secondary signal is not visually detectable. The RMMSE-CMT results are shown in Figure 5.3(b). The RMMSE-CMT approach has reduced sidelobe levels to near the baseline level.

The RMMSE and RMMSE-CMT MSL is shown in Figure 5.4 over the full range of intrasample arrival cases. As before, the normalized distance refers to the relative offset of the rising edge of the pulse from an A/D sample. A normalized distance of 0 indicates that the pulse arrives directly on an A/D sample, while a normalized distance of 0.5 indicates that the pulse arrives exactly halfway between A/D samples. The dashed red line shows

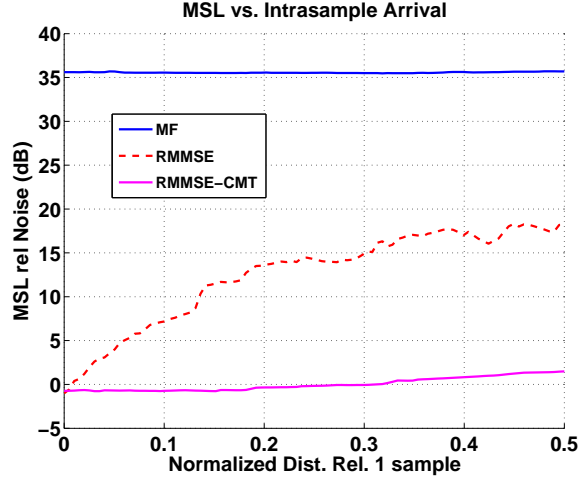


Figure 5.4: Intrasample arrival distortion: MSL for matched Filter, RMMSE and RMMSE-CMT

the RMMSE MSL and matches the results presented in Chapter 3. The magenta line is the RMMSE-CMT MSL. The RMMSE-CMT approach has effectively mitigated intrasample arrival distortion.

Summary

Intrasample arrival is a form of mismatch that is expected in most practical systems. The RMMSE algorithm is sensitive to this form of distortion. The RMMSE-CMT approach effectively mitigates this form of distortion and returns algorithm performance to the baseline level.

5.2.3 Doppler Distortion

Background

Chapter 3 showed that the RMMSE algorithm is sensitive to the distortions caused by the Doppler effect. A significant amount of benefit can be realized by first estimating the signal Doppler prior to running RMMSE. If the Doppler estimation is inexact, a Doppler error

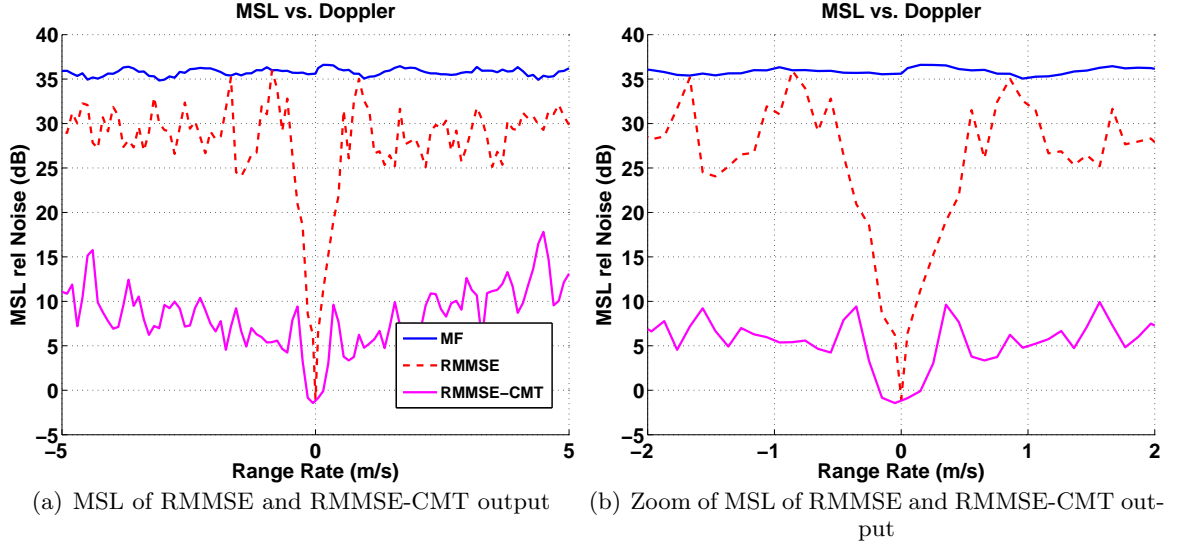


Figure 5.5: Doppler distortion: MSL of matched filter, RMMSE, RMMSE-CMT outputs.
Doppler estimation not performed

will be present. Assuming that the Doppler estimation error is relatively small, \mathbf{C}_Δ may be used to further improve performance in the presence of Doppler distortion.

Results

In order to determine the range of Doppler shifts over which the CMT enhances performance, the simulation was run without Doppler estimation being used. Figure 5.5 shows the MSL values obtained in this simulation.

The RMMSE-CMT approach improves MSL performance in several aspects. First, the notch near 0 m/s range rate has been widened compared the original RMMSE approach. This notch provides an indication of the region over which the RMMSE-CMT output is nearly identical to the baseline performance. Without CMT, the notch width is roughly ± 0.04 m/s. RMMSE-CMT increases the width to ± 0.30 m/s. Additionally, the overall MSL is lower for RMMSE-CMT. Without the CMT, the RMMSE is very high for many of the range rates investigated, though it is still generally below the matched filter MSL. In the RMMSE-CMT output, the MSL is, on average, 20 dB lower than the RMMSE levels.

In practical systems, achieving ± 0.30 m/s accuracy in Doppler estimation may not be a realistic goal. Inspection of the RMMSE-CMT outputs indicates algorithm performance is acceptable up to ± 1.5 m/s, even though these regions have elevated sidelobes compared to the baseline case. Figure 5.6 shows algorithm performance at ± 1.5 m/s. The RMMSE results are shown in Figures 5.6(a) and 5.6(c). In these plots, the RMMSE performance is distorted and it is not possible to see the secondary signal. The RMMSE-CMT results are shown in Figures 5.6(b) and 5.6(d). Though the sidelobes are higher than the baseline case, both signals are clearly visible. Performance is not perfect, but the degradation is acceptable.

The simulation was also processed using the Doppler ambiguity surface estimation technique discussed in Chapter 3. The MSL results are shown in Figure 5.7. The combination of Doppler estimation and the RMMSE-CMT approach provide robust performance in the presence of Doppler distortion.

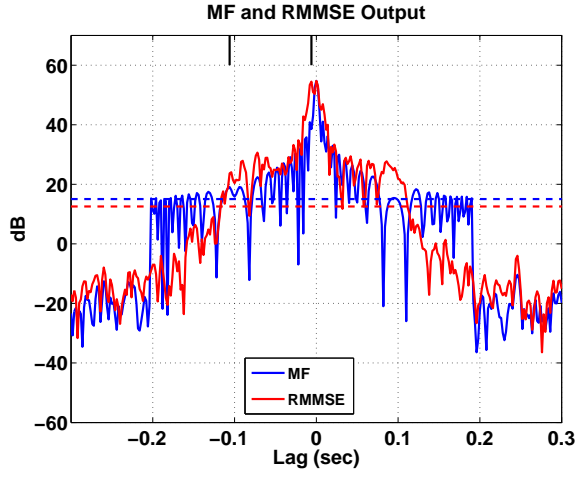
Summary

The RMMSE-CMT approach recovers performance in the presence of small Doppler distortions. For this simulation, RMMSE-CMT recovers near-baseline performance within ± 0.30 m/s, compared to ± 0.04 m/s without the CMT. Additionally, acceptable performance is noted up to ± 1.5 m/s with RMMSE-CMT. There is no acceptable performance outside of ± 0.04 m/s in the RMMSE case.

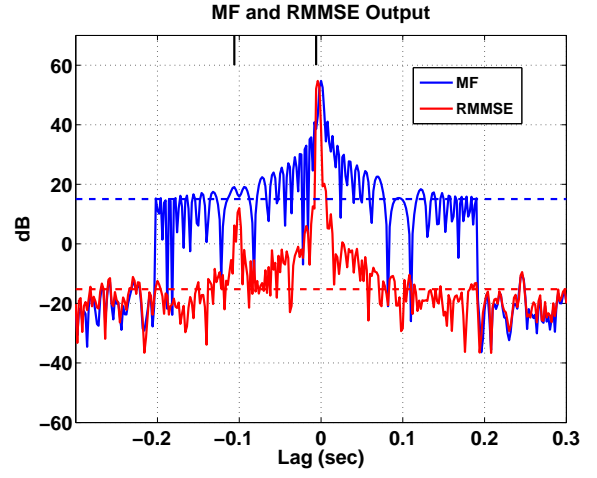
5.2.4 Uncalibrated Transducer Effects

Background

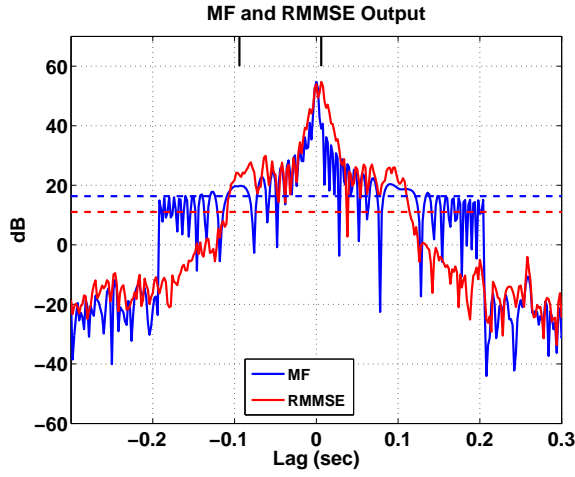
Chapter 3 showed that the RMMSE algorithm is sensitive to the effects of uncalibrated transducers. In Chapter 4, a CMT was developed for a simple transducer distortion model, and defined as \mathbf{C}_r in equation (4.34). Recall that this distortion is modeled as a bandpass filter with a linear gain ramp and is implemented as a time domain amplitude taper for an



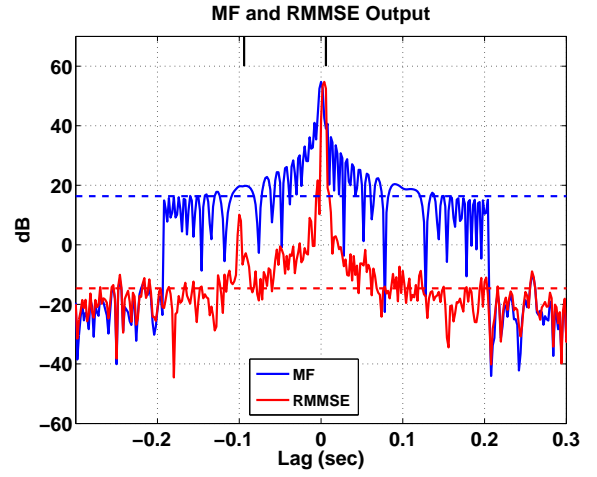
(a) RMMSE output: -1.5 m/s Doppler



(b) RMMSE-CMT output: -1.5 m/s Doppler



(c) RMMSE output: +1.5 m/s Doppler



(d) RMMSE-CMT output: +1.5 m/s Doppler

Figure 5.6: Doppler distortion: RMMSE and RMMSE-CMT output with ± 1.5 m/s Doppler

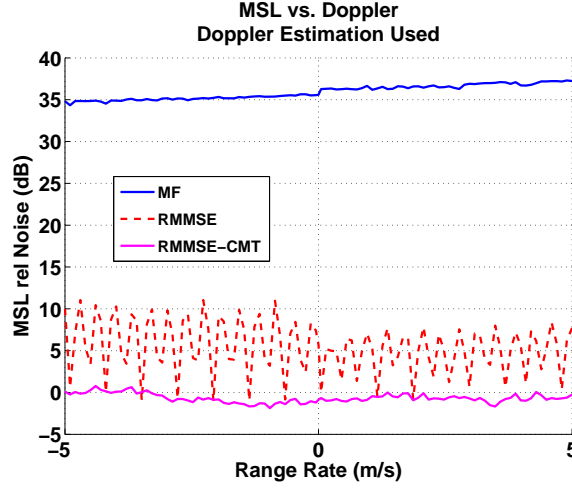


Figure 5.7: Doppler distortion with Doppler estimation: MSL for matched filter, RMMSE and RMMSE-CMT approaches

LFM. Figure 5.8 shows the 100×100 CMT for the waveform being investigated.

Results

This CMT was used in RMMSE processing for the same μ values that were set in Chapter 3: 100 linearly spaced increments from 0.01 to 1.0. In dB scale, this corresponds to -40 dB to 0 dB. Figure 5.9(a) shows the processing results when $\mu = 0.01$ and a CMT is not used. This value of μ corresponds to an initial attenuation of 40 dB, which is very severe. A significant performance degradation is seen in the RMMSE output. Figure 5.9(b) shows the results when the CMT defined by equation (4.34) is used. Though the RMMSE floor is slightly elevated compared to the baseline, both signals are clearly detectable. At this μ value of -40 dB, the initial sample is nearly zeroed. The linear nature of the shading ramp reduces the energy in the pulse by approximately one-half. The noise floor is therefore expected to be 6 dB higher than the baseline case due to the reduction in coherent gain.

The MSL for all values of μ are shown in Figure 5.10. The x -axis corresponds to the investigated μ values in dB and the y -axis corresponds to the MSL relative to the noise

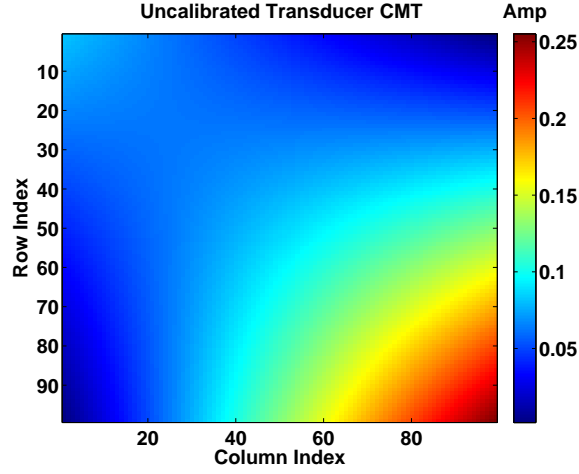


Figure 5.8: CMT for uncalibrated transducer distortion

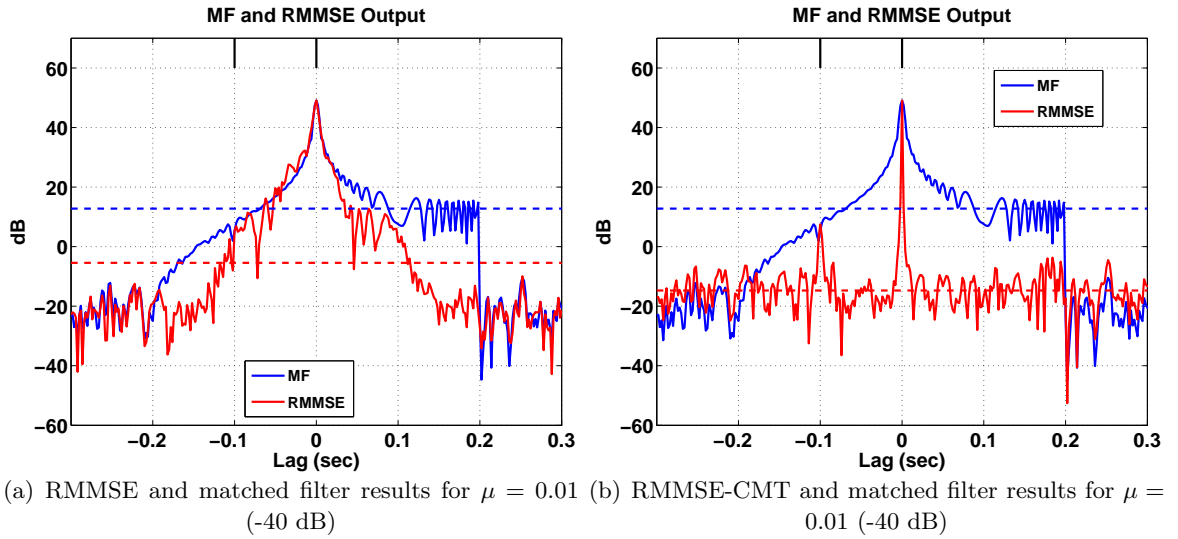


Figure 5.9: Uncalibrated transducer distortion: Results of matched filter, RMMSE and RMMSE-CMT processing, lowest frequency attenuated 40 dB

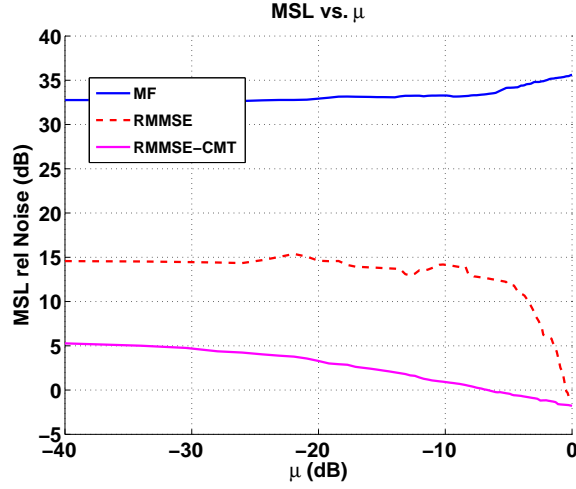


Figure 5.10: Uncalibrated transducer distortion: MSL of matched filter, RMMSE, and RMMSE-CMT outputs. Min taper value (μ) on x -axis, MSL rel. baseline noise floor on y -axis

floor. The matched filter results are shown in blue, and the RMMSE and RMMSE-CMT results are shown in red and magenta, respectively. The RMMSE-CMT approach improves performance and mitigates the effects of this distortion. As expected, the lowest μ values, which correspond to the highest attenuation, have higher MSL due to decreased coherent gain. Overall, this CMT has completely restored RMMSE performance, as demonstrated in Figure 5.9(b).

Summary

The CMT developed for this form of transducer distortion is very effective. RMMSE performance is restored, even in the most stressing case.

5.2.5 Stressing Scenario

Background

As a final test of CMT utility in RMMSE processing, a stressing scenario is developed. Up to this point, the simulations have consisted of two signals. Further, forms of distortion have been isolated. In a practical system, multiple forms of distortion can be expected on received data. The presence of Doppler distortion does not preclude a signal from arriving between A/D samples. The stressing scenario consists of 10 signals, all of which are subjected to intrasample arrival, Doppler distortion, and uncalibrated transducer effects.

Four of the signals are considered strong signals and are visible in the matched filter output. The remaining six signals are weaker and are below the matched filter sidelobes. Table 5.1 summarizes the distortions for all of these signals. The column denoted “A/D Dist. (nrm)” refers to the normalized distance between A/D samples of the pulse rising edge. These values were selected randomly from a uniform distribution between 0 and 0.5. The Doppler factor used in RMMSE processing corresponds to a range rate of 1.43 m/s. The true signal range rates are listed in the column titled “Rng. Rate (m/s)”. These values were randomly selected from a Gaussian distribution with mean 1.5 m/s and standard deviation of 0.0001 m/s. The transducer transfer function minimum, μ is set to the same value for all signals (-6 dB).

Results

The simulation was processed by the matched filter, RMMSE and RMMSE-CMT algorithms. For the RMMSE-CMT algorithm, it is assumed that it is known that intrasample arrival can occur, so \mathbf{C}_Δ will be used. Furthermore, it is assumed that it is known that there is some form of transducer distortion present. The value of μ for this particular transducer is not known, but a statistical description is known and matches the assumptions outlined in Chapter 4. Therefore, \mathbf{C}_r is used to mitigate the transducer distortion. The final CMT used in processing, \mathbf{C}_2 is obtained as:

Table 5.1: Stressing scenario signal settings

ID	Lag (sec)	Power (dB)	A/D Dist. (nrm)	Rng. Rate (m/s)	μ (dB)
1	-0.174	15	0.216	1.52	-6
2	-0.148	45	0.202	1.53	-6
3	-0.128	15	0.153	1.51	-6
4	-0.100	15	0.102	1.53	-6
5	-0.060	20	0.469	1.39	-6
6	0.000	55	0.263	1.59	-6
7	0.066	50	0.070	1.61	-6
8	0.100	15	0.102	1.51	-6
9	0.126	15	0.255	1.61	-6
10	0.152	40	0.196	1.60	-6

$$\mathbf{C}_2 = \mathbf{C}_1 \circ \mathbf{C}_\Delta \circ \mathbf{C}_r \quad (5.4)$$

The results of processing this simulation through the RMMSE algorithm are shown in Figure 5.11(a). The RMMSE sidelobes are generally lower than the matched filter for this case, but overall signal detection capability is not significantly improved. The strong signals (ID: 2, 6, 7, 10) can be seen in both matched filter and RMMSE output. The result of RMMSE-CMT processing is shown in Figure 5.11(b). In this plot, all 10 signals are clearly visible and can be detected. Table 5.2 shows the local SNR measurements for the matched filter, RMMSE and RMMSE-CMT approaches. These measurements were made through visual inspection of Figures 5.11(a) and 5.11(b). Entries marked with a dash “-” indicate that the signal is not visually detectable in the algorithm output. The SNR measurements were made relative to the noise floor immediately surrounding the detected signals. The RMMSE-CMT approach clearly outperforms the other approaches in this simulation. All signals were visually detectable, and their local SNR measurements are close to the true values.

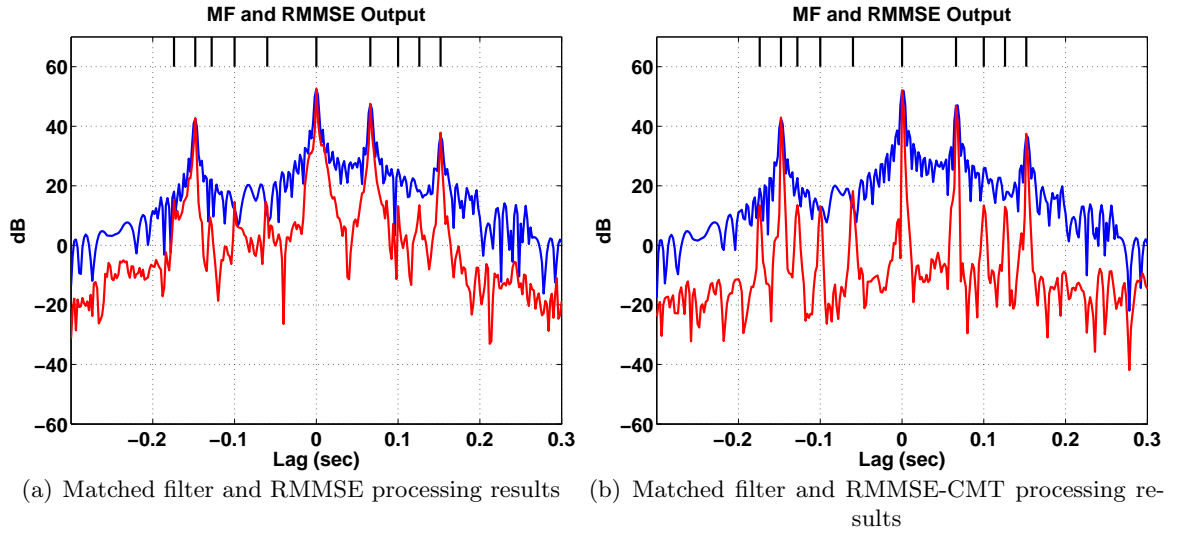


Figure 5.11: Stressing Scenario: Results of matched filter, RMMSE and RMMSE-CMT processing, true signal locations denoted by black vertical ticks

Table 5.2: Stressing scenario SNR results

ID	True SNR (dB)	MF SNR (dB)	RMMSE SNR (dB)	RMMSE-CMT SNR (dB)
1	35	-	-	33
2	65	30	49	62
3	35	-	-	28
4	35	-	15	33
5	40	-	10	37
6	75	38	50	68
7	70	17	47	61
8	35	-	-	29
9	35	-	-	29
10	60	17	38	56

Summary

The stressing scenario represents a more realistic case than the individual distortion cases investigated previously. Ten signals were subjected to multiple forms of distortion to create a complex return. Multiple CMTs were combined to counteract the varied distortions. The RMMSE-CMT approach provides superior performance over the RMMSE and Matched Filter.

5.3 Summary of CMT Use in RMMSE Processing

The distortions investigated in this chapter and in Chapter 3 are expected in most practical sonar systems. Intrasample arrival is virtually guaranteed, and Doppler-like distortion is common, even if the scenario is assumed stationary. Transducers with inaccurate calibrations can also occur. Even if the sensors themselves are calibrated, sound propagation channels have frequency dependent effects [4], leading to distortion resembling uncalibrated transducers.

The CMTs derived in Chapter 4 have been seen to provide significant performance enhancements in the presence of distortion. This, coupled with their relatively low computational cost indicate that CMTs are a very desirable complement to the RMMSE algorithm.

Chapter 6: Acoustic Data Analysis

In this chapter, algorithm performance is demonstrated on acoustic data. The test data under investigation is described. The RMMSE and RMMSE-CMT results are displayed and compared against the matched filter. It is seen that the RMMSE-CMT approach suppresses time sidelobes and enables the detection of weak signals.

6.1 Data Description and Processing Steps

Between 2009 and 2010, acoustic sensor data was collected in the Philippine Sea for the purpose of analyzing temperature and current changes. This research was sponsored by the Office of Naval Research (ONR) and is denoted as the PhilSea experiment. At the beginning of the experiment, acoustic sources and receivers were deployed at various locations throughout the operational area. In one such deployment, a transmit and receive module were attached to a vertical line as shown in Figure 6.1. The transmitter is at the bottom of the cable, at a depth of 1000 m. The receiver is in the center of the cable, at a depth of 500 m. The transmitter beam pattern is known to be approximately a dipole pattern, and is symmetric about the vertical axis.

Following deployment of the source and receiver, a test was performed to validate the transmitter was operating correctly. Several signals were transmitted and receiver data was collected and analyzed to verify system health. Due to the close proximity of the source and receiver, the signal level at the receiver is very high, and is therefore a good candidate for RMMSE investigation. This chapter analyzes the data collected to verify source operation.

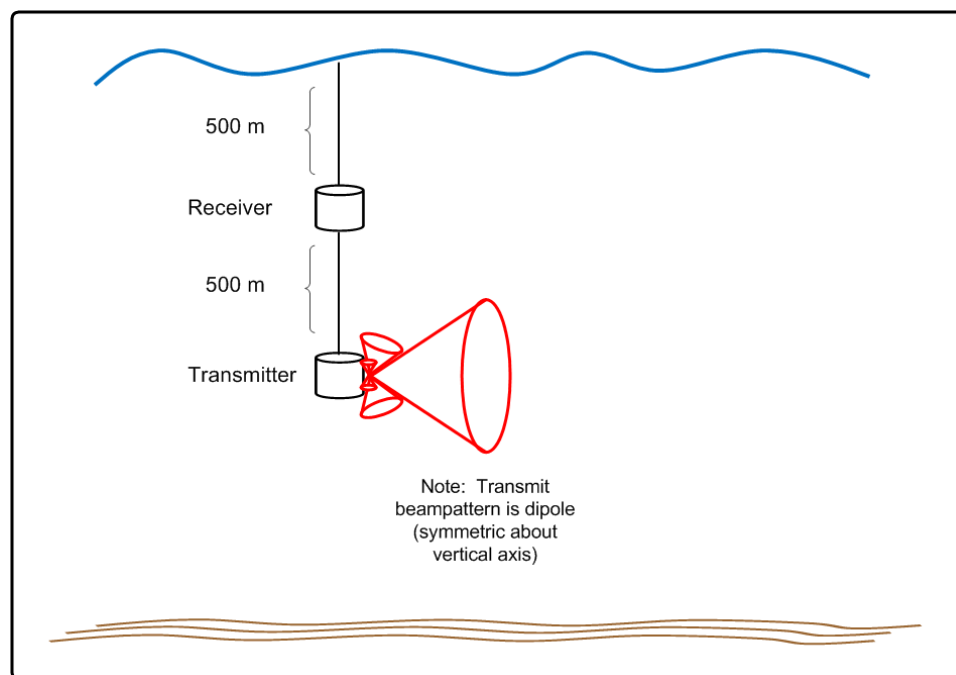


Figure 6.1: Transmitter and receiver configuration for acoustic data. Transmit beampattern is symmetric about vertical axis

Table 6.1: Acoustic Data LFM Parameters

	Value	Units	Symbol
Bandwidth	100	Hz	β
Duration	135	sec	T
Center frequency	275	Hz	f_c
Sample Rate	1953.125	Hz	f_s

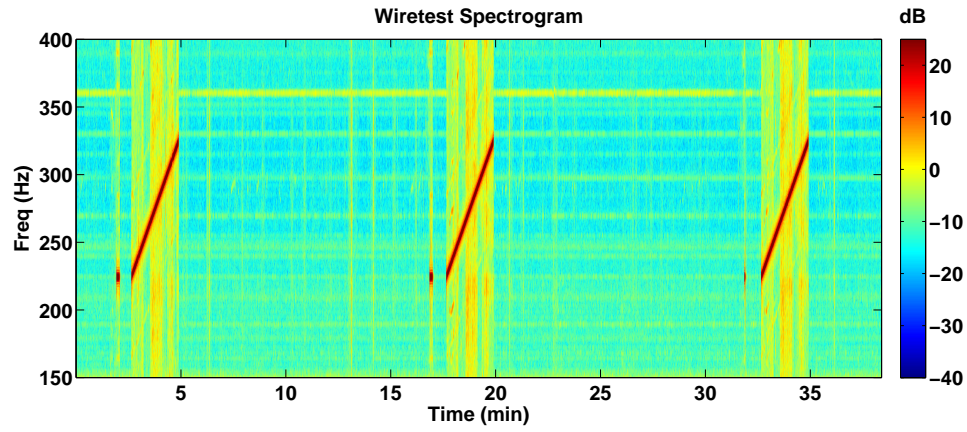


Figure 6.2: Spectrogram of acoustic data. Zoomed to show LFM region.

6.1.1 Input Data

The acoustic data comprises roughly 60 minutes collection time. There are three identical LFM transmissions in the data. The LFM parameters are summarized in Table 6.1.

A spectrogram of the input data is shown in Figure 6.2. This spectrogram has been zoomed to show the LFM waveforms, which are clearly visible as the dark red diagonal lines. Approximately 0.8 seconds prior to the LFM transmissions, a 0.2 second continuous wave (CW) pulse is transmitted at 225 Hz.

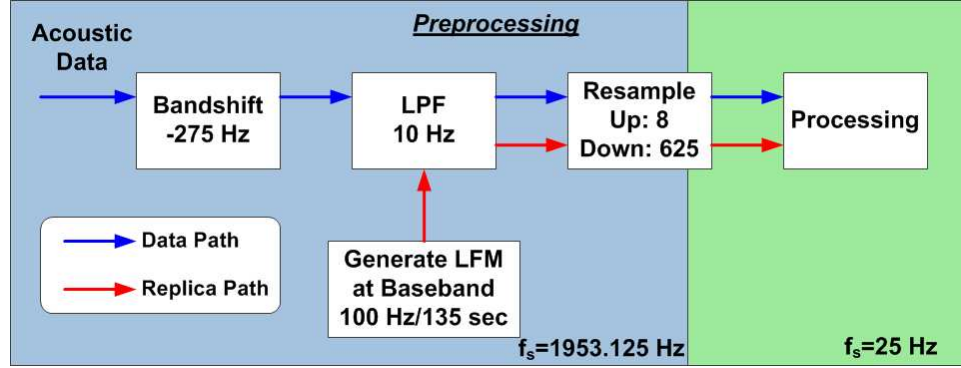


Figure 6.3: Acoustic data and replica preprocessing steps. Colored background regions highlight sample rate changes

6.1.2 Data Preprocessing

Given the waveform duration and sample rate, $N \approx 26367$ in the initial data. Inverting a matrix of this dimension presents a significant computational burden. The dimension must be reduced in order to process the data in a reasonable amount of time. On the computing resources available, it was empirically determined that the maximum matrix size capable of being processed in a timely manner is $N \approx 900$. It is also desired to have some amount of bandwidth to maintain the desirable correlation properties of the LFM. Given the relatively slow sweep rate of this waveform (approximately 0.74 Hz/sec), the replica must therefore be relatively long in duration. These conflicting requirements necessitate that the input data be preprocessed to decrease the bandwidth and sample rate. After multiple experiments and tradeoffs, it was decided to downsample to 25 Hz, yielding a replica approximately 34 seconds in duration. The preprocessing steps are illustrated in Figure 6.3 and described in subsequent paragraphs.

Bandshift

The first step in preprocessing the data is to baseband the LFM. A time domain complex exponential is used to shift the center frequency of the waveform from 275 to 0 Hz.

Replica Generation

Using a replica with bandwidth equal to the desired bandwidth of 25 Hz resulted in poor algorithm performance. It was determined through multiple experiments that the replica should be subjected to the same preprocessing steps as the data. This is likely due to the fact that the original signal contains information outside of the passband of the downsampled signal. Subjecting the replica to the same processing steps as the data results in a better match between the replica and the data. The replica was generated at baseband with waveform parameters as defined in Table 6.2 using (3.1)

Low Pass Filter

In order to prevent aliasing effects during the downsampling process, the acoustic data and replica are low pass filtered prior to resampling. Given the extremely low desired sample rate, a high order filter is necessary to suppress signal content outside of the desired band. A 2700 point Chebychev window with cutoff frequency of 10 Hz was generated using Matlab's "chebwin" function. The magnitude and phase of the selected filter are shown in Figure 6.4.

Resampling

Following the LPF, the data rate was reduced to 25 Hz. This was accomplished using Matlab's "resample" function. The data is first upsampled by a factor of 8, and then downsampled by a factor of 625 to achieve a final sample rate of 25 Hz.

6.1.3 Data Processing

The steps in the data processing segment are illustrated in Figure 6.5. Acoustic data is first time windowed to reduce the number of computations. The replica is also time-windowed to match the LPF passband.

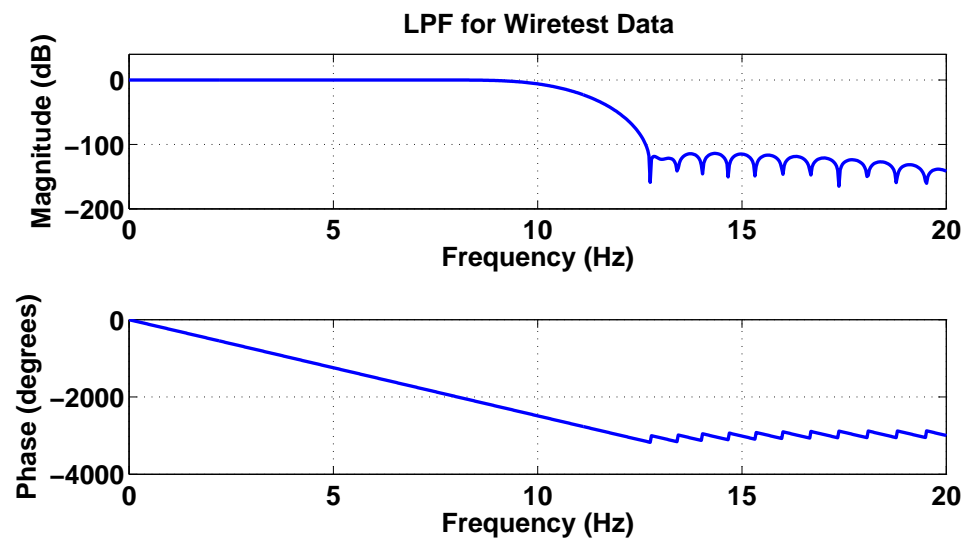


Figure 6.4: Magnitude (top) and phase angle (bottom) of LPF used in acoustic data processing. 2700 point Chebychev window with 10 Hz cutoff frequency. Zoomed to show passband.

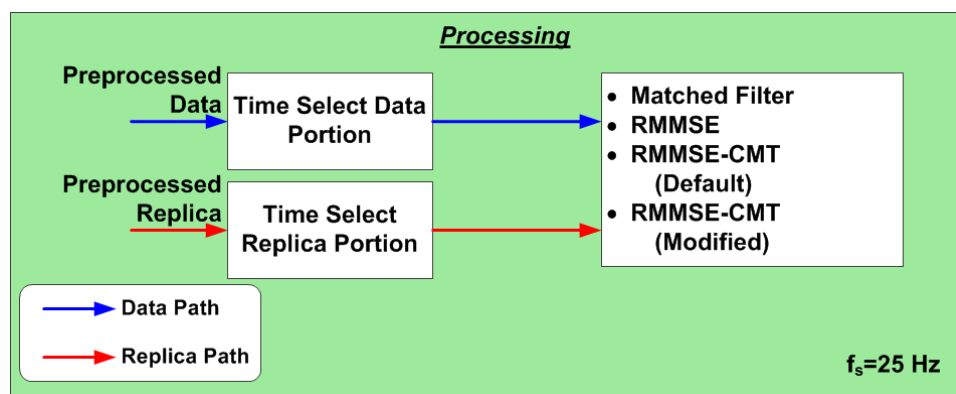


Figure 6.5: Acoustic data and replica processing steps.

Data Time Selection

There are three LFM transmissions present in the data. The first signal was not considered as it appeared to have multiple samples “clipped” at the A/D converter. The second signal appeared to have multiple discrete spurs present immediately prior to the start of the pulse. The third signal has a visually “clean” time response and was selected for processing.

Replica Time Selection

Recall that the replica was generated with the original pulse duration and bandwidth. Following the preprocessing stages, the replica contains many samples that are nearly 0. These samples were omitted from the replica used in processing to reduce the dimension of the covariance matrix. Following this stage, the replica size, $N = 845$.

Algorithms used for Processing

The data was processed using several algorithms to compare performance. Since no distortion is assumed other than intrasample arrival, the basic CMT form is given by (4.19).

- Matched filter: Current state of the art processing capability
- RMMSE: Original RMMSE algorithm
- RMMSE-CMT (Default): RMMSE-CMT approach, with the CMT defined as in (4.19)
- RMMSE-CMT (Modified): RMMSE-CMT approach, with a modified CMT

In the RMMSE-CMT (Default) setting, the results of applying (4.19) result in a CMT whose m^{th} , n^{th} elements are given by:

$$\begin{aligned} C_{\Delta mn} &= \text{sinc}\left(\frac{2\gamma\pi\beta(m-n)}{2Tf_s}\right) \\ &\approx \text{sinc}(0.0037(m-n)) \end{aligned} \tag{6.1}$$

It was found that this CMT did not adequately suppress the sidelobes for this data case. Through experimentation, it was found that the following modified CMT appears to yield better performance for this case:

$$C_{\Delta mn} = \text{sinc}(0.0350(m - n)) \quad (6.2)$$

It is not apparent that this CMT setting corresponds to a given distortion or processing effect. Given the extreme amount of pre-processing necessary to use the data, it may not necessarily be surprising that a significantly different CMT is required to achieve desirable results. The cause of this is still under investigation and is an area of future work.

6.2 Processing Results

The processing results are shown in Figure 6.6. The original RMMSE output is shown in Figure 6.6(a). The standard RMMSE output is not significantly different from the matched filter output. In this case, there is no apparent benefit to using the RMMSE algorithm as the sidelobes are not reduced. In Figure 6.6(b), the RMMSE-CMT results are shown where the CMT is defined as in (6.1). Though there is some suppression of sidelobes, the RMMSE-CMT output does not provide significant benefit over the matched filter results. Furthermore, the variance seen inside the mainlobe is undesirable. Figure 6.6(c) shows the results using the modified CMT as defined in (6.2). In this case, the sidelobes are clearly reduced and the behavior inside the mainlobe is well-behaved. There appear to be approximately 4 clear signals present in the RMMSE-CMT output.

A possible set of signal paths is shown in Figure 6.7. The ray paths are numbered from 1-4, and the paths are briefly summarized as:

- Path 1: Direct path from transmitter sidelobe #1 to receiver
- Path 2: Surface reflection from transmitter sidelobe #2 to receiver

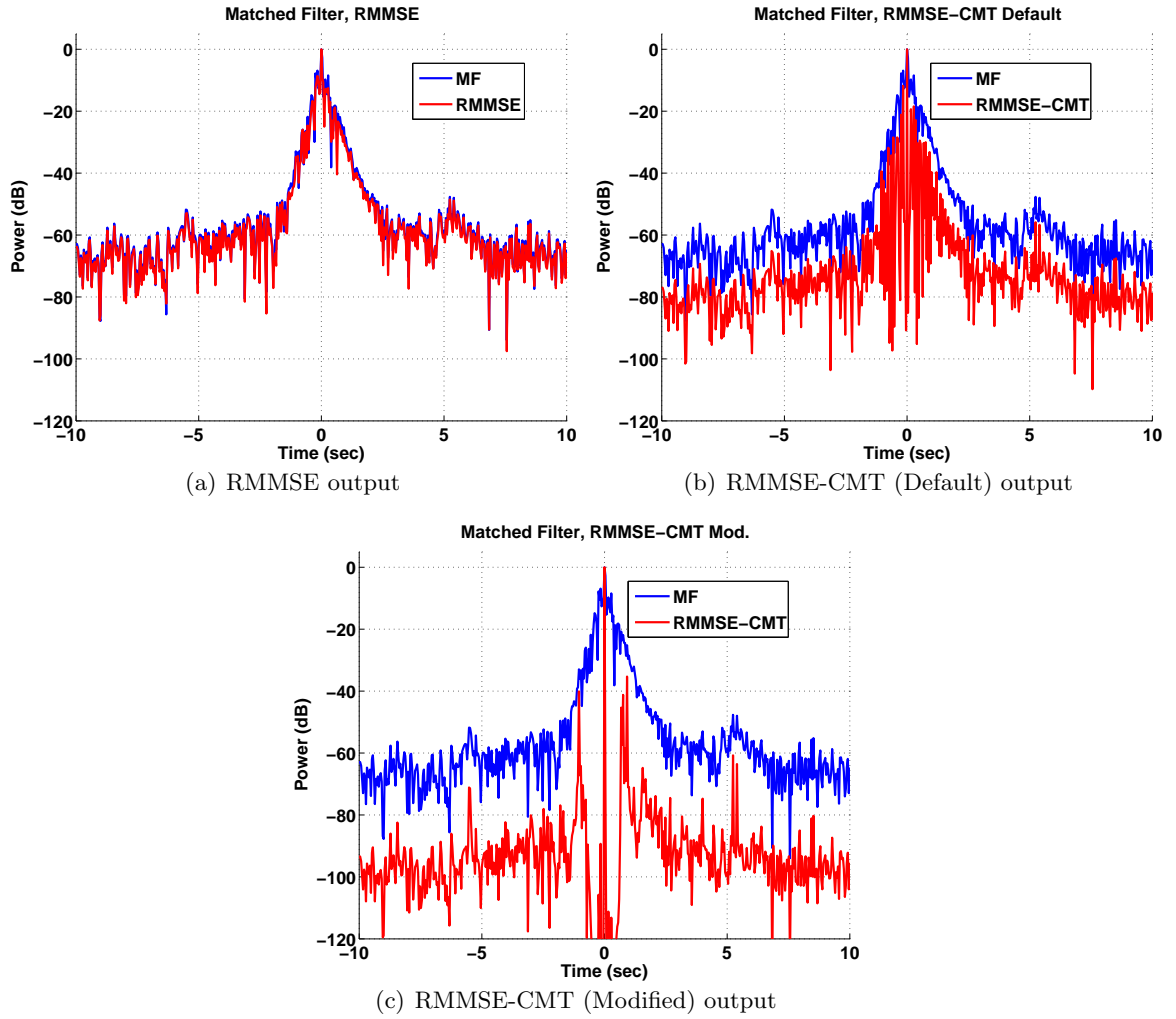


Figure 6.6: Results of processing acoustic data through candidate algorithms. Matched filter shown in blue, adaptive algorithms shown in red

- Path 3: Surface reflection from transmitter mainlobe to receiver
- Path 4: Bottom reflection from transmitter sidelobe #1 to receiver

Transmitter sidelobe #1 is assumed to be pointing along the vertical direction, and transmitter sidelobe #2 is assumed to be pointing at a diagonal angle. Several important parameters for the signals are listed in Table 6.2. In this table, SL refers to “SideLobe” and ML refers to “MainLobe”. In order to compute the total distance traveled, the relative lag at each peak is multiplied by the speed of sound (1500 m/s). The estimated transmit power is obtained by adjusting the RMMSE-CMT output levels shown in Figure 6.6(c). This is accomplished by accounting for transmission loss and reflection loss. Assuming that the power spreading is roughly spherical, the transmission loss L in dB is given by [4]:

$$L_{dB} = 20 \cdot \log_{10}(r) \quad (6.3)$$

where r is the total distance traveled.

Path 1 has no reflection loss as it is a direct-path. Paths 2 and 4 are assumed to have negligible reflection loss due to the angle of incidence. The reflection loss on Path 3 is obtained by first computing a grazing angle of 32 degrees, based on the time delays and configuration. The surface wind speed is assumed to be 10 knots. Using Figure 8.21 from [4], the reflection loss on Path 3 is therefore approximately 45 dB.

The power levels in Table 6.2 are normalized relative to the mainlobe transmit power. Note that Path 1 and Path 4 are both assumed to originate from sidelobe #1 (vertical), and their adjusted power levels are similar. This provides a measure of confidence to the calculations and assumptions made.

6.3 Summary

The acoustic data analysis performed in this chapter provides insight into the practical considerations of the RMMSE algorithm. The waveform present in the available data is

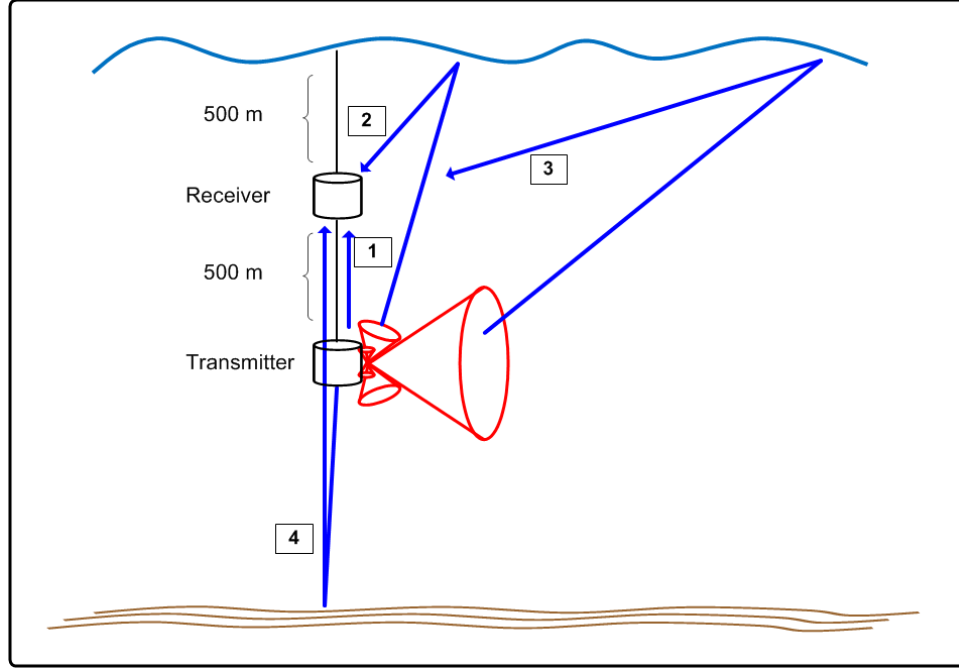


Figure 6.7: Paths resolved by RMMSE output

Table 6.2: Paths for acoustic signal propagation

ID	Tag	Total Dist. (m)	Est Tx Power (dB)
1	Direct	500	-66
2	Surface SL	1950	-16
3	Surface ML	3500	0
4	Bottom	10200	-63

too long to be processed in a reasonable amount of time. Therefore, a portion of the LFM was extracted from the data and used for processing. The signal level is sufficiently high such that the matched filter output is corrupted by time domain sidelobes. The original RMMSE algorithm output does not show significant improvement over the matched filter. Use of the RMMSE-CMT approach derived in Chapter 4 yields slightly different, yet still undesirable performance. Through experimentation, it has been found that the sidelobes are adequately suppressed by modifying the sinc argument of the CMT. There appear to be four signals resolved by the RMMSE-CMT approach. Possible explanations for the signal time delays and power levels are provided.

Chapter 7: Conclusions

This chapter discusses the results of applying the RMMSE algorithm to active sonar data. A brief summary of the application of the algorithm to active sonar data is given, and future work is discussed.

7.1 Application of RMMSE Algorithm to Active Sonar

It has been shown that the RMMSE algorithm can resolve signal arrivals that would otherwise be obscured in matched filter sidelobes. This permits more information to be extracted from the data stream. Potential applications of the RMMSE algorithm in active sonar processing are:

- Multipath arrival separation
- High resolution underwater acoustic imaging
- Bathymetric profiling
- Underwater communications

and possibly others. Since the RMMSE algorithm requires the inversion of an $N \times N$ matrix, RMMSE application is limited by waveform duration and computational capability.

The RMMSE algorithm is sensitive to several types of distortion commonly found in active sonar. The three distortions investigated in this thesis are intrasample arrival, Doppler distortion, and uncalibrated transducers. These distortions are representative of three major classes of distortion- time offsets, phase distortion and frequency shading. In general, mismatch and distortion lead to elevated sidelobe levels and degraded detection capability. RMMSE performance tends to degrade gracefully towards matched filter performance

as the effects of distortion become more severe. The computational cost of the RMMSE algorithm could potentially preclude its use as the detection capability is reduced to the matched filter level.

Covariance Matrix Tapers are an effective approach for making the RMMSE algorithm robust against distortion. They are also computationally efficient as the CMT is computed only once and is applied through use of the Hadamard product. Two CMTs have been derived in this thesis and have been shown to successfully mitigate distortion and return RMMSE performance to the baseline level. The use of CMTs is a new contribution to RMMSE processing.

Given the performance enhancement realized by CMTs, it is recommended that they be used for RMMSE processing in practical active sonar systems. At a minimum, it is recommended to use the intrasample arrival CMT as this form of mismatch is virtually guaranteed. Other CMTs can potentially be developed to address specific forms of distortion.

7.2 Performance with Experimental Data

Due to the lack of publicly available unclassified active sonar data, a low-bandwidth, long duration waveform was used to assess RMMSE performance on real data. Given the duration of the pulse, it was not possible to process the entire waveform in a reasonable amount of time. A portion of the waveform was filtered out and used for processing.

Despite the relatively low bandwidth and sample rate that resulted from preprocessing, the RMMSE-CMT approach suppressed sidelobes and revealed the presence of signal arrivals. These signals are not visible with the baseline RMMSE algorithm or the matched filter.

In order to achieve this level of performance, the CMT was adjusted to a more aggressive setting than the derivations prescribe. The underlying process requiring this setting is currently unclear. Given the extent to which the original data had to be preprocessed, filtered, and downsampled, it is not necessarily surprising that the CMT setting required

adjustment.

7.3 Future Work

The data processed in Chapter 6 provides useful insight to the RMMSE and RMMSE-CMT approaches. More data analysis is necessary to characterize the benefits and potential shortcomings the RMMSE-CMT approach. As data becomes available, further analysis of the RMMSE-CMT approach can be performed.

The Fast Adaptive Pulse Compression (FAPC) algorithm [19] is a reduced rank version of the RMMSE algorithm. It is possible that this algorithm may be used to process the full waveform presented in Chapter 6 without the need for such extensive data pre-processing. Further work is needed to assess the feasibility of using FAPC on sonar data.

Another area of future work is the derivation of CMTs for other common waveforms. The RMMSE algorithm is not waveform dependent and preliminary experiments have verified performance on several different waveforms. In this thesis, CMTs were developed specifically for the LFM waveform because it is one of the most common waveforms used in sonar. The hyperbolic frequency modulated (HFM) waveform is also often used in underwater acoustics. This waveform is more complicated than the LFM, but is extremely insensitive to the Doppler effect when a matched filter is used as the detector [38]. A derivation of CMTs for RMMSE-HFM processing would enable additional datasets to be processed by the RMMSE-CMT algorithm.

It is also desired to assess the use of CMTs in RMMSE processing for radar systems. The frequency shift used to model LFM intrasample arrival is similar to the Doppler model commonly used in radar systems. It is noted in [21] that the modeled radar Doppler distortion leads to elevated RMMSE sidelobes and decreased detection capability. In the cited reference, this Doppler distortion is mitigated through iterative estimation of the Doppler factor. It is possible that the RMMSE-CMT approach can be used as a computationally efficient means of mitigating Doppler distortion in radar systems.

Appendix A: CMT Use in Adaptive Beamforming

Many of the published papers utilizing CMTs are specific to adaptive beamforming applications, particularly the problem of moving interference sources. Most baseline adaptive beamforming algorithms assume that interference signals arrive from discrete angles and are stationary over the time period of interest. If these assumptions are not met, as would be the case in a distributed or moving interferer, the adaptive weights may not adequately suppress the interference. CMTs have been shown to be an effective means for making adaptive beamformers robust against this form of mismatch [34].

A.1 CMT Derivation

In this section, the $N \times N$ beamforming covariance matrix is denoted as \mathbf{S} to distinguish it from the RMMSE covariance matrix, \mathbf{C} . Further, the \mathbf{S} notation is consistent with the notation of Van Trees [12] to emphasize that it is a spectral matrix. The $N \times 1$ array manifold vector, denoted as \mathbf{v} is analogous to the replica waveform vector, \mathbf{s} . As before, the scalar N refers to the dimension of the covariance matrix.

The optimum beamformer weight vector, \mathbf{w}_{ABF} , is often obtained using the following general equation:

$$\mathbf{w}_{ABF} = \kappa \mathbf{S}^{-1} \mathbf{v} \quad (\text{A.1})$$

The κ term is a real-valued scale factor, such the scale factor used in Minimum Variance Distortionless Response (MVDR) beamforming [12]. For purposes of this example, we assume the array has N equally spaced elements. The elements of the array manifold vector \mathbf{v} at the cosine-spaced angle u are given by:

$$\mathbf{v} = \begin{bmatrix} e^{j(0-\frac{N-1}{2})u\pi} \\ e^{j(1-\frac{N-1}{2})u\pi} \\ \vdots \\ e^{j((N-1)-\frac{N-1}{2})u\pi} \end{bmatrix} \quad (\text{A.2})$$

It is assumed in equation (A.2) that the array elements are spaced at half-wavelength intervals.

Two example cases are now presented to illustrate the utility of CMTs. In the first case, the interfering signal is stationary and is described fully by the estimated covariance matrix. In the second case, the interferer has a random motion component which is not completely described by the estimated covariance matrix. It is shown that the random motion can be incorporated into the covariance matrix estimate through the use of a CMT.

A.1.1 Case 1: Stationary Interferer

If an interfering signal of unit power arrives from the angle u_1 , its array manifold vector is given by:

$$\mathbf{v}_1 = \begin{bmatrix} e^{j(0-\frac{N-1}{2})u_1\pi} \\ e^{j(1-\frac{N-1}{2})u_1\pi} \\ \vdots \\ e^{j((N-1)-\frac{N-1}{2})u_1\pi} \end{bmatrix} \quad (\text{A.3})$$

The covariance matrix contribution for this single interferer is given by:

$$\mathbf{S}_1 = E \{ \mathbf{v}_1 \mathbf{v}_1^H \} \quad (\text{A.4})$$

If the interferer is stationary, then $\mathbf{S}_1 = \mathbf{v}_1 \mathbf{v}_1^H$. Often there is a white noise component added to the diagonal elements of \mathbf{S} prior to use in equation (A.1). That step is not shown

here in order to emphasize the interferer component. When \mathbf{S}_1 from equation (A.4) is used to compute the adaptive weights, the resulting beampattern will have a deep, sharp null at angle u_1 . The \mathbf{S} matrix has full knowledge of the interferer location and is able to mitigate its effects.

A.1.2 Case 2: Moving Interferer

Suppose that an estimate of \mathbf{S}_1 has been computed and will be used to generate the weights for subsequent snapshots of data. In a subsequent snapshot, the interferer has moved from its original position of u_1 . The new angle of the interferer is given by $u_2 = u_1 + \Delta_u$. The array manifold vector corresponding to the new interferer location is:

$$\begin{aligned}
\mathbf{v}_2 &= \begin{bmatrix} e^{j(0-\frac{N-1}{2})(u_1+\Delta_u)} \\ e^{j(1-\frac{N-1}{2})(u_1+\Delta_u)} \\ \vdots \\ e^{j((N-1)-\frac{N-1}{2})(u_1+\Delta_u)} \end{bmatrix} \\
&= \begin{bmatrix} e^{j(0-\frac{N-1}{2})u_1} e^{j(0-\frac{N-1}{2})\Delta_u} \\ e^{j(1-\frac{N-1}{2})u_1} e^{j(1-\frac{N-1}{2})\Delta_u} \\ \vdots \\ e^{j((N-1)-\frac{N-1}{2})u_1} e^{j((N-1)-\frac{N-1}{2})\Delta_u} \end{bmatrix} \\
&= \begin{bmatrix} e^{j(0-\frac{N-1}{2})u_1} \\ e^{j(1-\frac{N-1}{2})u_1} \\ \vdots \\ e^{j((N-1)-\frac{N-1}{2})u_1} \end{bmatrix} \circ \begin{bmatrix} e^{j(0-\frac{N-1}{2})\Delta_u} \\ e^{j(1-\frac{N-1}{2})\Delta_u} \\ \vdots \\ e^{j((N-1)-\frac{N-1}{2})\Delta_u} \end{bmatrix}
\end{aligned} \tag{A.5}$$

The relationship between the original position and the offset position is represented in matrix-vector form as:

$$\mathbf{v}_2 = \mathbf{v}_1 \circ \mathbf{v}_\Delta \tag{A.6}$$

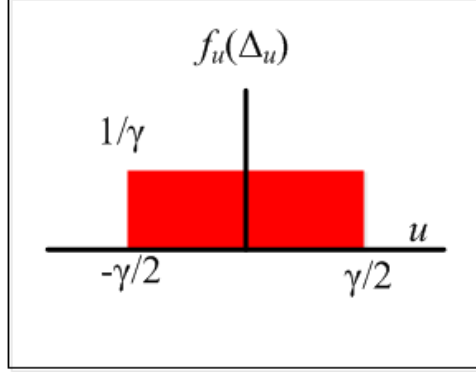


Figure A.1: Probability Density Function for a zero mean uniform angular distribution

Where \mathbf{v}_2 is the true array manifold vector of the interferer. The steering vector of angle u_2 represented as the Hadamard product of the original steering vector and the offset steering vector. The results of equation (4.5) indicate that if the interferer can be decomposed into two vectors related by the Hadamard product as in equation (A.6), then the random effects of interferer motion may be incorporated into a new interference covariance matrix, \mathbf{S}_2 through the Hadamard product of the individual covariance matrices:

$$\mathbf{S}_2 = \mathbf{S}_1 \circ \mathbf{S}_\Delta \quad (\text{A.7})$$

The covariance matrix \mathbf{S}_1 is assumed to have been estimated previously. The motion offset, Δ_u , is an unknown, random quantity. To make use of equation (A.7), the problem is then to estimate \mathbf{S}_Δ . The first step is to assign a random process to describe the interferer motion. For this example, it is assumed that Δ_u is a zero-mean, uniformly distributed random variable on the interval $[-\gamma/2 \ \gamma/2]$. Figure A.1 illustrates the probability density function, $f_u(\Delta_u)$ for this case.

The element in the m^{th} row and n^{th} column of \mathbf{S}_Δ is given by

$$S_{\Delta mn} = E \{ v_{\Delta m} v_{\Delta n}^* \} \quad (\text{A.8})$$

Where $v_{\Delta x}$ corresponds to the x^{th} element of vector \mathbf{v}_{Δ} . The above equation is now expanded and simplified:

$$\begin{aligned}
S_{\Delta mn} &= E \left\{ e^{j\pi\Delta_u \left(n - \frac{N-1}{2}\right)} e^{-j\pi\Delta_u \left(m - \frac{N-1}{2}\right)} \right\} \\
&= E \left\{ e^{j\pi\Delta_u \left(m - \frac{N-1}{2}\right) - j\pi\Delta_u \left(n - \frac{N-1}{2}\right)} \right\} \\
&= E \left\{ e^{j\pi\Delta_u (m-n)} \right\}
\end{aligned} \tag{A.9}$$

The expectation is evaluated by integrating the probability density function and the expectation argument:

$$\begin{aligned}
S_{\Delta mn} &= \int_{-\gamma/2}^{\gamma/2} f_u(\Delta_u) e^{j\pi\Delta_u (m-n)} d\Delta_u \\
&= \int_{-\gamma/2}^{\gamma/2} \frac{1}{\gamma} e^{j\pi\Delta_u (m-n)} d\Delta_u
\end{aligned} \tag{A.10}$$

Using Euler's relation, this becomes

$$S_{\Delta mn} = \int_{-\gamma/2}^{\gamma/2} \frac{1}{\gamma} (\cos(\pi\Delta_u (m-n)) + j \sin(\pi\Delta_u (m-n))) d\Delta_u \tag{A.11}$$

The sine term goes to 0 due to the symmetric limits of integration, leaving

$$S_{\Delta mn} = \int_{-\gamma/2}^{\gamma/2} \frac{1}{\gamma} \cos(\pi\Delta_u (m-n)) d\Delta_u \tag{A.12}$$

This integral is solved directly, and after some algebraic manipulation, the result is

simplified to

$$S_{\Delta mn} = \text{sinc}\left(\frac{\gamma}{2}\pi(m-n)\right) \quad (\text{A.13})$$

Equation (A.13) allows \mathbf{S}_{Δ} to be computed and applied as seen in equation (A.7). This results in a new covariance matrix, \mathbf{S}_2 that incorporates the random motion of the interferer.

A.2 Summary of CMT use in Adaptive Beamforming

The presented example derives the CMT commonly used in adaptive beamforming applications for moving interferers. The actual motion of the interferer does not need to be known, but a statistical description of the motion needs to be assigned.

Bibliography

Bibliography

- [1] S. Blunt and K. Gerlach, “A novel pulse compression scheme based on minimum mean-square error reiteration,” in *Radar Conference, 2003. Proceedings of the International*, September 2003, pp. 349 – 353.
- [2] J. Ehrenberg, T. Ewart, and R. Morris, “Signal-processing techniques for resolving individual pulses in a multipath signal,” *Journal of the Acoustical Society of America*, vol. 63(6), pp. 1861–1865, June 1978.
- [3] C. Therrien, *Discrete Random Signals and Statistical Signal Processing*. Englewood Cliffs, NJ: Prentice-Hall, Inc, 1992.
- [4] R. Urick, *Principles of Underwater Sound, 3rd Edition*. Los Altos Hills, CA: Peninsula Publishing, 1983.
- [5] —, “Sonar design in the real ocean: Multipath limitations on sonar performance,” in *Acoustics, Speech, and Signal Processing, IEEE International Conference on ICASSP '76.*, vol. 1, April 1976, pp. 652 –655.
- [6] D. Abraham, K. Hillsley, and J. Norrmann, “A robust model-based detector for active sonar,” in *OCEANS, 2001. MTS/IEEE Conference and Exhibition*, vol. 4, 2001, pp. 2139 –2146 vol.4.
- [7] G. Golomb, Solomon; Gong, *Signal Design for Good Correlation*. New York, NY: Cambridge University Press, 2005.
- [8] S. Widrow, Bernard; Stearns, *Adaptive Signal Processing*. Englewood Cliffs, NJ: Prentice-Hall, Inc, 1985.
- [9] S. Haykin, *Adaptive Filter Theory*. Englewood Cliffs, NJ: Prentice-Hall, Inc, 1986.
- [10] D. Manolakis, V. Ingle, and S. Kogon, *Statistical and Adaptive Signal Processing*. Norwood, MA: Artech House, Inc, 2005.
- [11] T. Higgins, S. Blunt, and K. Gerlach, “Gain-constrained adaptive pulse compression via an mvdr framework,” in *Radar Conference, 2009 IEEE*, May 2009, pp. 1 –6.
- [12] H. Van Trees, *Optimum Array Processing*. New York, NY: John Wiley & Sons, Inc., 2002.
- [13] S. Blunt and K. Gerlach, “Adaptive pulse compression,” in *Radar Conference, 2004. Proceedings of the IEEE*, April 2004, pp. 271 – 276.

- [14] —, “Adaptive pulse compression via mmse estimation,” *Aerospace and Electronic Systems, IEEE Transactions on*, vol. 42, no. 2, pp. 572 – 584, April 2006.
- [15] —, “Adaptive pulse compression repair processing,” in *Radar Conference, 2005 IEEE International*, May 2005, pp. 519 – 523.
- [16] K. Gerlach and S. Blunt, “Radar pulse compression repair,” *Aerospace and Electronic Systems, IEEE Transactions on*, vol. 43, no. 3, pp. 1188 –1195, July 2007.
- [17] A. Shackelford, J. de Graaf, S. Talapatra, S. Blunt, and K. Gerlach, “Adaptive pulse compression: Preliminary experimental measurements,” in *Radar Conference, 2007 IEEE*, April 2007, pp. 234 –237.
- [18] S. Blunt and T. Higgins, “Achieving real-time efficiency for adaptive radar pulse compression,” in *Radar Conference, 2007 IEEE*, April 2007, pp. 116 –121.
- [19] —, “Dimensionality reduction techniques for efficient adaptive pulse compression,” *Aerospace and Electronic Systems, IEEE Transactions on*, vol. 46, no. 1, pp. 349 –362, January 2010.
- [20] S. Blunt, K. Smith, and K. Gerlach, “Doppler-compensated adaptive pulse compression,” in *Radar, 2006 IEEE Conference on*, April 2006, p. 6 pp.
- [21] S. Blunt, A. Shackelford, K. Gerlach, and K. Smith, “Doppler compensation and single pulse imaging using adaptive pulse compression,” *Aerospace and Electronic Systems, IEEE Transactions on*, vol. 45, no. 2, pp. 647 –659, April 2009.
- [22] S. Blunt and K. Gerlach, “Aspects of multistatic adaptive pulse compression,” in *Radar Conference, 2005 IEEE International*, May 2005, pp. 104 – 108.
- [23] —, “A generalized formulation for adaptive pulse compression of multistatic radar,” in *Sensor Array and Multichannel Processing, 2006. Fourth IEEE Workshop on*, July 2006, pp. 349 –353.
- [24] —, “Multistatic adaptive pulse compression,” *Aerospace and Electronic Systems, IEEE Transactions on*, vol. 42, no. 3, pp. 891 –903, July 2006.
- [25] K. Gerlach, A. Shackelford, and S. Blunt, “A novel approach to shared-spectrum multistatic radar,” in *Radar, 2006 IEEE Conference on*, April 2006, p. 7 pp.
- [26] —, “Combined multistatic adaptive pulse compression and adaptive beamforming for shared-spectrum radar,” *Selected Topics in Signal Processing, IEEE Journal of*, vol. 1, no. 1, pp. 137 –146, June 2007.
- [27] S. Blunt, W. Dower, and K. Gerlach, “Hybrid adaptive receive processing for multistatic radar,” in *Computational Advances in Multi-Sensor Adaptive Processing, 2007. CAMPSAP 2007. 2nd IEEE International Workshop on*, December 2007, pp. 5 –8.
- [28] —, “Hybrid interference suppression for multistatic radar,” *Radar, Sonar Navigation, IET*, vol. 2, no. 5, pp. 232 –333, October 2008.

- [29] S. Blunt, K. Gerlach, and T. Higgins, "Aspects of radar range super-resolution," in *Radar Conference, 2007 IEEE*, April 2007, pp. 683 –687.
- [30] S. Blunt, T. Chan, and K. Gerlach, "A new framework for direction-of-arrival estimation," in *Sensor Array and Multichannel Signal Processing Workshop, 2008. SAM 2008. 5th IEEE*, July 2008, pp. 81 –85.
- [31] —, "Robust doa estimation: The reiterative superresolution (risr) algorithm," *Aerospace and Electronic Systems, IEEE Transactions on*, vol. 47, no. 1, pp. 332 – 346, January 2011.
- [32] B. Zhao, L. Kong, M. Yang, and G. Cui, "Adaptive pulse compression for stepped frequency continuous-wave radar," in *Radar (Radar), 2011 IEEE CIE International Conference on*, vol. 2, October 2011, pp. 1780 –1783.
- [33] S. Wang, Z. Li, and Y. Zhang, "Application of optimized filters to two-dimensional sidelobe mitigation in meteorological radar sensing," *Geoscience and Remote Sensing Letters, IEEE*, vol. 9, no. 4, pp. 778 –782, July 2012.
- [34] R. Mailloux, "Covariance matrix augmentation to produce adaptive array pattern troughs," in *Antennas and Propagation Society International Symposium, 1995. AP-S. Digest*, vol. 1, June 1995, pp. 102 –105 vol.1.
- [35] M. Zatman, "Production of adaptive array troughs by dispersion synthesis," *Electronics Letters*, vol. 31, no. 25, pp. 2141 –2142, December 1995.
- [36] J. Guerci, "Theory and application of covariance matrix tapers for robust adaptive beamforming," *Signal Processing, IEEE Transactions on*, vol. 47, no. 4, pp. 977 –985, April 1999.
- [37] H. Cox, R. Zeskind, and M. Owen, "Robust adaptive beamforming," *Acoustics, Speech and Signal Processing, IEEE Transactions on*, vol. 35, no. 10, pp. 1365 – 1376, October 1987.
- [38] J. Kroszczynski, "Pulse compression by means of linear-period modulation," *Proceedings of the IEEE*, vol. 57, no. 7, pp. 1260 – 1266, July 1969.

Curriculum Vitae

Travis Cuprak graduated from the University of Notre Dame in May 2003 with a Bachelor of Science degree in Electrical Engineering. From 2003 until 2008 he worked at Raytheon Space and Airborne Systems in El Segundo, CA as a Systems Engineer. From 2008 until the present, Travis has worked at Adaptive Methods, Inc., in Centreville, VA as an Engineer. His primary interests are adaptive signal processing and high resolution imaging techniques.